EUROPEAN ORGANIZATION FOR NUCLEAR RESEARCH (CERN)
FERMILAB-PUB-11-718-CMS

CERN-PH-EP/2011-051
2011/06/27

CMS-JME-10-009

arXiv:1106.5048v1 [physics.ins-det] 24 Jun 2011

Missing transverse energy performance of the CMS detector

The CMS Collaboration*

Abstract

During 2010 the LHC delivered pp collisions with a centre-of-mass energy of 7 TeV. In this paper, the results of comprehensive studies of missing transverse energy as measured by the CMS detector are presented. The results cover the measurements of the scale and resolution for missing transverse energy, and the effects of multiple pp interactions within the same bunch crossings on the scale and resolution. Anomalous measurements of missing transverse energy are studied, and algorithms for their identification are described. The performances of several reconstruction algorithms for calculating missing transverse energy are compared. An algorithm, called missing-transverse-energy significance, which estimates the compatibility of the reconstructed missing transverse energy with zero, is described, and its performance is demonstrated.

Submitted to the Journal of Instrumentation

*See Appendix B for the list of collaboration members

Operated by Fermi Research Alliance, LLC under Contract No. De-AC02-07CH11359 with the United States Department of Energy.

1 Introduction

Neutral weakly interacting particles, such as neutrinos, escape from typical collider detectors without producing any direct response in the detector elements. The presence of such particles must be inferred from the imbalance of total momentum. The vector momentum imbalance in the plane perpendicular to the beam direction is particularly useful in pp and $p\bar{p}$ colliders, and is known as missing transverse momentum, here denoted $\vec{\not{E}}_{\mathrm{T}}$. Its magnitude is called missing transverse energy, and is denoted $\not{E}_{\mathrm{T}}$.

Missing transverse energy is one of the most important observables for discriminating leptonic decays of W bosons and top quarks from background events which do not contain neutrinos, such as multijet and Drell–Yan events. It is also an important variable in searches for new weakly interacting, long-lived particles. Many beyond-the-standard-model scenarios, including supersymmetry, predict events with large $\not{E}_{\mathrm{T}}$. The reconstruction of $\vec{\not{E}}_{\mathrm{T}}$ is very sensitive to particle momentum mismeasurements, particle misidentification, detector malfunctions, particles impinging on poorly instrumented regions of the detector, cosmic-ray particles, and beam-halo particles, which may result in artificial $\not{E}_{\mathrm{T}}$.

In this paper, we present studies of $\vec{\not{E}}_{\mathrm{T}}$ as measured using the Compact Muon Solenoid (CMS) detector at the Large Hadron Collider (LHC), based on a data sample corresponding to an integrated luminosity of $36\,\mathrm{pb}^{-1}$. In Section 2, the CMS detector is briefly described. In Section 3, particle reconstruction algorithms and identification requirements, together with the basic sample selection requirements, are given. In Section 4, the different algorithms for evaluating $\vec{\not{E}}_{\mathrm{T}}$ are presented. In Section 5, methods for identifying anomalous $\vec{\not{E}}_{\mathrm{T}}$ mismeasurements from known detector artifacts are described. In Section 6, the scale and resolution are measured using events containing photons or Z bosons. The degradation of the resolution due to the presence of additional soft pp collisions in the same crossing as the hard scatter ("pile-up") is presented. In Section 7 we present distributions from physics processes containing genuine $\not{E}_{\mathrm{T}}$. In Section 8, an algorithm, called "$\not{E}_{\mathrm{T}}$ significance", which is the likelihood that the observed $\vec{\not{E}}_{\mathrm{T}}$ is due to resolution effects, is described, its performance in jet events is demonstrated, and its efficacy for separating events containing a W boson decaying to either an electron and a neutrino or a muon and a neutrino from multijet backgrounds is shown. Conclusions are given in Section 9. Finally, in the Appendix, the optimization of the parameters used in the correction for the detector response is described.

2 The CMS detector

The central feature of the CMS apparatus is a superconducting solenoid, of 6 m internal diameter, providing a field of 3.8 T. Within the field volume are the silicon pixel and strip tracker, the crystal electromagnetic calorimeter (ECAL), and the brass/scintillator hadron calorimeter (HCAL). Muons are measured in gas-ionization detectors embedded in the steel return yoke. In addition to the barrel and endcap detectors, CMS has extensive forward calorimetry.

CMS uses a right-handed coordinate system, with the origin at the nominal interaction point, the x-axis pointing to the centre of the LHC, the y-axis pointing up (perpendicular to the LHC plane), and the z-axis along the anticlockwise-beam direction. The polar angle, θ, is measured from the positive z-axis and the azimuthal angle, ϕ, is measured in the x-y plane relative to the x-axis. Transverse quantities, such as "transverse momentum" ($\vec{p}_{\mathrm{T}}$), refer to the components in the $x-y$ plane. The magnitude of $\vec{p}_{\mathrm{T}}$ is p_{T}. Transverse energy, E_{T}, is defined as $E\sin\theta$.

The electromagnetic calorimeter (ECAL) consists of nearly 76 000 lead tungstate crystals, which

provide coverage in pseudorapidity $|\eta| < 1.479$ in a barrel region (EB) and $1.479 < |\eta| < 3.0$ in two endcap regions (EE). A preshower detector consisting of two planes of silicon sensors interleaved with a total of $3X_0$ of lead is located in front of the EE. The ECAL has an energy resolution of better than 0.5 % for unconverted photons with $E_T > 100$ GeV.

The HCAL is comprised of four subdetectors, a barrel detector (HB) covering $|\eta| < 1.3$, two endcap detectors (HE) covering $1.3 < |\eta| < 3.0$, two forward detectors (HF) covering $2.8 < |\eta| < 5.0$, and a detector outside of the solenoid (HO) covering $|\eta| < 1.3$. The HCAL, when combined with the ECAL, measures hadrons with a resolution $\Delta E/E \approx 100\%\sqrt{E\,[\mathrm{GeV}]} \oplus 5\,\%$. In the region $|\eta| < 1.74$, the HCAL cells have widths of 0.087 in pseudorapidity and 0.087 rad in azimuth. In the (η, ϕ) plane, and for $|\eta| < 1.48$, the HCAL cells map onto 5×5 ECAL crystal arrays to form calorimeter towers projecting radially outwards from close to the nominal interaction point. At larger values of $|\eta|$, the size of the towers increases and the matching ECAL arrays contain fewer crystals.

The muons are measured in the pseudorapidity window $|\eta| < 2.4$, with detection planes made of three technologies: Drift Tubes, Cathode Strip Chambers, and Resistive Plate Chambers. A global fit of the measurements from the muon system and the central tracker results in a p_T resolution between 1 and 5%, for p_T values up to 1 TeV.

The inner tracker measures charged particles within the $|\eta| < 2.5$ pseudorapidity range. It consists of 1440 silicon pixel and 15 148 silicon strip detector modules and is located in the 3.8 T field of the superconducting solenoid. It provides an impact parameter resolution of $\sim 15\ \mu$m and a p_T resolution of about 1.5% for 100 GeV particles.

The first level (L1) of the CMS trigger system, composed of custom hardware processors, uses information from the calorimeters and muon detectors to select, in less than 1 μs, the most interesting events. The High Level Trigger (HLT) processor farm further decreases the event rate from around 100 kHz to ~ 300 Hz, before data storage.

The calibrations used in this analysis were those available at the beginning of the fall of 2010, which are not the final calibrations for this data sample. Improvements and updates to the calibrations can lead to small improvements in resolution.

A much more detailed description of CMS can be found elsewhere [1].

3 Data sample selection and particle reconstruction

The data sets used for the studies presented in this paper were collected from March through November, 2010, and consist of pp collisions at a centre-of-mass energy $\sqrt{s} = 7$ TeV. An integrated luminosity with all subdetectors certified as fully functional of 36 pb^{-1} was available. The detailed selection criteria for the individual data samples used for each study are given throughout the text. However, all require at least one well-identified primary vertex (PV) whose z position is less than 24 cm away from the nominal centre of the detector and whose transverse distance from the z-axis is less than 2 cm, ensuring that particles coming from collisions are well contained in the CMS detector.

The samples used for the studies in this paper are defined through selection requirements on reconstructed jets, electrons, photons, muons, and b jets. We describe the basic identification requirements used for these particles here.

Jet reconstruction and its performance in CMS are discussed in detail elsewhere [2]. For the analyses described in this paper, jets are reconstructed using an anti-k_T algorithm [3] with a jet

radius parameter R of 0.5. The energy of a jet is corrected, on average, to that which would have been obtained if all particles inside the jet cone at the vertex were measured perfectly (particle-level). CMS uses three different types of jets. Calorimeter jets (Calo Jets) are clusters of calorimeter tower energies. Jet-plus-track jets (JPT Jets) achieve improved response by supplementing the calorimeter information with tracking information. Tracks are associated with Calo Jets if they are within the jet cone at the PV. The measured momentum of these tracks is added to the jet. To avoid double-counting energies, the expected response in the calorimeter is subtracted from the Calo Jet if the particle is still within the cone when it impacts the calorimeter. The response and resolution can be further improved using a global particle-flow reconstruction. Details on the CMS particle-flow algorithm and performance can be found in [4]. The particle-flow technique reconstructs a complete, unique list of particles (PF particles) in each event using an optimized combination of information from all CMS subdetector systems. Reconstructed and identified particles include muons, electrons (with associated bremsstrahlung photons), photons (including conversions in the tracker volume), and charged and neutral hadrons. Particle-flow jets (PF Jets) are constructed from PF particles.

Photon candidates are selected from clusters of energy in the ECAL. They are required to be isolated. The ECAL energy in an annular region in the $\eta - \phi$ plane with inner radius 0.06 and outer radius 0.4, excluding a three-crystal-wide strip along ϕ from the candidate, is required to be less than $4.2 + 0.006\, p_{\mathrm{T}}^{\gamma}$ GeV, where p_{T}^{γ} is the transverse momentum in GeV of the photon candidate. The sum of the p_{T}s of the tracks in the same region must be less than $2.2 + 0.0025\, p_{\mathrm{T}}^{\gamma}$ GeV. The ratio of the HCAL energy in an annular region with inner radius 0.15 and outer radius 0.4 to the ECAL cluster energy is required to be less than 0.05. The shape of the cluster of calorimeter energies must be consistent with that of an electromagnetic shower. In addition, to provide strong rejection against misidentification of electrons as photons, the cluster must not match any track reconstructed in the pixel detector that is consistent with coming from the primary vertex. Photon reconstruction and identification are described in detail in [5].

Electrons are identified using similar criteria. In addition to similar shower shape and isolation requirements, the candidate must match well in both ϕ and η to a charged track, but be isolated from additional tracks. Electron candidates are also required to be in the fiducial portion of the calorimeter ($|\eta| < 1.4442$ or $1.5660 < |\eta| < 2.5$). More details are given in [6]. In addition, photon-conversion rejection is used in some of the analyses presented in this paper.

Muon candidates consist of a track in the tracker which can be linked to one reconstructed in the muon system. The candidate must be isolated from deposits of energy in the ECAL and HCAL that are not consistent with having been deposited by the muon. The sum of the p_{T}s of other tracks within an isolation cone centered on the candidate must also be small.

Several algorithms for the identification of b jets have been developed [7, 8]. Two of them are used in an analysis described in this paper. The `SimpleSecondaryVertex` (SSV) tagging algorithm exploits the significance of the three-dimensional flight distance between the PV and a reconstructed secondary vertex. The `SoftMuonByPt` (SMbyPt) tagger uses the transverse momentum of the muon with respect to the jet axis to construct a discriminant.

The collision data are compared to samples of simulated events that were generated either using PYTHIA 6 [9], with a parameter setting referred to as tune Z2, or with MADGRAPH interfaced with PYTHIA [10]. The generated events are passed through the CMS detector simulation based on GEANT4 [11]. The detector geometry description includes realistic subsystem conditions such as simulation of nonfunctioning channels. The samples used in Section 6.5 include pile-up. The offline event selection for collision data is also applied to simulated events.

4 Reconstruction of $\not{E}_T$

In general, $\vec{\not{E}}_T$ is the negative of the vector sum of the transverse momenta of all final-state particles reconstructed in the detector. CMS has developed three distinct algorithms to reconstruct $\vec{\not{E}}_T$: (a) PF $\not{E}_T$, which is calculated using a complete particle-flow technique [4]; (b) Calo $\not{E}_T$, which is based on calorimeter energies and the calorimeter tower geometry [12]; and (c) TC $\not{E}_T$, which corrects Calo $\not{E}_T$ by including tracks reconstructed in the inner tracker after correcting for the tracks' expected energy depositions in the calorimeter [13].

PF $\not{E}_T$ is calculated from the reconstructed PF particles. PF $\sum E_T$ is the associated scalar sum of the transverse energies of the PF particles.

Calo $\not{E}_T$ is calculated using the energies contained in calorimeter towers and their direction, relative to the centre of the detector, to define pseudo-particles. The sum excludes energy deposits below noise thresholds. Since a muon deposits only a few GeV on average in the calorimeter, independent of its momentum, the muon p_T is included in the Calo $\not{E}_T$ calculation while the small calorimetric energy deposit associated to the muon track is excluded. Calo $\sum E_T$ is the associated scalar sum of the transverse energies of the calorimeter towers and muons.

TC $\not{E}_T$ is based on Calo $\not{E}_T$, but also includes the p_Ts of tracks that have been reconstructed in the inner tracker, while removing the expected calorimetric energy deposit of each track. The predicted energy deposition for charged pions is used for all tracks not identified as electrons or muons. The calorimetric energy deposit is estimated from simulations of single pions, in intervals of p_T and η, and an extrapolation of the track in the CMS magnetic field is used to determine its expected position. No correction is applied for very high p_T tracks ($p_T > 100$ GeV), whose energy is already well measured by the calorimeters. For low-p_T tracks ($p_T < 2$ GeV), the measured momentum is taken into account assuming no response from the calorimeter.

The magnitude of the $\vec{\not{E}}_T$ can be underestimated for a variety of reasons, including the nonlinearity of the response of the calorimeter for neutral and charged hadrons due to its noncompensating nature, neutrinos from semileptonic decays of particles, minimum energy thresholds in the calorimeters, p_T thresholds and inefficiencies in the tracker, and, for Calo $\not{E}_T$, charged particles that are bent by the strong magnetic field of the CMS solenoid and whose calorimetric energies are therefore in a calorimeter cell whose associated angle is very different from the angle of the track at the vertex. The displacement of charged particles with small p_T due to the magnetic field and the calorimeter nonlinearity are the largest of these biases, and thus Calo $\not{E}_T$ is affected most. A two-step correction has been devised in order to remove the bias in the $\vec{\not{E}}_T$ scale. The correction procedure relies on the fact that $\vec{\not{E}}_T$ can be factorized into contributions from jets, isolated high p_T photons, isolated high p_T electrons, muons, and unclustered energies. The contribution due to unclustered energies is the difference between the $\vec{\not{E}}_T$ and the negative of the vector sum of the p_Ts of the other objects. Isolated photons, electrons, and muons are assumed to require no scale corrections.

Jets can be corrected to the particle level using the jet energy correction [2]. The "type-I corrections" for $\vec{\not{E}}_T$ use these jet energy scale corrections for all jets that have less than 0.9 of their energy in the ECAL and corrected $p_T > 20$ GeV for Calo $\not{E}_T$, and for a user-defined selection of jets with $p_T > 10$ GeV for PF $\not{E}_T$. These corrections can be up to a factor of two for Calo $\not{E}_T$ but are less than 1.4 for PF $\not{E}_T$ [14] . In order to correct the remaining soft jets below this threshold, and energy deposits not clustered in any jet, a second correction can be applied to the unclustered energy, which is referred to as the "type-II correction". This correction is obtained from $Z \to ee$ events, as discussed in the Appendix.

In this paper, distributions involving Calo $\not{E}_{\mathrm{T}}$ include both type-I and type-II corrections, those involving PF $\not{E}_{\mathrm{T}}$ include type-I corrections, and those involving TC $\not{E}_{\mathrm{T}}$ are uncorrected, as these were the corrections that were available at the time the analyses presented in this paper were performed and are the versions used most typically in 2010 physics analyses. As discussed in the Appendix, type-II corrections have been developed for PF $\not{E}_{\mathrm{T}}$ and can be used in future analyses. The optimization of both corrections is also discussed in the Appendix.

5 Large $\not{E}_{\mathrm{T}}$ due to misreconstruction

This section describes various instrumental causes of anomalous $\vec{\not{E}}_{\mathrm{T}}$ measurements, and the methods used to identify, and sometimes to correct, $\vec{\not{E}}_{\mathrm{T}}$ for these effects. We also examine the contributions to the tails of the $\not{E}_{\mathrm{T}}$ distribution from non-functioning channels, uninstrumented regions of the detector. and particles from sources other than pp interactions.

5.1 Contributions to $\not{E}_{\mathrm{T}}$ from anomalous signals in the calorimeters

The CMS ECAL and HCAL occasionally record anomalous signals that correspond to particles hitting the transducers. Anomalous signals in HCAL can also be produced by rare random discharges of the readout detectors. Some of these effects had already been observed during past test beam and cosmic data taking [15]. Detailed studies of these effects have continued with the 7 TeV data taking, and are documented in detail in [16] for the HCAL, and in [17] for the ECAL. For some types of anomalous energies, the number of affected channels is small and the event can still be used in physics analysis after the removal of the anomaly. We refer to the removal process as "cleaning" the event. If a large number of channels are effected, "filters" instead tag the event as not suitable for use in physics analysis.

Anomalous energy deposits in EB are associated with particles striking the sensors and very occasionally interacting to produce secondaries that cause large anomalous signals through direct ionization of the silicon. Three main types of noise have been identified in HF: scintillation light produced in the light guides that carry the light from the quartz fibres to the photomultipliers, Cherenkov light in the photomultiplier tube (PMT) windows, and punch-through particles hitting the PMTs. While the EB, HF scintillation and HF Cherenkov sources typically affect only a single channel, signals generated in the HF by particles that exit the back of the calorimeter can affect clusters of channels per event. In the HB and HE, electronics noise from the Hybrid Photo Diode (HPD) and Readout BoX (RBX) occurs, and can affect from one up to all 72 channels in an RBX. This noise is not related to interactions with particles from pp interactions but instead occurs at a low rate and at random times, so the overlap with pp interactions is very low at the bunch spacings of the 2010 run.

The basic strategy for the identification and removal of anomalous signals (cleaning) is based on information such as unphysical charge sharing between neighbouring channels in η-ϕ and/or depth, and timing and pulse shape information. Each of the calorimeters in CMS measures and samples signals every twenty-five ns and several samples are saved with the event record. The shapes of the pulses for signals that develop from energy deposits in the calorimeters are different than those from anomalous noise signals.

Once a "hit" in an HCAL tower or ECAL crystal is determined to be unphysical, we exclude it from the reconstruction of higher-level objects such as jets or $\vec{\not{E}}_{\mathrm{T}}$. We thus arrive at a reconstruction of jets and $\vec{\not{E}}_{\mathrm{T}}$ that is consistently "cleaned" of anomalous detector effects. Studies using simulations of a variety of different physics processes indicate that the amount of energy due to particles produced in a pp scattering that is removed is negligible.

Some features of anomalous signals can be used to identify events contaminated by them most effectively after higher level objects such as jets have been reconstructed. Usually we reject events containing these types of anomalies using filters instead of trying to clean them, although some cleaning is available for PF $\not{E}_T$. For example, we usually exclude events with HPD or RBX noise affecting many channels from our data samples using the requirements described in [15]. We find that this requirement excludes 0.003% of an otherwise good inclusive sample of pp interactions (minimum-bias events).

The Calo $\not{E}_T$ distribution from a data sample that was collected on a trigger that requires a coincidence in the beam pick-up monitors and scintillators in front of the HF calorimeter (minimum bias data) are shown before and after removal of the anomalous signals in Fig. 1, demonstrating the effect of the cleaning and filters. A comparison with simulation, which does not include anomalous energies, shows good agreement. The effect of the cleaning on the other types of $\not{E}_T$ is similar.

The minimum bias triggers used to collect the data shown in Fig. 1 were prescaled for most of the data-taking period. Triggers that require large amounts of energy in the detector, such as $\not{E}_T$ triggers and single jet triggers, are enriched in events with anomalous energies. Filters for cosmic rays, other non-collision-related sources of high $\not{E}_T$, and other types of anomalies have been developed in the context of specific searches for new particle production [18]. An example of a filter for beam-halo muons, which can produce high energy bremsstrahlung photons in the detector, is given in the next section.

Hardware modifications to mitigate one of the largest sources of anomalous energies during the 2010 run, scintillation light produced in part of the light guide reflective sleeves in the HF, were implemented during the winter 2010 shutdown period. During this period, the material that was producing the scintillation light was replaced with Tyvek. These modifications reduce the rate of noise events in HF by an order of magnitude. The HF PMTs will be replaced with multi-anode PMTs with flat, thinner front glass during 2013/2014 winter shutdown, reducing the noise from Cherenkov light and punch-through particles. To reduce the noise observed in HB and HE, HPDs will be replaced by Silicon Photo Multipliers (SiPM) that do not produce this type of noise.

5.2 Removal of beam-induced contributions to $\not{E}_T$

Machine-induced backgrounds, especially the production of muons when beam protons suffer collisions upstream of the detector ("beam halo"), can cause anomalous, large $\not{E}_T$. The CMS beam-halo event filter uses trigger and reconstruction-level information obtained from the Cathode Strip Chambers (CSCs), a subdetector with good reconstruction performance for both collision and non-collision muons [19] and can be used to tag events for removal. The geometry of the CSCs make it difficult for beam-halo particles, with mostly parallel-to-beam trajectories, to traverse the barrel calorimetry without traversing one or both CSC endcaps.

The filter can operate in either a "loose" or "tight" mode. The former is designed for high tagging efficiency at the cost of a modest misidentification probability, while the latter tags only well-identified halo candidates and has a smaller misidentification probability. The tagging efficiencies and misidentification probabilities have been assessed using simulation. For simulated beam-halo particles which impact the calorimeters and produce Calo $\not{E}_T > 15$ GeV, the loose (tight) filter is roughly 92% (65%) efficient. The per-event mistag probability determined from a simulation of inclusive pp interactions (minimum-bias events) for the loose (tight) filter is $\sim 10^{-5}$ (10^{-7}). The tagging inefficiency is due in part to halo muons which do not traverse enough active layers of the CSCs for a well-measured track to be reconstructed and in part to

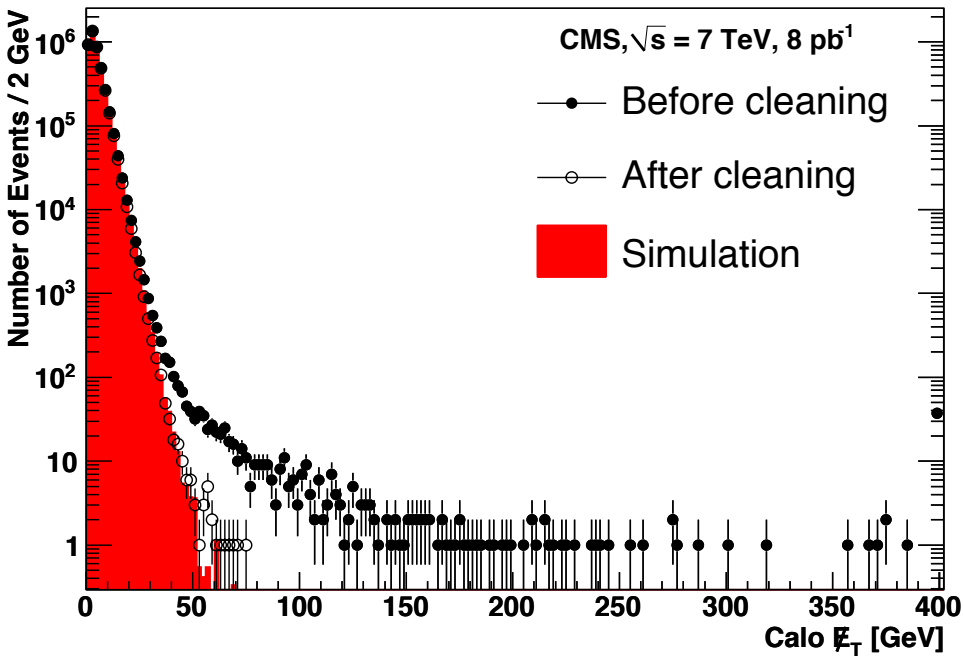

Figure 1: Calo $\not{E}_T$ distributions in a minimum bias data sample without (black dots) and with (open circles) cleaning and filters, compared to simulation. Overflows are included in the highest bin.

muons that do not meet the coincidence requirements of the L1 beam-halo trigger. Many of the mistagged events are from extremely soft and forward muons (i.e. $p_T < 2$ GeV and $|\eta| > 1.7$), from pion decay or from hadron punch through.

The CSC-based beam-halo filter was applied to events passing muon triggers which had p_T thresholds of 9, 11, or 15 GeV, depending on the running period. Beam-halo muons, because their tracks do not point towards the nominal interaction point in the centre of the detector, in general do not fire the triggers for muons from pp interactions. Thus the beam halo muons in this sample are overlaid on events triggered otherwise. This sample therefore provides an unbiased comparison of $\not{E}_T$ in events with and without a beam-halo muon in coincidence. Minimum bias events could have been used as well, but, because the minimum bias trigger was prescaled, the number of available events was small. The fraction of halo-tagged events for each running period is shown versus the average beam intensity, with an uncertainty of approximately 10%, in Fig. 2(left). The fraction of tagged events increases with the beam intensity, as might be expected.

Figure 2(right) shows the PF $\not{E}_T$ distribution for two trigger streams. The distribution from events recorded by collision muon triggers is shown by the dashed curve while that of the subset of these events which met the requirements of the tight halo filter is shown by the red inverted triangles. As can be seen, the halo muons that overlapped with these events did not disproportionately produce events with large PF $\not{E}_T$, which indicates that the probability that a halo muon produces large $\not{E}_T$ in events taken from triggers that are uncorrelated with $\not{E}_T$ is small. However, events from a trigger on Calo $\not{E}_T$ with a minimum trigger threshold of 100 GeV (solid curve), show a substantial fraction identified as halo (blue triangles), since the trigger preferentially selects events in which the beam-halo muon has deposited large amounts

of energy in the calorimeter. A beam-halo filter is therefore necessary for analyses that make use of samples based on this trigger.

5.3 Contributions of non-instrumented or non-functioning detector regions

Particles traversing poorly instrumented regions of the detector can be a cause of apparent $\vec{\not{E}}_T$. While generally hermetic, the CMS calorimeter does have uninstrumented areas (cracks) at the boundary between the barrel and endcap sections, and between the endcap and the forward calorimeters. The gap between the barrel and endcap sections is about 5 cm and contains various services, including cooling, power cables, and silicon detector readout. The crack is not projective to the interaction point. In addition, about 1% of the ECAL crystals are either not operational or have a high level of electronic noise [17], and they are masked in reconstruction. The η-ϕ distribution of these crystals for the barrel, and y-z distribution for the endcaps, is shown in Fig. 3.

In this Section, we illustrate the effect of these features on the $\not{E}_T$ distribution and test the reliability of the simulation for events with jets pointing towards masked ECAL channels or cracks.

Figure 4 shows the $\not{E}_T$ distributions from simulated samples of events containing at least 2 jets, with the leading jet satisfying $p_T > 50$ GeV and the second jet satisfying $p_T > 25$ GeV, for Calo $\not{E}_T$, TC $\not{E}_T$, and PF $\not{E}_T$. For events with $100 < \not{E}_T < 200$ GeV, the contribution from QCD multijet production is 24–42%, depending on the $\vec{\not{E}}_T$ reconstruction algorithm; the rest is from $W/Z/t\bar{t}$ production. In order to illustrate the effect of the cracks, distributions are also shown for those subsets of these samples that have at least one jet that is aligned with the $\vec{\not{E}}_T$ to within $\Delta\phi(\vec{\not{E}}_T, \text{jet}) < 0.2$ and that is pointing towards masked ECAL channels, the barrel-endcap boundary ($1.3 < |\eta| < 1.7$), or the endcap-forward boundary ($2.8 < |\eta| < 3.2$). The masked ECAL channels considered here are those that are part of a group of 5×5 or 5×1 masked channels that are adjacent in η-ϕ, as they have larger impact on the $\not{E}_T$ distributions than isolated masked channels. A jet is considered to be pointing to one of the masked ECAL channels when its jet centroid is within $\Delta R < 0.2$ of a masked ECAL channel, where $\Delta R =$

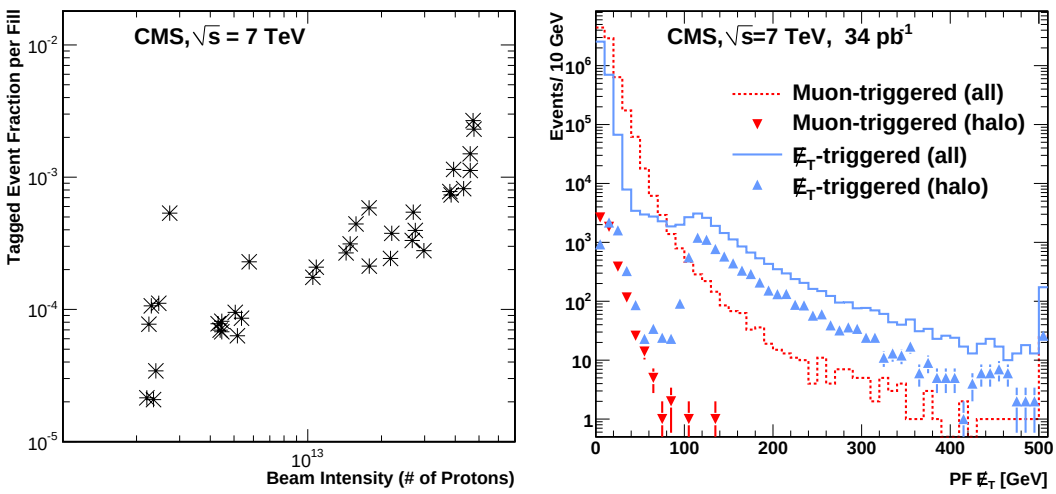

Figure 2: (left) Probability of finding a beam-halo tagged event in muon-triggered events. Results are shown as a function of the beam intensity. (right) PF $\not{E}_T$ distribution for all the events from muon and Calo $\not{E}_T$ triggers that were analyzed, and for the subset of these events that were identified as beam halo.

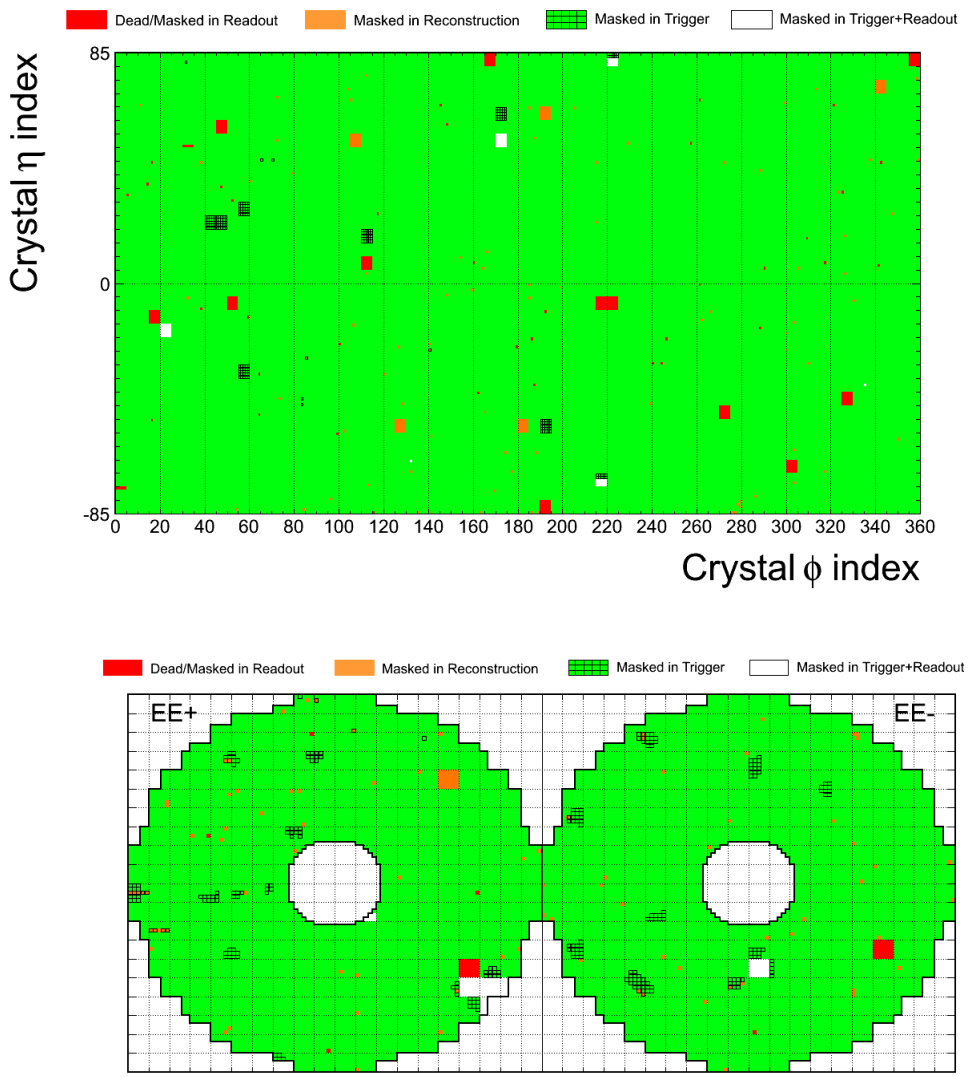

Figure 3: Distribution of masked ECAL channels in (top) barrel: η-ϕ view of 170x360 individual crystals and (bottom) endcaps: y-z view of 2x7400 individual crystals.

$\sqrt{(\Delta\eta)^2 + (\Delta\phi)^2}$. We can see effects on the $\not{E}_T$ distribution from masked ECAL channels, while the calorimeter boundaries do not appear to have an enhanced contribution to the events with large $\not{E}_T$.

Figure 5 shows the fraction of dijet events with at least one jet aligned with the $\vec{\not{E}}_T$ and also pointing towards the masked ECAL channels, the barrel-endcap boundary, or endcap-forward boundary for data and for simulation. Figure 5(left) shows that the masked ECAL channels enhance the rate of events with large $\not{E}_T$ in both data and Monte Carlo simulation. Approximately 20% of the events with $\not{E}_T > 80$ GeV have contributions to the measured $\vec{\not{E}}_T$ from mismeasurements due to masked ECAL channels. Results from simulations indicate that the fraction of events with large $\not{E}_T$ due to mismeasurements (excluding the predicted contributions from sources of genuine $\not{E}_T$, such as $W/Z/t\bar{t}$) is 30%. As shown in Figs. 5(middle) and

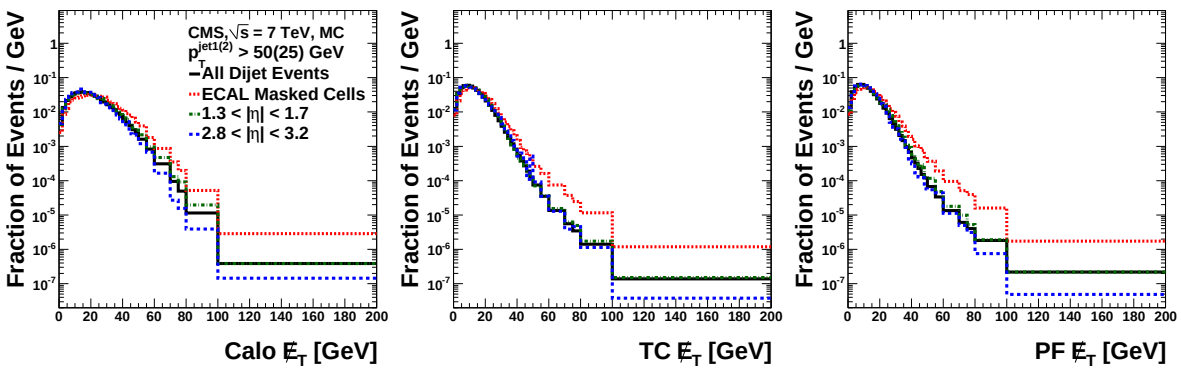

Figure 4: Distribution of (left) Calo $\not{E}_T$, (middle) TC $\not{E}_T$, and (right) PF $\not{E}_T$, normalized to unit area, for events containing at least 2 jets with $p_T^{\mathrm{jet1(2)}} > 50$ (25) GeV (black solid), and for the subsets of these events with a jet aligned with $\vec{\not{E}}_T$ within $\Delta\phi(\vec{\not{E}}_T, \mathrm{jet}) < 0.2$ and pointing towards a masked ECAL cell (red dotted), the barrel-endcap boundary (green dot-dashed), and the endcap-forward boundary (blue dashed) in simulation.

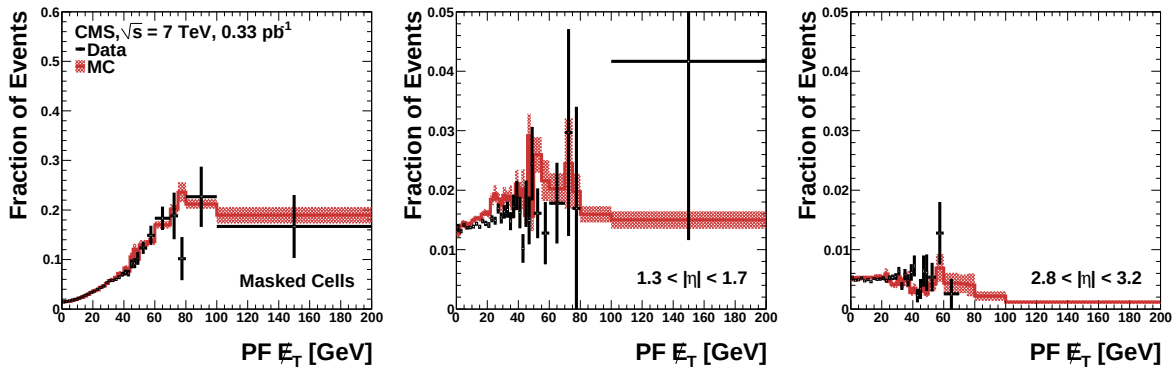

Figure 5: Fraction of dijet events in data (points) and simulation (red band) with a jet aligned to $\vec{\not{E}}_T$ within $\Delta\phi(\vec{\not{E}}_T, \mathrm{jet}) < 0.2$ and pointing towards (left) a masked ECAL channel, (middle) the barrel-endcap boundary, and (right) the endcap-forward boundary, in data and in simulation.

5(right), the fraction of events which contain a jet that is both aligned with the $\vec{\not{E}}_T$ and pointing towards a calorimeter boundary does not have a strong dependence on $\not{E}_T$, indicating that the calorimeter boundaries are not major contributors to events that have large apparent $\not{E}_T$ due to mismeasurements. Unlike the masked ECAL channels, the cracks are not projective to the interaction point, and therefore energies of particles traversing these cracks are still measured, albeit with degraded resolution.

While the impact of the cracks is small, analyses sensitive to events with large $\not{E}_T$ need to take the ECAL masked channels into account. About 70% of the ECAL channels that are masked during offline reconstruction have a useful measurement of their energy from the separate readout of the L1 trigger. Although the trigger readout saturates, it can be used to recover energies smaller than this and to identify events that had more than this amount of energy in a masked channel. This saturation energy has been increased from 64 GeV to 128 GeV in 2011. Analysts can veto events with a jet pointing towards an ECAL masked channel that does not have trigger information or that has trigger-readout energy at the saturation threshold.

6 Missing transverse energy scale and resolution

In this section, we study the performance of $\vec{\not{E}}_{\mathrm{T}}$ using events where an identified Z boson or isolated γ is present. Events containing vector bosons may be produced in hard parton-parton collisions such as qg$\rightarrow$ qγ, q$\bar{\mathrm{q}}$ $\rightarrow$ Z, qg$\rightarrow$qZ, and q$\bar{\mathrm{q}}$ $\rightarrow$ gZ. While there is no genuine $\not{E}_{\mathrm{T}}$ in these events, we can induce it by removing the vector boson. By comparing the momenta of the well-measured and well-understood vector boson to the $\vec{\not{E}}_{\mathrm{T}}$ induced this way, we probe the detector response to the global hadronic system and measure the scale and resolution of $\vec{\not{E}}_{\mathrm{T}}$. While the lowest order underlying processes may be simple, many physics and experimental issues contribute to the measured, induced $\vec{\not{E}}_{\mathrm{T}}$ in these events. Effects due to jet energy scale corrections and fluctuating jet composition directly impact the measurement of the hadronic products of the hard collision. Underlying event activity, pile-up, detector noise, and finite detector acceptance contribute as well.

The following notation is used: the vector boson momentum in the transverse plane is $\vec{q}_{\mathrm{T}}$, and the hadronic recoil, defined as the vector sum of the transverse momenta of all particles except the vector boson (or its decay products, in the case of Z candidates), is $\vec{u}_{\mathrm{T}}$. Momentum conservation in the transverse plane requires $\vec{q}_{\mathrm{T}} + \vec{u}_{\mathrm{T}} = 0$. The recoil is the negative of the induced $\vec{\not{E}}_{\mathrm{T}}$.

The presence of a well-measured Z or γ provides both a momentum scale, $q_{\mathrm{T}} \equiv |\vec{q}_{\mathrm{T}}|$, and a unique event axis, $\hat{q}_{\mathrm{T}}$. The hadronic recoil can be projected onto this axis, yielding two signed components, parallel ($u_{\parallel}$) and perpendicular ($u_{\perp}$) to the event axis. Since $u_{\parallel} \equiv \vec{u}_{\mathrm{T}} \cdot \hat{q}_{\mathrm{T}}$, and the observed hadronic system is usually in the opposite hemisphere from the boson, $u_{\parallel}$ is typically negative.

The mean value of the scalar quantity $\langle u_{\parallel} \rangle / q_{\mathrm{T}}$ is the scale factor correction required for $\not{E}_{\mathrm{T}}$ measurements in the classes of events considered here, and is closely related to jet energy scale corrections and jet parton flavour. We refer to $\langle u_{\parallel} \rangle / q_{\mathrm{T}}$ as the "response" and denote distributions of this quantity versus q_{T} as "response curves". Deviations of the response curve from unity probe the $\not{E}_{\mathrm{T}}$ response as a function of q_{T}.

Resolution is assessed by measuring the RMS spread of $u_{\parallel}$ and $u_{\perp}$ about their mean values, after correcting for the response, and is denoted $RMS(u_{\parallel})$ and $RMS(u_{\perp})$. As with the response, we examine the resolutions as functions of q_{T}.

6.1 Direct photon sample

Candidate photon events are selected by requiring each event to contain exactly one reconstructed photon in the barrel portion of the ECAL ($|\eta| < 1.479$), with $q_{\mathrm{T}} > 20$ GeV, and which passes the identification and isolation selection described in Section 3. The total number of events passing all requirements is 157567, of which 67621 have only one reconstructed primary vertex. The prescale factors for the HLT triggers used to collect this sample varied over the course of the 2010 LHC running period. As a result, this sample is dominated by events recorded during the earlier period of the data taking, when the fraction of crossings containing pile-up interactions was smaller.

Figure 6 shows the photon q_{T} spectrum for data and for simulation. About half of the observed rate arises from QCD dijet production where one jet passes all photon identification requirements. Such jets are typically highly enriched in $\pi^0 \rightarrow \gamma\gamma$ and contain little hadronic activity. The detector response to these jets is similar to that of single photons, and studies indicate that response curves extracted from these QCD background events match the response of true

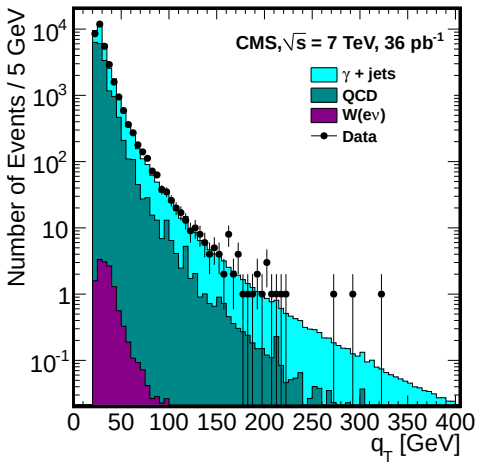

Figure 6: Distribution of q_T for events selected as photon+jet candidates. Predicted rates from simulation for signal and backgrounds are also shown. QCD refers to multijet events.

photon-jet events to within a percent. We therefore make no further attempt to filter them out. The detector response to the jet depends on the type of parton from which it originated. The leading jet in photon events is predicted to predominantly be a quark jet. A prediction for the difference in response for the CMS detector between quark and gluon jets can be found in [20]. The difference is largest for Calo Jets ($\approx$ 20% for jets with p_T of 20 GeV), and decreases with p_T. The primary reason that the response is lower for gluon jets is that their particles tend to have lower p_Ts, and the calorimeter response is lower at low p_T. For PF jets and PF $\not{E}_T$, which use tracker instead of calorimeter momenta for most charged hadrons, the difference in response is reduced, and varies from about 5% at 20 GeV to a percent a high p_T.

6.2 Z samples

For the $Z \to e^+e^-$ selection (electron channel), we require two well-identified and isolated electrons, with $p_T > 20$ GeV, within the fiducial region of the ECAL. The invariant mass ($M_{\ell\ell}$) of the electron pair is required to be in the range $70 < M_{\ell\ell} < 120$ GeV.

For the $Z \to \mu^+\mu^-$ selection (muon channel), we require two isolated muons with opposite electric charges, that have $p_T > 20$ GeV, and are within the $|\eta| < 2.1$ region. The invariant mass $M_{\ell\ell}$ of the muon pair is required to be at least 60 GeV, and no more than 120 GeV.

We obtain a total of 12 635 (12 383) $Z \to e^+e^-$ ($Z \to \mu^+\mu^-$) candidates. The relative contributions of signal and background are estimated from simulation. By normalizing the invariant mass distribution from simulation of signal and background so that it has the same number of events that is observed in the data, a total background of around 143 (35) events is estimated to have a contribution of 97 (2) events from QCD, 28 (9) events from electroweak, and 18 (24) from final states containing top quarks.

Figure 7 shows the $M_{\ell\ell}$ distribution for the electron and muon samples. Figure 8 shows their q_T spectrum. Except at very low q_T, the leading jet in Z events, as with the γ events, should usually be a quark jet.

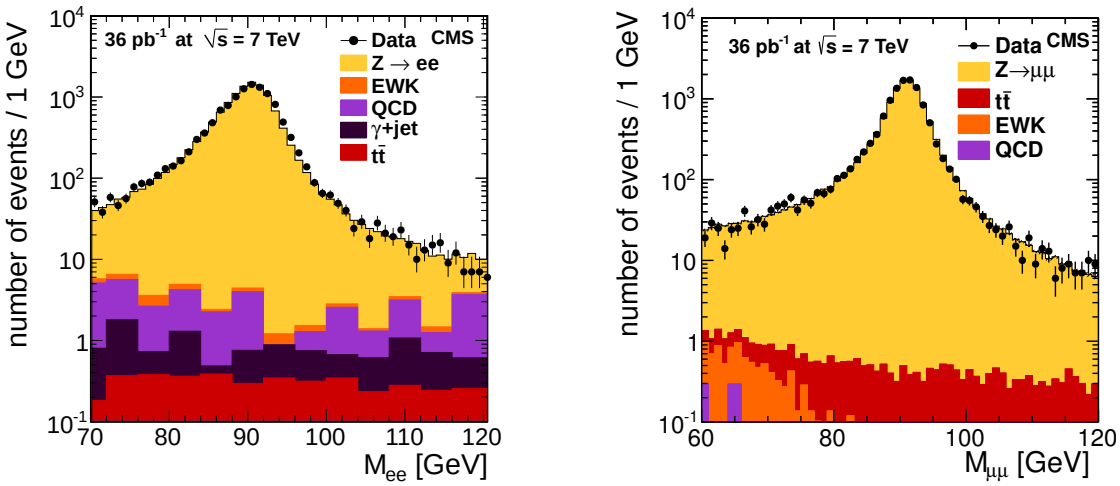

Figure 7: (left) Invariant mass distribution of the two leading electrons and (right) invariant mass distribution of the two leading muons, for the Z boson candidates, along with the predicted distribution from simulation. QCD refers to multijet events.

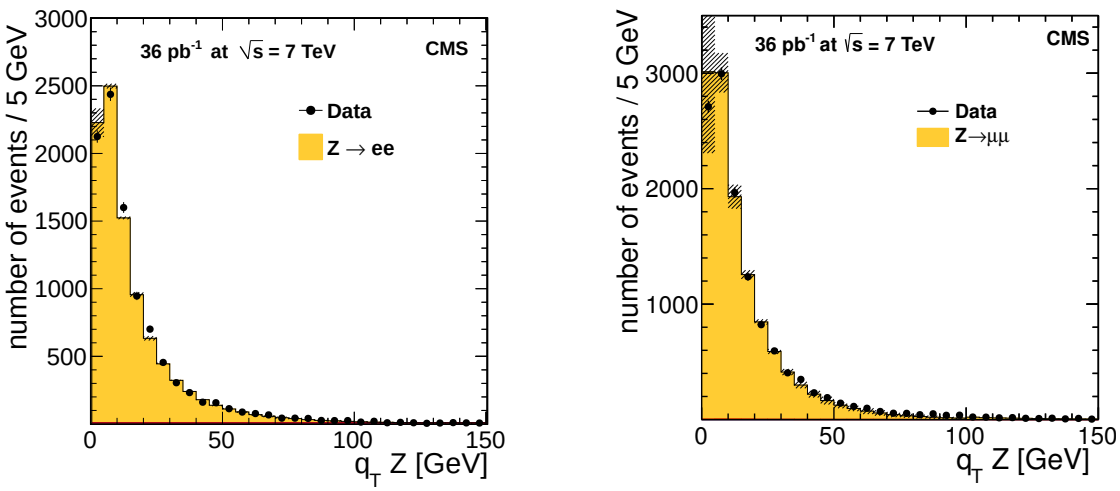

Figure 8: The q_T distribution for Z boson candidates in (left) the electron channel and (right) the muon channel, along with the prediction from simulation. Systematic uncertainties are shown as grey bands.

6.3 Scale and resolution for events with one primary vertex

To study the $\not{E}_T$ scale and resolution, we decompose the recoil with respect to the boson (γ or Z) direction in the transverse plane. We restrict ourselves to events containing one reconstructed primary vertex. Z yields are thus reduced to 2611 $Z \to e^+e^-$ candidates and 2438 $Z \to \mu^+\mu^-$ candidates. The effect of pile-up on the scale and the resolution is studied in Section 6.5.1. Distributions of the components of the recoil calculated from PF $\not{E}_T$ that are parallel and perpendicular to the boson axis, $u_{\parallel}$ and $u_{\perp}$, are shown in Fig. 9 for direct photon candidates, $Z \to e^+e^-$ candidates, and $Z \to \mu^+\mu^-$ candidates. As expected, the parallel component is mainly negative, consistent with the back-to-back nature of the events, while the perpendicular component is symmetric.

The distributions are corrected for the residual contamination ($5 \pm 1\%$) from events with more

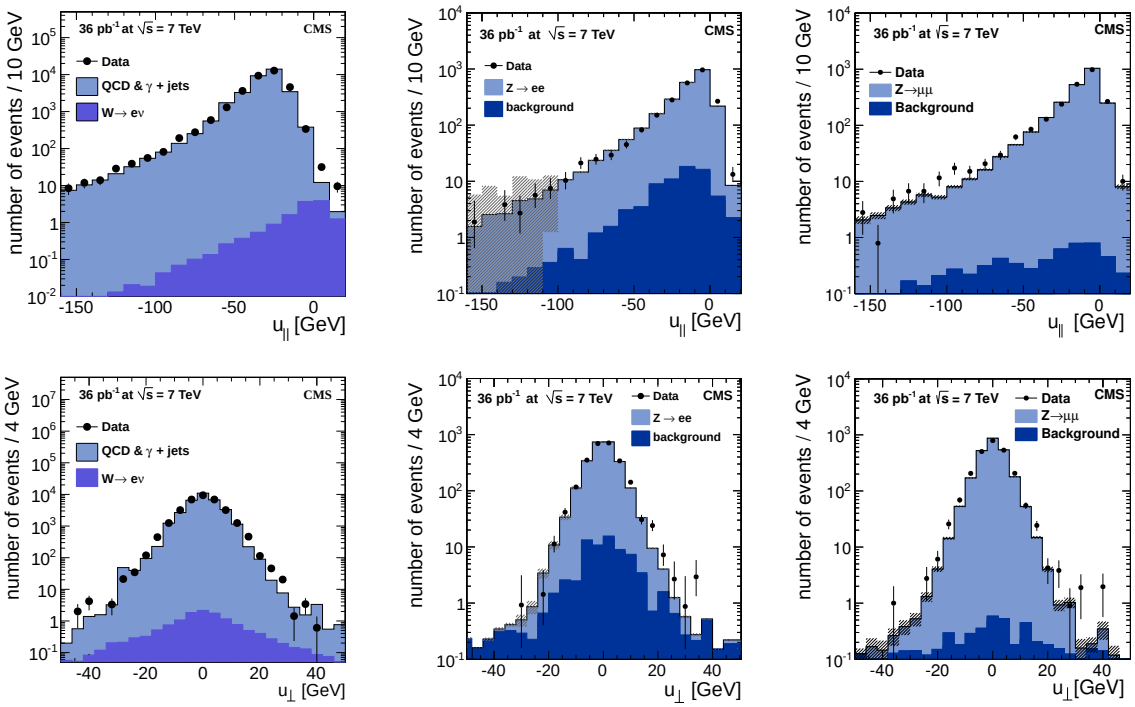

Figure 9: $u_{\parallel}$ distributions for PF $\not{E}_{\mathrm{T}}$ for (top, left) γ, (top, middle) $\mathrm{Z} \to \mathrm{e}^{+}\mathrm{e}^{-}$ and (top, right) $\mathrm{Z} \to \mu^{+}\mu^{-}$ events; $u_{\perp}$ distributions for PF $\not{E}_{\mathrm{T}}$ for (bottom, left) γ, (bottom, middle) $\mathrm{Z} \to \mathrm{e}^{+}\mathrm{e}^{-}$, and (bottom, right) $\mathrm{Z} \to \mu^{+}\mu^{-}$ events. Distributions are for events containing one PV, with a correction for residual pile-up contamination. Statistical uncertainties and systematic uncertainties on the removal of events with more-than-one PV and on the boson q_{T} spectrum are shown as grey bands on the prediction from simulation. QCD refers to multijet production.

than one interaction. The number of events with more than one scattering that are reconstructed as a single PV is estimated by convoluting the efficiency for reconstructing two vertices as a function of the vertex separation with the z distribution of vertices. The distributions are corrected for this contamination by subtracting multi-vertex-event shapes obtained from data, rescaled to the estimated contamination, from the distribution from events with one PV. The systematic uncertainty on the residual contamination is obtained by varying the normalization within its uncertainties.

Events generated with PYTHIA are reweighted so that the q_{T} spectrum matches that predicted by the RESBOS Monte Carlo program [21], in order to take advantage of its resummed calculation of the boson q_{T} spectrum. The systematic uncertainties due to our imperfect knowledge of the true q_{T} distributions for Z bosons are estimated from the difference between the q_{T} distributions predicted by PYTHIA and RESBOS. We set the systematic uncertainty, bin-by-bin in q_{T}, equal to this difference.

In addition, there is a systematic uncertainty on the prediction from the simulation due to the size of the simulation samples. In Fig. 9, the dominant uncertainty on $u_{\parallel}$ for the part of the distribution from the electron channel with $u_{\parallel} < -100$GeV is from this source and from uncertainties on the removal of the multi-PV contamination.

Figure 10 shows the response curves, $|\langle u_{\parallel} \rangle| / q_{\mathrm{T}}$ versus q_{T}, extracted from data, for the three $\not{E}_{\mathrm{T}}$ reconstruction algorithms, Calo $\not{E}_{\mathrm{T}}$, TC $\not{E}_{\mathrm{T}}$, and PF $\not{E}_{\mathrm{T}}$ for γ, $\mathrm{Z} \to \mathrm{e}^{+}\mathrm{e}^{-}$, and $\mathrm{Z} \to \mu^{+}\mu^{-}$ samples. The agreement in response between the different samples is good. The agreement

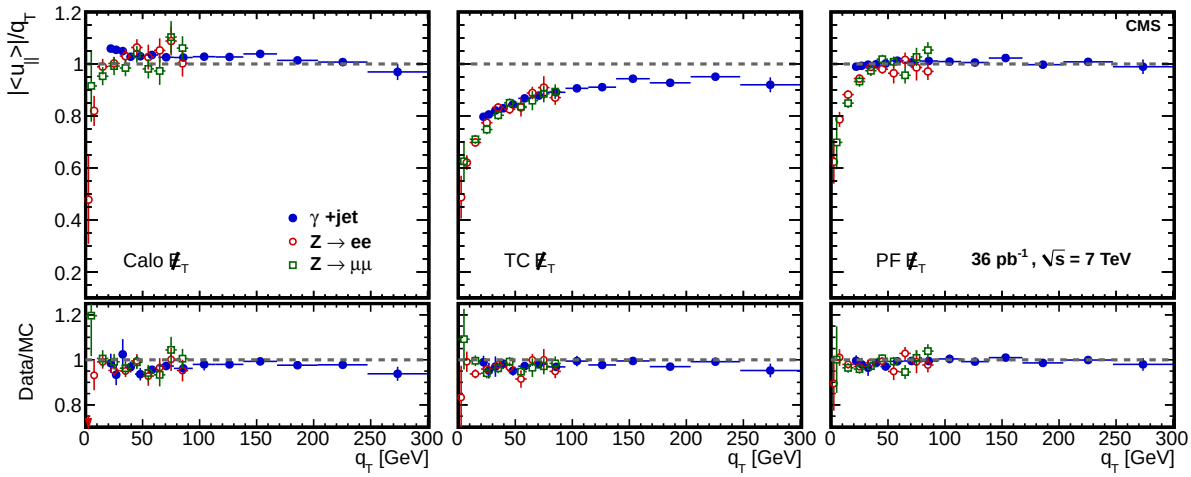

Figure 10: Response curves for events with one primary vertex, for (left) Calo $\not\!\!E_T$, (middle) TC $\not\!\!E_T$, and (right) PF $\not\!\!E_T$. Results are shown for photon events (full blue circles), $Z \to e^+e^-$ events (open red circles) and $Z \to \mu^+\mu^-$ events (open green squares). The upper frame of each figure shows the response in data; the lower frame shows the ratio of data to simulation. The vertical axis labels at the far left apply to all three subfigures.

between data and simulation is good, and the results indicate that the three reconstruction algorithms are distinct in their capabilities, performing differently in the recovery of hadronic activity in the detector. The response for Calo $\not\!\!E_T$ is slightly larger than one because the jet energy scale used in the type-I corrections was determined from a sample with a mixture of quark and gluon jets, while for these samples the leading jet is primarily a quark jet. The TC $\not\!\!E_T$ response is lower because it has neither type-I nor type-II corrections. The PF $\not\!\!E_T$ response is lower than the Calo $\not\!\!E_T$ response at low values of q_T because Calo $\not\!\!E_T$ has type-II corrections

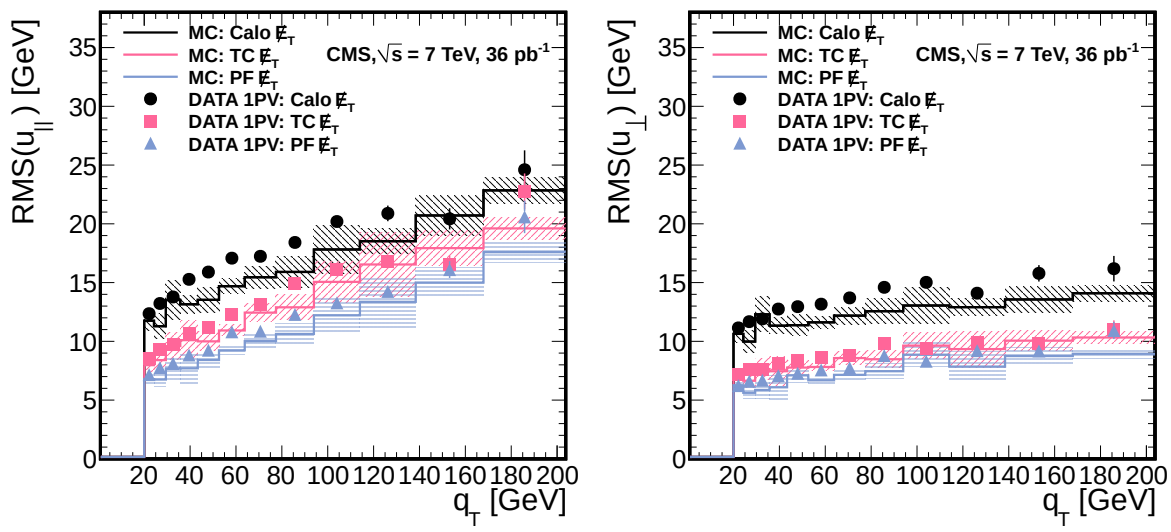

Figure 11: Resolution curves for components of hadronic recoil measured in direct photon candidate events with one primary vertex. (left) parallel to boson; (right) perpendicular to boson. Data and simulation are indicated by points and histograms, respectively. Black circles (upper): Calo $\not\!\!E_T$; Pink squares (middle): TC $\not\!\!E_T$; Blue triangles (bottom): PF $\not\!\!E_T$. Shaded regions indicate statistical uncertainties on the simulation.

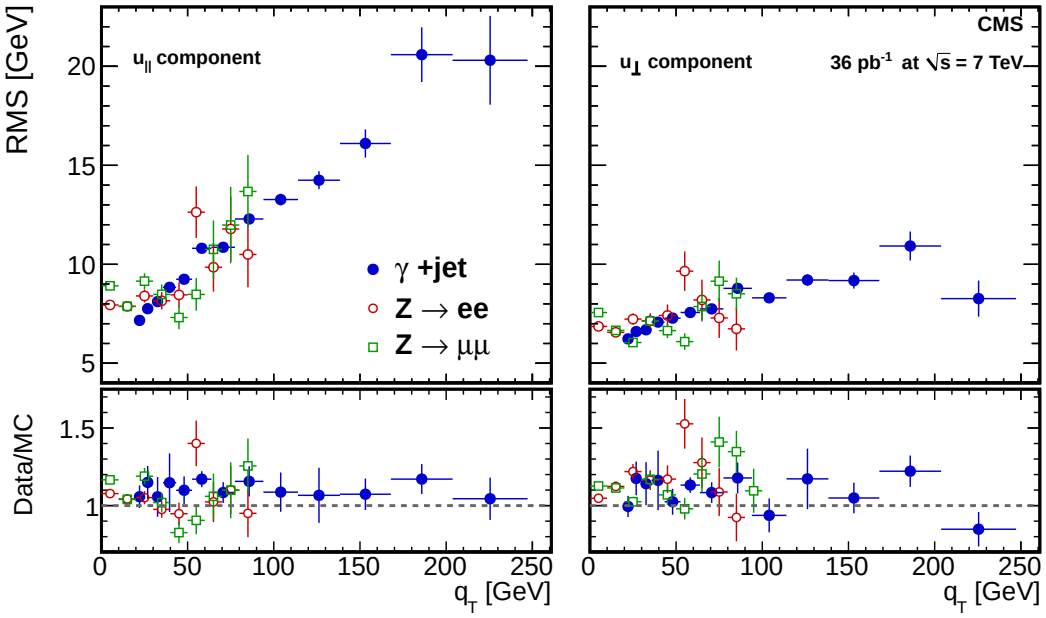

Figure 12: Resolution curves for components of hadronic recoil calculated using PF $\not{E}_T$ measured in events with one primary vertex. Left: parallel to boson; right: perpendicular to boson. $Z \to \mu^+\mu^-$, $Z \to e^+e^-$ and γ events are indicated by open green squares, open red circles and full blue circles, respectively. The lower frame indicates the ratio of data to simulation. The vertical axis labels at the far left apply to both subfigures.

while PF $\not{E}_T$ has only type-I corrections.

Figure 11 shows the resolution curves from photon candidate events for $u_{\parallel}$ and $u_{\perp}$ for data and simulation, for all three reconstruction algorithms. Figure 12 shows the resolution as measured in γ, $Z \to e^+e^-$, and $Z \to \mu^+\mu^-$ events for PF $\not{E}_T$. The measured resolution must be corrected for the scale to avoid a misleading result; e.g., the apparent resolution on $u_{\perp}$ is proportional to the scale and therefore an algorithm with a scale that is smaller than unity could appear to have a better resolution than one with a scale of unity without such a correction. Since only Calo $\not{E}_T$ has been corrected fully for the detector response with both type-I and type-II corrections, the resolution measurements are rescaled, bin by bin, using the corresponding response curves of Fig. 10. The data confirm the prediction from simulation that tracking information significantly enhances the $\vec{\not{E}}_T$ resolution. The resolutions as measured in the different samples are in good agreement, but are $\approx$ 10% worse than expected from the simulation. A similar difference in resolution for jets for the 2010 run is documented in [14]. The small discrepancies between data and simulation shown in Fig. 9 are due to this difference.

6.4 Resolution in multijet events

The $\not{E}_T$ resolution can also be evaluated in events with a purely hadronic final state, where the observed $\not{E}_T$ arises solely from resolution effects. Because the $\not{E}_T$ resolution has a strong dependence on the associated $\sum E_T$, it is presented as a function of $\sum E_T$. We characterize the $\vec{\not{E}}_T$ resolution using the σ of a Gaussian fit to the distribution of the x and y components of $\vec{\not{E}}_T$ ($\not{E}_{x,y}$). In order to make a meaningful comparison, we calibrate the measured $\not{E}_T$ for the different algorithms to the same scale using the response from Fig. 10. These corrections would not be needed if all types of $\vec{\not{E}}_T$ had both type-I and type-II corrections.

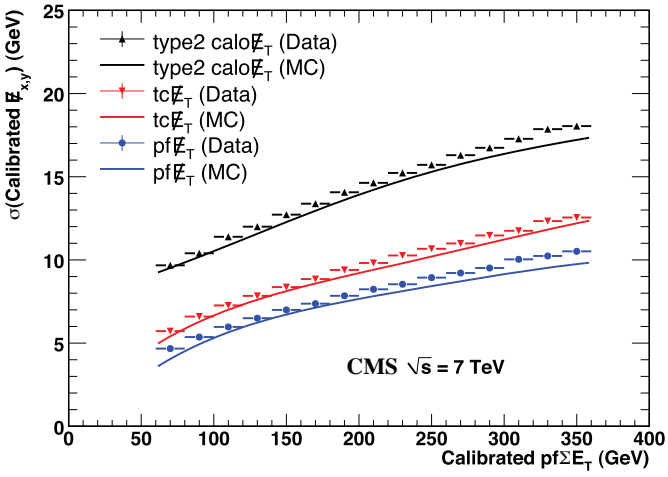

Figure 13: Calibrated $\not{E}_{x,y}$ resolution versus calibrated PF $\sum E_T$ for Calo $\not{E}_T$, TC $\not{E}_T$, and PF $\not{E}_T$ in data and in simulation.

For $\sum E_T$, we use the PF $\sum E_T$ as measured by the particle-flow algorithm for all types of $\not{E}_T$, as it gives the best estimate of the true $\sum E_T$, and hence is an accurate evaluation of the event activity. We use PF $\sum E_T$ for all algorithms to ensure their measure is the same. We calibrate PF $\sum E_T$ to the particle-level $\sum E_T$, on average, using the predicted average mean value as a function of the particle-level $\sum E_T$ from a simulation of events from the PYTHIA 8 event generator [22].

Figure 13 shows the calibrated $\not{E}_{x,y}$ Gaussian core resolution versus the calibrated PF $\sum E_T$ for different $\not{E}_T$ reconstruction algorithms in events containing at least two jets with $p_T > 25$ GeV. Both TC $\not{E}_T$ and PF $\not{E}_T$ show improvements in the $\not{E}_T$ resolution compared to the Calo $\not{E}_T$, and the PF $\not{E}_T$ yields the smallest $\not{E}_T$ resolution.

Figure 14 shows the PF $\not{E}_T$ distributions for different intervals of Calo $\sum E_T$ and for jet multiplicities varying from two to four, normalized to the same area. The jets are required to be above a p_T-threshold of 20 GeV. The good agreement of the normalized shapes in Fig. 14 indicates that PF $\not{E}_T$-performance in events without genuine $\not{E}_T$ is driven by the total amount of calorimetric activity (parametrized by Calo $\sum E_T$) and no residual non-linear contribution from jets to PF $\not{E}_T$ is visible. Similar behaviour is also observed for Calo $\not{E}_T$ and TC $\not{E}_T$.

6.5 Effect of multiple interactions

Pile-up, namely multiple proton collisions within the same bunch crossing, occurs because of high LHC bunch currents and can play an important role in $\vec{\not{E}}_T$ performance.

Because there is no true $\vec{\not{E}}_T$ in minimum bias events and because the average value for a component of $\vec{\not{E}}_T$ in these events is zero (e.g., the x or y component), pile-up should have only a small effect on the scale of the component of the measured $\vec{\not{E}}_T$ projected along the true $\vec{\not{E}}_T$ direction. Pile-up, however, will have a considerable effect on the resolution of the parallel and perpendicular components.

We investigate the effect of pile-up using multijet samples, γ, and Z data.

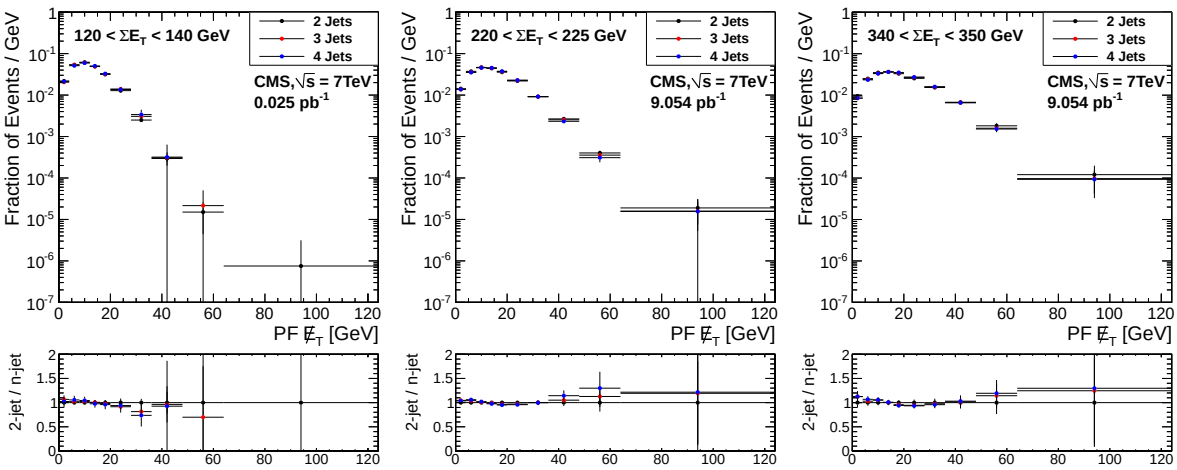

Figure 14: PF $\not\!\!E_{\mathrm{T}}$ distributions in 2-, 3- and 4-jet events, in selected Calo $\sum E_{\mathrm{T}}$ bins.

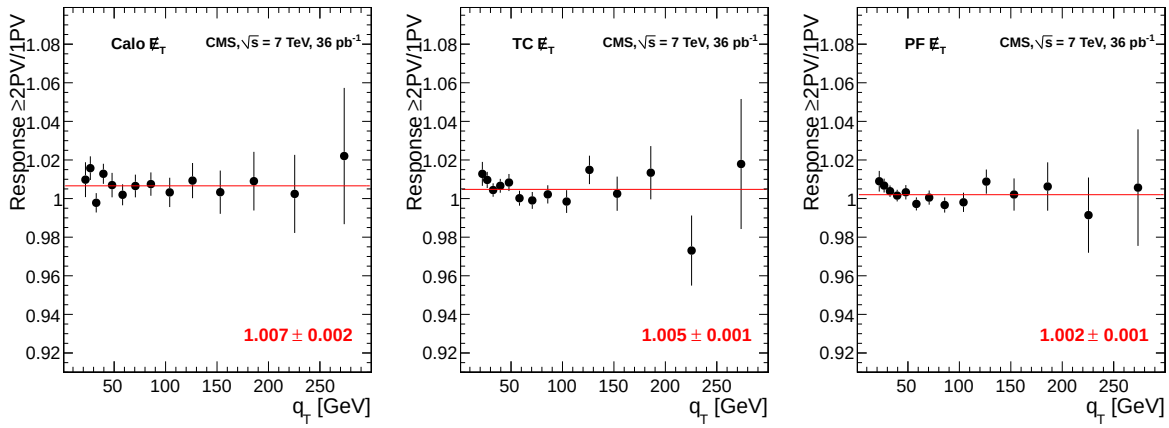

Figure 15: The ratio of the response for the component of the induced $\vec{\not\!\!E}_{\mathrm{T}}$ along the boson direction, measured in γ events for events containing 1 PV and at least 2 PVs for (left) Calo $\not\!\!E_{\mathrm{T}}$, (middle) TC $\not\!\!E_{\mathrm{T}}$, and (right) PF $\not\!\!E_{\mathrm{T}}$. Also given is the best fit value for the average ratio, which corresponds to the solid, red line.

6.5.1 Studies of pile-up effects using photon and Z events

In this section, we use samples containing a vector boson to measure the effect of pile-up on the scale and resolution of a component of $\vec{\not\!\!E}_{\mathrm{T}}$. Figure 15 shows the ratio of the response as measured in γ events for events containing 1 PV and at least 2 PVs. The ratio of the responses of the component of the measured $\vec{\not\!\!E}_{\mathrm{T}}$ along the boson direction is close to one, as expected. It is slightly larger at low q_{T} when pile-up is present. This is expected, as pile-up can reduce energy lost due to zero suppression in the readout of the calorimeter if energy from a pile-up interaction and from the hard scattering are both in the same readout channel. If the sum is larger than the zero suppression thresholds, more of the energy from the hard scattering is recorded.

Figure 16 shows the resolution versus the q_{T} of the γ for the components of the hadronic recoil parallel and perpendicular to the boson direction for 1, 2, and 3 reconstructed PVs. Also shown is the prediction from simulated γ events without pile-up. Figure 17 shows the resolution

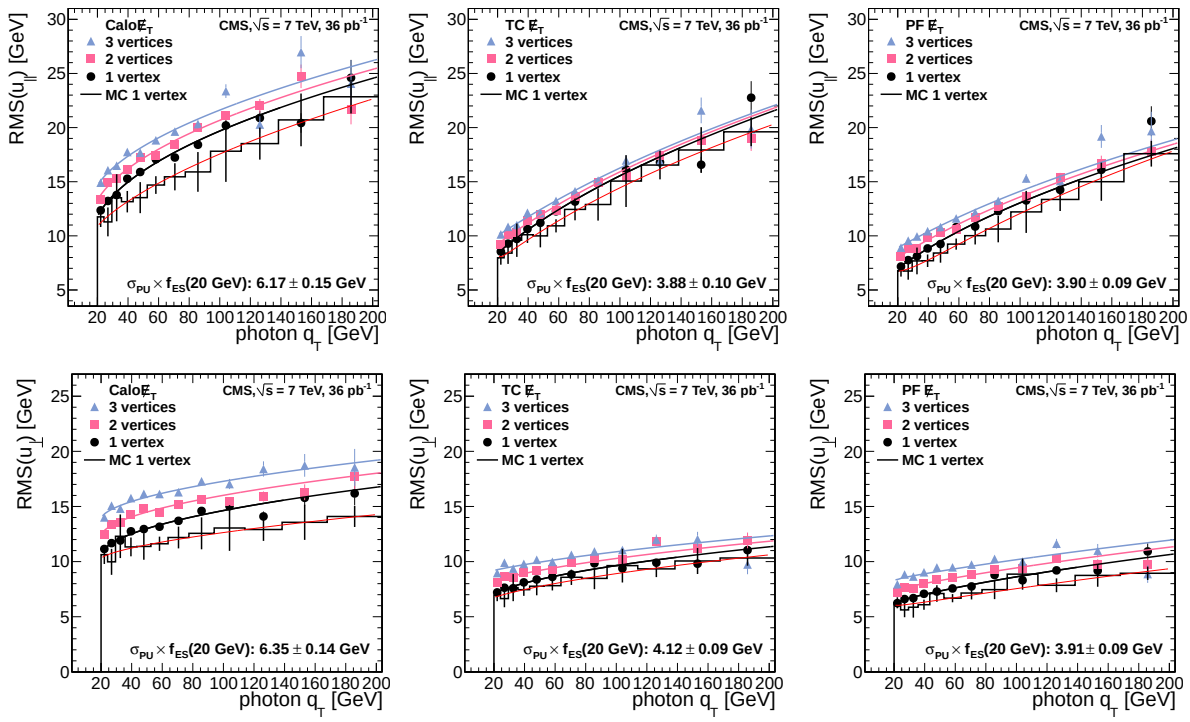

Figure 16: Resolution versus photon q_T for the parallel component (top) and perpendicular component (bottom) for (left to right) Calo $\not{E}_T$, TC $\not{E}_T$, and PF $\not{E}_T$, for events with 1 (circles), 2 (squares), and 3 (triangles) reconstructed primary vertices.

versus the q_T of the Z for the parallel and perpendicular components of the hadronic recoil. The parameterization of $\not{E}_T$ resolution used in Figs. 16 and 17 is given by :

$$\sigma^2_{\text{total}} = (a\sqrt{q_T} + b)^2 \; + \; (\sigma_{\text{noise}} f_{\text{ES}}(q_T))^2 + \; (N-1)\,(\sigma_{\text{PU}} f_{\text{ES}}(q_T))^2 \tag{1}$$

where a and b characterize the hard process, σ_{noise} is the intrinsic noise resolution, N is the number of reconstructed vertices in the event, σ_{PU} is the intrinsic pile-up resolution, and $f_{\text{ES}}(q_T)$ is the energy scale correction applied on each event. At low q_T, the resolution is dominated by contributions from the underlying event and detector noise (σ_{noise}). Since these contributions can not be distinguished from those due to the particles from the recoil, and since the recoil measurement needs to be corrected for the detector response, these contributions are magnified and have a larger contribution at low boson q_T when energy scale corrections are applied. As expected, the resolution is degraded with increasing pile-up interactions. Results from the Z and γ channels are in agreement and are similar to the values obtained in Section 6.5.2 from jet data.

6.5.2 Studies of pile-up effects in jet data

In this Section, we study the behaviour of the PF $\not{E}_T$ distributions in samples containing high p_T jets when pile-up is present. The data are selected using a prescaled H_T trigger with a threshold of 100 GeV, where H_T is defined as the scalar sum of the transverse momenta of PF jets ($p_T > 20$ GeV, $|\eta| < 3$). Additionally, in the offline analysis, each event is required to have H_T (calculated using PF jets)$>$ 200 GeV to avoid bias from the trigger. Figure 18 shows that the widening of the PF $\not{E}_T$ distribution with increasing number of vertices can be modeled by convoluting the x-

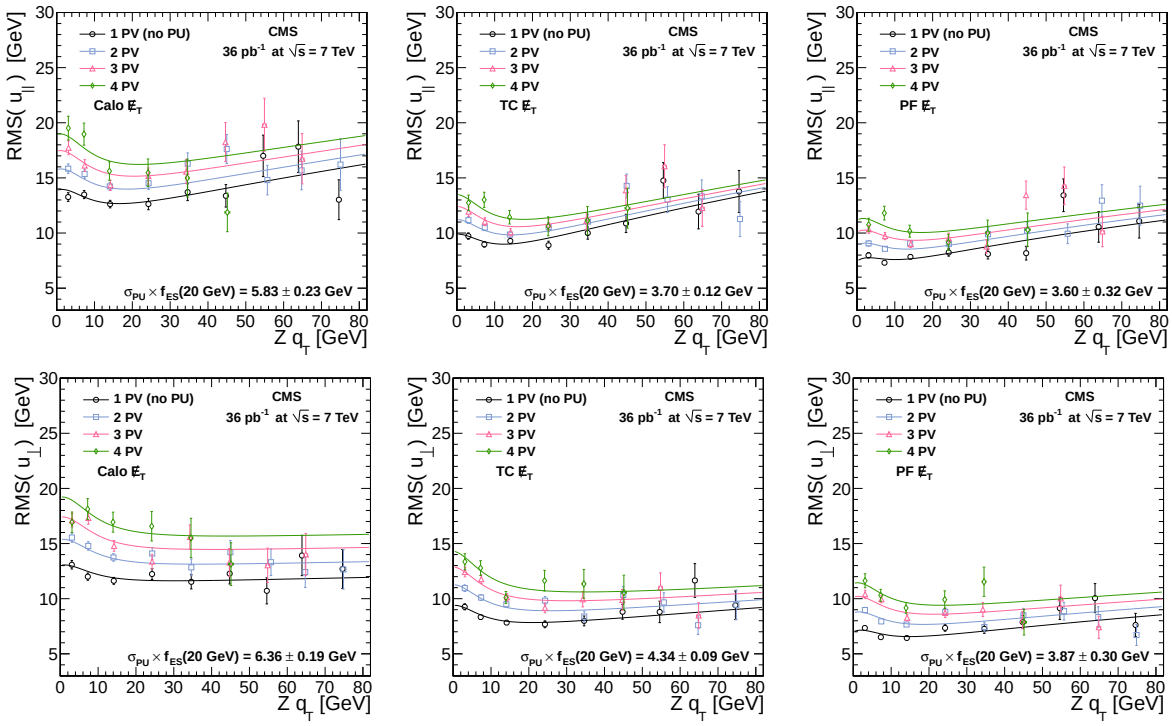

Figure 17: Resolution versus the q_T of the Z for the parallel component (top) and perpendicular component (bottom) for (left to right) Calo $\not{E}_T$, TC $\not{E}_T$, and PF $\not{E}_T$, for events with 1 (circles), 2 (squares), 3 (triangles), and 4 (diamonds) reconstructed primary vertices.

and y-components of the one-vertex $\not{E}_T$ shape with a Gaussian (G) whose mean is $(n-1) \cdot \Delta\mu_x$ and with standard deviation $\sqrt{n-1} \cdot \Delta\sigma_x$:

$$\not{E}_{T,n} = \sqrt{(\not{E}_{x1} \otimes G[(n-1) \cdot \Delta\mu_x, \sqrt{n-1} \cdot \Delta\sigma_x])^2 + (\not{E}_{y1} \otimes G[(n-1) \cdot \Delta\mu_y, \sqrt{n-1} \cdot \Delta\sigma_y])^2} \tag{2}$$

where $\not{E}_{x,y}$ are the x and y components of $\vec{\not{E}}_T$. Here we assume that each additional vertex contributes with a constant $\Delta\sigma_x$ ($\Delta\sigma_y$) to the $\not{E}_T$ resolution such that the resolution with n pile-up interactions is related to that with one primary vertex via: $\sigma^2_{xn} = \sigma^2_{x1} + (n-1)\Delta\sigma^2_x$. In addition we also allow for a linear shift of $\not{E}_x$ and $\not{E}_y$ by $\Delta\mu_x$ ($\Delta\mu_y$) such that $\mu_{xn} = \mu_{x1} + (n-1)\Delta\mu_x$. A fit of Eq. (2) to data results in $\Delta\sigma_x = \Delta\sigma_y = 3.7$ GeV, consistent with the results from Section 6.5.1. This fit is performed simultaneously on the $\not{E}_T$ distributions of events containing two to seven vertices. The shifts of the x and y $\not{E}_T$ components are estimated to be $\Delta\mu_x = 0.5$ GeV and $\Delta\mu_y = -0.3$ GeV respectively, which are small compared to $\Delta\sigma$ and are consistent with the expected shift seen in simulation due to non-functional channels.

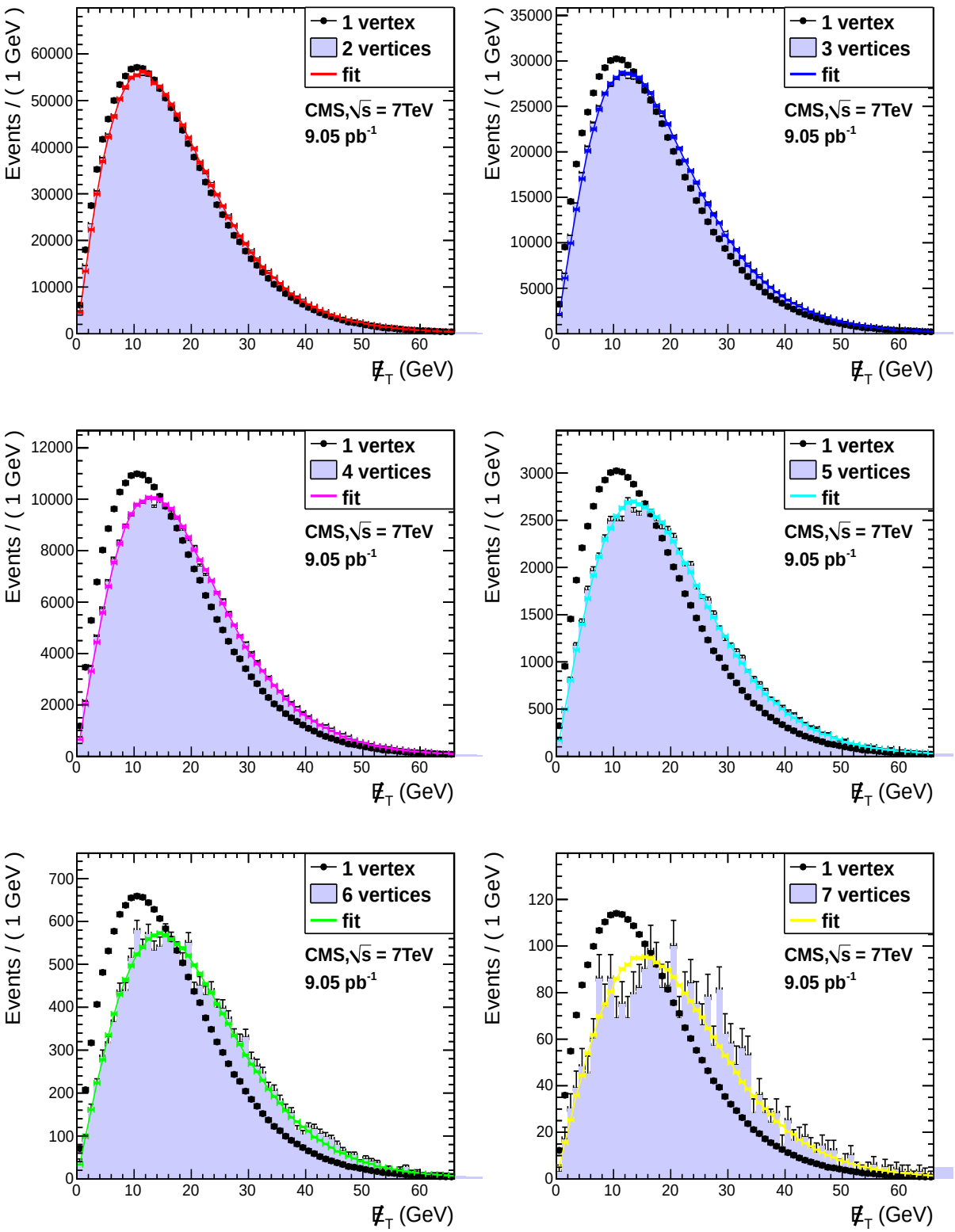

Figure 18: PF $\not{E}_T$ distributions in pile-up events. The figures show a comparison between the one- and n-vertex shapes ($n = 2...7$) and the results of a simultaneous fit of Eq. (2) to the n-vertex shapes. The one-vertex distribution is normalized to the n-vertex distribution for each plot.

7 Studies of physics processes containing genuine $\not{E}_T$

In this section, we examine distributions relevant to $\vec{\not{E}}_T$ in events containing neutrinos. Events containing W bosons and b quarks are studied.

7.1 W events

The performance of $\not{E}_T$ is studied in events that contain large, genuine $\not{E}_T$: $W \to \ell\nu$ events, where ℓ is a muon or electron. For most W events, the magnitude of $\vec{\not{E}}_T$ is approximately equal to the p_T of the charged lepton, but its resolution is dominated by the hadronic recoil. When the W q_T is small compared to the W mass, the $\not{E}_T$ is approximately

$$\not{E}_T \approx p_T(\ell) - 0.5u_\ell$$

where u_ℓ is the component of the recoil parallel to the lepton transverse direction.

In the $W \to \mu\nu$ decay channel, events are required to have been collected by a single-muon high-level trigger. In addition, candidates are selected by requiring a muon with $|\eta| < 2.1$ that has $p_T > 25$ GeV. Events with a second muon with $p_T > 25$ GeV are rejected to suppress Z and $t\bar{t}$ contamination. $W \to e\nu$ decays are identified using similar selection criteria. A single-electron high-level trigger requirement with a p_T threshold of 15 GeV is applied. Events are also required to contain an electron with $p_T > 25$ GeV. Events with a second electron with $p_T > 20$ GeV are rejected, and rejection against γ conversions is applied. A total of 24 628 (29 200) $W \to \mu\nu$ ($W \to e\nu$) events with only one primary vertex are selected.

The main sources of background to the $W \to \ell\nu$ signal are jet events with one jet falsely identified as a high-p_T muon or electron and $Z \to \ell\ell$ events with one lepton escaping detection. The jet events usually have low values of $\not{E}_T$. The apparent $\not{E}_T$ in these events (that have no genuine $\not{E}_T$) is amplified by scale corrections to the $\not{E}_T$ (type-I and type-II) because, since they are indistinguishable, artificial $\not{E}_T$ receives the same scale correction factor as genuine $\not{E}_T$, and genuine $\not{E}_T$ tends to be underestimated without corrections. Other backgrounds include W and Z bosons decaying into τ, followed by $\tau \to \ell\nu\bar{\nu}$, and $t\bar{t}$ events, with one top quark decaying semi-leptonically. The relative normalization of the different electroweak (EWK) signal simulation event ensembles, and simulations of those backgrounds that contain an electroweak boson ($W \to \ell\nu$, $Z \to \ell\ell$, $t\bar{t}$), are set by the ratios of their theoretical cross sections computed at next-to-leading order [23]. The normalization of the composite EWK and the QCD contributions are established through a one-parameter binned fit to the $\not{E}_T$ distribution from data.

Figure 19 shows the PF $\not{E}_T$ distribution for the $W \to e\nu$ and $W \to \mu\nu$ candidate samples, along with the expectation from simulation. As for the analyses using Z events, the background distributions include a grey-shaded band indicating the estimated uncertainty due to the size of the simulation samples, modeling of the W q_T spectrum, and the pile-up correction procedure. In most cases this uncertainty is too small to be visible. Data and simulation agree well, and the W shows up prominently as expected.

Figure 19 also shows the u_T distribution. To suppress QCD background, for the u_T studies only, we further require that the W candidate pass a requirement on the transverse mass, defined as $M_T = \sqrt{p_T(\ell) \cdot \not{E}_T \cdot (1 - \cos\Delta\phi)}$, where $\Delta\phi$ is the opening angle in the transverse plane between the lepton candidate and the $\vec{\not{E}}_T$. We require $M_T > 50$ GeV, and a minimum $\not{E}_T$ threshold, $\not{E}_T > 25$ GeV. The $\not{E}_T$ resolution has substantial contributions from the mismeasurement of the many particles in the underlying event. These contributions can be more

clearly seen in the u_T distribution, since they are not obscured by the contributions from the charged lepton. Again we see reasonable agreement between data and simulation.

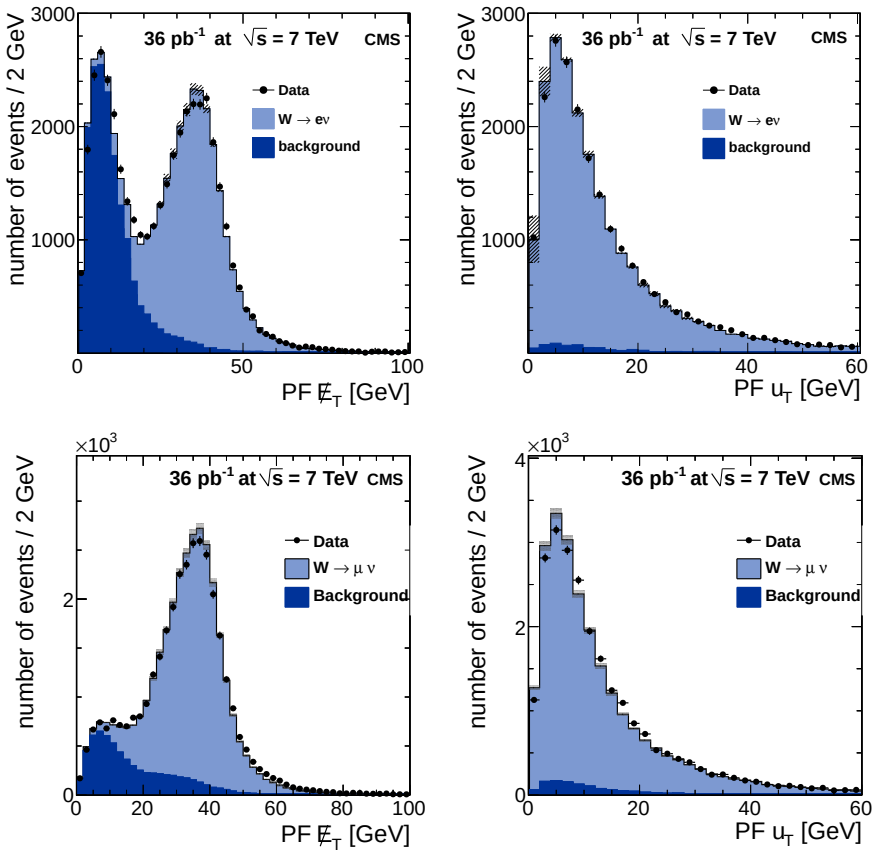

Figure 19: The PF $\not{E}_T$ (left) and $|u_T|$ (right) distribution in $W \to e\nu$ (top) and $W \to \mu\nu$ (bottom) candidate events. Both data (points) and simulation (solid lines) are shown. The plots on the right include selection requirements on $\not{E}_T$ and M_T, while those on the left do not.

7.2 Heavy flavour production and $\not{E}_T$

The $\not{E}_T$ distributions from jet samples containing b quarks can differ from those of inclusive jet samples because the B hadrons have unique fragmentation properties, and sometimes their final states contain neutrinos. Neutrinos from b jets are one of the main sources of severe underestimations of jet energies (the other main source is the ECAL masked channels discussed in Section 5.3). In this section, we study the induced $\not{E}_T$ in an inclusive b-tagged jet sample.

We compare the $\not{E}_T$ distributions in dijet events with and without a secondary vertex, *i.e.*, events where the leading jet has a positive SSV (displaced vertex) tag or a SMbyPt (lepton) tag [7, 8] (Section 3 includes a description of these algorithms). Since these taggers rely on tracking information, we require that the leading jet has $|\eta| < 2.1$. Also, we require the leading two jets to have $p_T > 40$ GeV. Below this value, the b-quark tagging purity is significantly reduced. A prescaled jet trigger with a p_T threshold of 15 GeV was used; the resulting sample corresponds to an integrated luminosity of 0.025 pb^{-1}. Figure 20 shows the fraction of events from this sample with a b-tagged jet as a function of $\not{E}_T$ for the two tagging algorithms. The larger increase in the fraction of b-tagged events at large $\not{E}_T$ for SMbyPt than for SSV is due, in part, to the higher probability of neutrinos in leptonically tagged events.

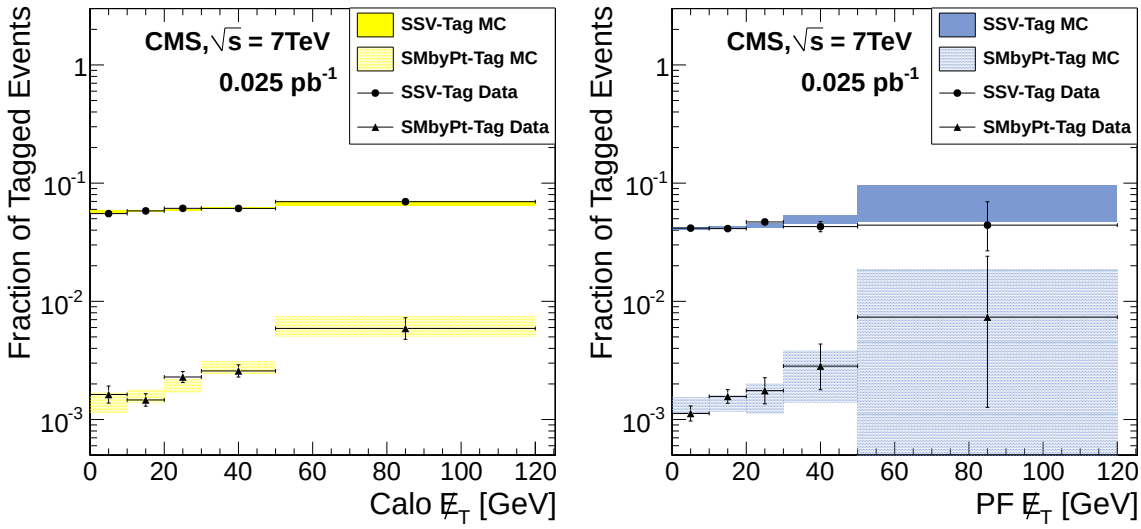

Figure 20: Fraction of events in a jet sample that contain a jet tagged as a b jet by the SSV- and SMbyPt-taggers for (left) Calo $\not{E}_T$ and (right) PF $\not{E}_T$.

8 $\not{E}_T$ significance

A spurious nonzero $\vec{\not{E}}_T$ in an event can have contributions from many sources, including measurement resolution, reconstruction inefficiencies, instrumental defects, and improper pattern recognition. Events in which the reconstructed $\vec{\not{E}}_T$ is consistent with contributions solely from particle-measurement resolutions and efficiencies can be identified by evaluating the $\vec{\not{E}}_T$ significance, $\mathcal{S}$. The significance offers an event-by-event assessment of the likelihood that the observed $\not{E}_T$ is consistent with zero given the reconstructed content of the event and known measurement resolutions. A similar variable used by the CDF collaboration is described in [24].

8.1 Definition

The significance requires evaluation of the uncertainty in the total measured transverse energy, which is given by

$$\vec{E}_T^{\,\text{total}} = \sum_{i \in X} \vec{E}_{T_i} = -\vec{\not{E}}_T, \tag{3}$$

where $\vec{E}_{T_i} = (E_{x_i}, E_{y_i})$ is the measured transverse momentum of the ith reconstructed object. X is the set of reconstructed objects, such as calorimeter towers (for Calo $\not{E}_T$) or PF particles (for PF $\not{E}_T$), used to calculate $\not{E}_T$. In the derivation of the significance, there are three relevant quantities for each object in the sum. The first of these is $\vec{e}_{T_i}$, the true transverse momentum of the object. The significance provides a measure of whether an event is consistent with the null hypothesis of zero genuine total transverse momentum. Under this hypothesis, $\sum_{i \in X} \vec{e}_{T_i} = 0$. The second is $\vec{E}_{T_i}$, the measured transverse momentum of the object, which is distributed according to $P_i(\vec{E}_{T_i}|\vec{e}_{T_i})$, the probability density function (pdf) for observing the measured transverse momentum given the true transverse momentum of the object. The third is $\vec{\varepsilon}_i = \vec{E}_{T_i} - \vec{e}_{T_i}$. For convenience, we define an equivalent pdf in terms of this difference: $p_i(\vec{\varepsilon}_i|\vec{e}_{T_i}) \equiv P_i(\vec{\varepsilon}_i + \vec{e}_{T_i}|\vec{e}_{T_i})$. Given the null hypothesis, $\sum \vec{E}_{T_i} = \sum \vec{\varepsilon}_i$, so that the ith reconstructed object contributes $\vec{\varepsilon}_i$ to the

measured total transverse momentum.

We first introduce the likelihood that we would observe a total transverse momentum $\vec{\varepsilon}$ under our null hypothesis. For the two object case, the likelihood function is given by

$$\begin{aligned}\mathcal{L}(\vec{\varepsilon}) &= \int P_1(\vec{E}_{\mathrm{T}_1}|\vec{e}_{\mathrm{T}_1}))P_2(\vec{E}_{\mathrm{T}_2}|\vec{e}_{\mathrm{T}_2}))\delta(\vec{\varepsilon}-(\vec{E}_{\mathrm{T}_1}+\vec{E}_{\mathrm{T}_2}))\,d\vec{E}_{\mathrm{T}_2}\,d\vec{E}_{\mathrm{T}_2} \\ &= \int p_1(\vec{\varepsilon}_1|\vec{e}_{\mathrm{T}_1})p_2(\vec{\varepsilon}_2|\vec{e}_{\mathrm{T}_2})\delta(\vec{\varepsilon}-(\vec{\varepsilon}_1+\vec{e}_{\mathrm{T}_1}+\vec{\varepsilon}_2+\vec{e}_{\mathrm{T}_2}))\,d\vec{\varepsilon}_1\,d\vec{\varepsilon}_2 \\ &= \int p_1(\vec{\varepsilon}_1|\vec{e}_{\mathrm{T}_1})p_2(\vec{\varepsilon}_2|\vec{e}_{\mathrm{T}_2})\delta(\vec{\varepsilon}-(\vec{\varepsilon}_1+\vec{\varepsilon}_2))\,d\vec{\varepsilon}_1\,d\vec{\varepsilon}_2, \end{aligned} \tag{4}$$

since $0 = \sum_i \vec{e}_{\mathrm{T_i}} = \vec{e}_{\mathrm{T}_1} + \vec{e}_{\mathrm{T}_2}$. For an arbitrary number of input objects, the full likelihood function can be generated by a recursive application of Eq. (4). The significance is defined as the log-likelihood ratio

$$\mathcal{S} \equiv 2\ln\left(\frac{\mathcal{L}(\vec{\varepsilon}=\sum\vec{\varepsilon}_i)}{\mathcal{L}(\vec{\varepsilon}=0)}\right), \tag{5}$$

which compares the likelihood of measuring the total observed $\vec{E}_{\mathrm{T}}^{\mathrm{total}} = \sum\vec{E}_{\mathrm{T_i}} = \sum\vec{\varepsilon}_i$ to the likelihood of the null hypothesis, $\vec{E}_{\mathrm{T}}^{\mathrm{total}} = 0$.

This formulation is completely general and accommodates any probability distribution function. In practice, however, we often employ Gaussian uncertainties for measured quantities, for which the integrals of Eq. (4) can be done analytically. The Gaussian probability density function is given by

$$p_i(\vec{\varepsilon}_i|\vec{e}_{\mathrm{T_i}}) \sim \exp\left(-\frac{1}{2}(\vec{\varepsilon}_i)^T\mathbf{V}_i^{-1}(\vec{\varepsilon}_i)\right),$$

where $\mathbf{V}_i$ is the 2×2 covariance matrix associated with the ith measurement. The integration of Eq. (4) yields

$$\mathcal{L}(\vec{\varepsilon}) \sim \exp\left(-\frac{1}{2}(\vec{\varepsilon})^T\,\mathbf{V}^{-1}\,(\vec{\varepsilon})\right)$$

with $\mathbf{V} = \mathbf{V}_1 + \mathbf{V}_2$. When many measurements contribute, the expression generalizes to

$$\mathcal{L}(\vec{\varepsilon}) \sim \exp\left(-\frac{1}{2}(\vec{\varepsilon})^T\left(\sum_i \mathbf{V}_i\right)^{-1}(\vec{\varepsilon})\right). \tag{6}$$

The covariance matrix $\mathbf{U}_i$ for each reconstructed object in the $\vec{E}_{\mathrm{T}}$ sum is initially specified in a natural coordinate system having one axis aligned with the measured $\vec{E}_{\mathrm{T_i}}$ vector, $\vec{E}_{\mathrm{T_i}} \equiv (E_{T_i}\cos\phi_i,\, E_{T_i}\sin\phi_i)$:

$$\mathbf{U}_i = \begin{pmatrix} \sigma^2_{E_{T_i}} & 0 \\ 0 & E^2_{T_i}\sigma^2_{\phi_i} \end{pmatrix}. \tag{7}$$

(We adopt the simplifying assumption that E_{T} and ϕ measurements are uncorrelated.) This matrix is rotated into the standard CMS $x - y$ reference frame to give the error matrix

$$\mathbf{V}_i = R(\phi_i)\mathbf{U}_i R^{-1}(\phi_i), \tag{8}$$

where $R(\phi_i)$ is the rotation matrix. The $\mathcal{S}$-matrix summation is then performed in this common reference frame. Combining Eqs. (5), (6), and (8) yields

$$\mathcal{S} = \left(\sum_{i \in X} \vec{E}_{\mathrm{T_i}}\right)^T \left(\sum_{i \in X} R(\phi_i)\mathbf{U}_i R^{-1}(\phi_i)\right)^{-1} \left(\sum_{i \in X} \vec{E}_{\mathrm{T_i}}\right). \tag{9}$$

Equation (9) makes explicit the dependence of $\mathcal{S}$ and $\vec{\not{E}}_{\mathrm{T}}$ on the set of objects X over which the vectors and matrices are summed. In general $\mathcal{S}$ is small when the $\not{E}_{\mathrm{T}}$ can be attributed to measurement resolution, and large otherwise.

In the Gaussian case, $\mathcal{S}$ is simply a χ^2 with two degrees of freedom. If we rotate into a coordinate system with the x axis parallel to the $\vec{\not{E}}_{\mathrm{T}}$ axis, instead of the CMS horizontal axis, then Eq. (9) is simplified to $\mathcal{S} = E_T^2/(\sigma_{E_T}^2(1-\rho^2))$, where $\sigma_{E_T}^2$ is the variance of the magnitude of $\vec{\not{E}}_{\mathrm{T}}$, and ρ is the correlation coefficient between the variances parallel to and perpendicular to the measured $\vec{\not{E}}_{\mathrm{T}}$. This form emphasizes the essential meaning of $\mathcal{S}$, but obscures the important feature that, through its denominator, $\mathcal{S}$ embodies the full topological information in the event. Essential features such as the angles between the measured $\vec{\not{E}}_{\mathrm{T}}$ and the reconstructed objects in the event are embedded in the definition of the denominator. This form also makes apparent the relationship between the true significance (in the Gaussian limit) and the more naive measure $\Sigma = \not{E}_{\mathrm{T}}/\sqrt{\sum E_{\mathrm{T}}}$.

The specialization to a Gaussian probability density function is less restrictive than it may appear, as any probability density function expressible as a linear combination of Gaussians is accommodated by the formalism presented here.

To apply Eq. (9) to PF $\not{E}_{\mathrm{T}}$ significance, we note that the Gaussian pdf only accommodates measurement resolution. Using only reconstructed PF particles to determine the covariance matrix would neglect fluctuations in the measured PF particle content itself. These fluctuations arise from finite detection and reconstruction efficiencies, and provide a non-negligible contribution to the PF $\not{E}_{\mathrm{T}}$ resolution. These fluctuations, however, also affect the PF jet resolutions. We can therefore substitute the PF jet resolutions for the combined measurement resolutions of the PF particles that have been clustered into jets. Hence the sum of covariance matrices in Eq. (9) includes contributions from PF jets, PF particles that were not considered during jet finding (e.g. isolated leptons), and PF particles that are not clustered into any jet. This approach inherently takes into account the contributions both from measurement resolution and from fluctuations in the reconstructed particle content.

The covariance matrices $\mathbf{U}_i$ of Eq. (7) are obtained from our knowledge of the response of each type of PF particle or jet as a function of p_{T} and η. The charged hadron and muon resolutions are obtained on a particle-by-particle basis from the error matrix from the final track fit, and the resolutions for electrons are those obtained from studies of data samples of known resonances such as neutral pions, the Z, etc. The jet and photon resolutions are from simulation. No input resolutions were tuned based on the behaviour of the significance distribution itself.

8.2 Performance of $\mathcal{S}_{\mathrm{PF}}$ in dijet events

Because $\mathcal{S}_{\mathrm{PF}}$ is χ^2 distributed, it should exhibit a flat probability of χ^2, $\mathcal{P}(\chi^2)$, for two degrees of freedom in an event sample that nominally has no genuine $\not{E}_{\mathrm{T}}$. (That is, $1 - \mathcal{P}(\chi^2)$ is the standard cumulative distribution function of the χ^2 statistic for two degrees of freedom.) Dijet samples from pp collisions are dominated by such events.

We select dijet events by requiring at least two jets satisfying $|\eta| < 2.3$ and $p_{\mathrm{T}} > p_{\mathrm{T}}^{\mathrm{min}}$, with thresholds $p_{\mathrm{T}}^{\mathrm{min}}$ of 30 or 60 GeV. One of the jets above threshold must have been responsible for the event passing an HLT single-jet trigger. We use data collected with a 15 GeV trigger threshold for our 30 GeV dijet sample, and a 30 GeV trigger threshold for the 60 GeV dijet sample (Because of different prescale factors applied to the two trigger streams, the 60 GeV dijet sample is not a direct subset of the 30 GeV sample.)

We compare the $\mathcal{S}_{\mathrm{PF}}$ distributions, as well as their corresponding $\mathcal{P}(\chi^2)$ distributions, in data and simulation in Fig. 21 for both values of the $p_{\mathrm{T}}^{\mathrm{min}}$ threshold. The significance distribution very closely follows a pure exponential, and the $\mathcal{P}(\chi^2)$ distribution is populated quite uniformly between zero and unity in both data and simulation. There is a small peak at zero in $\mathcal{P}(\chi^2)$; simulation (Fig. 21) indicates that about half of this peak results from genuine $\not{E}_{\mathrm{T}}$ in the event sample. This $\not{E}_{\mathrm{T}}$ arises from a combination of sources such as the semileptonic decays of heavy quarks and the finite η acceptance of the detector. The data and simulation distributions match well in the 30 GeV threshold sample. MC studies show that the remainder of the excess of low probability events after accounting for genuine $\not{E}_{\mathrm{T}}$ typically have at least one high-p_T jet whose response is in the non-Gaussian tail of the response function.

To probe the stability of the $\mathcal{S}_{\mathrm{PF}}$ behaviour, we have studied dijet samples with different p_T^{min} thresholds, which changes the relative contributions of different detector regions in the covariance matrix calculations. We find that, overall, the $\mathcal{S}_{\mathrm{PF}}$ distributions for the bulk of the data continues to exhibit near-ideal behaviour independent of threshold. As the 60 GeV sample shown here demonstrates, though, the higher threshold data does begins to develop a larger tail in the significance, and a correspondingly larger peak at zero in $\mathcal{P}(\chi^2)$, than we find in the simulation. The discrepancy between data and MC is below the 0.2% level. Visual examination of the events with low probability reveal that the discrepancy arises from a combination of events with a residual anomalous energy contamination and other events with a high-p_T jet with activity straddling the endcap (HE) and forward (HF) calorimetry, for which the non-Gaussian tails are not yet perfectly modeled.

For the $\mathcal{S}_{\mathrm{PF}}$ distributions shown here, the transition point for use of resolutions based on PF jets rather than resolutions from unclustered PF particles in the $\mathcal{S}_{\mathrm{PF}}$ calculation (Eq. (9)) occurs at a jet p_T of 3 GeV. The $\mathcal{S}_{\mathrm{PF}}$ distributions are insensitive to the variation of this transition point between jets and individual particles over the range of 1 to approximately 6 GeV. By 10 GeV, a slope in the $\mathcal{P}(\chi^2)$ distribution has clearly appeared, indicating that we no longer account sufficiently for contributions to the $\not{E}_{\mathrm{T}}$ resolution from fluctuations in the reconstructed particle content.

A powerful feature of the $\not{E}_{\mathrm{T}}$ significance is that its distribution is insensitive to pile-up (for events with no genuine $\not{E}_{\mathrm{T}}$). As long as the correct resolutions are input, the significance should still have a pure exponential behaviour with a uniformly distributed $\mathcal{P}(\chi^2)$. In Fig. 21, no restrictions were made on the number of interaction vertices in the data, while the simulation has no pile-up. In Fig. 22, we compare the shapes of the single-vertex and multiple-vertex significance and $\mathcal{P}(\chi^2)$ distributions in data. The shapes are very similar, as expected. The main difference arises in the low probability region, where the multiple interaction data exhibits

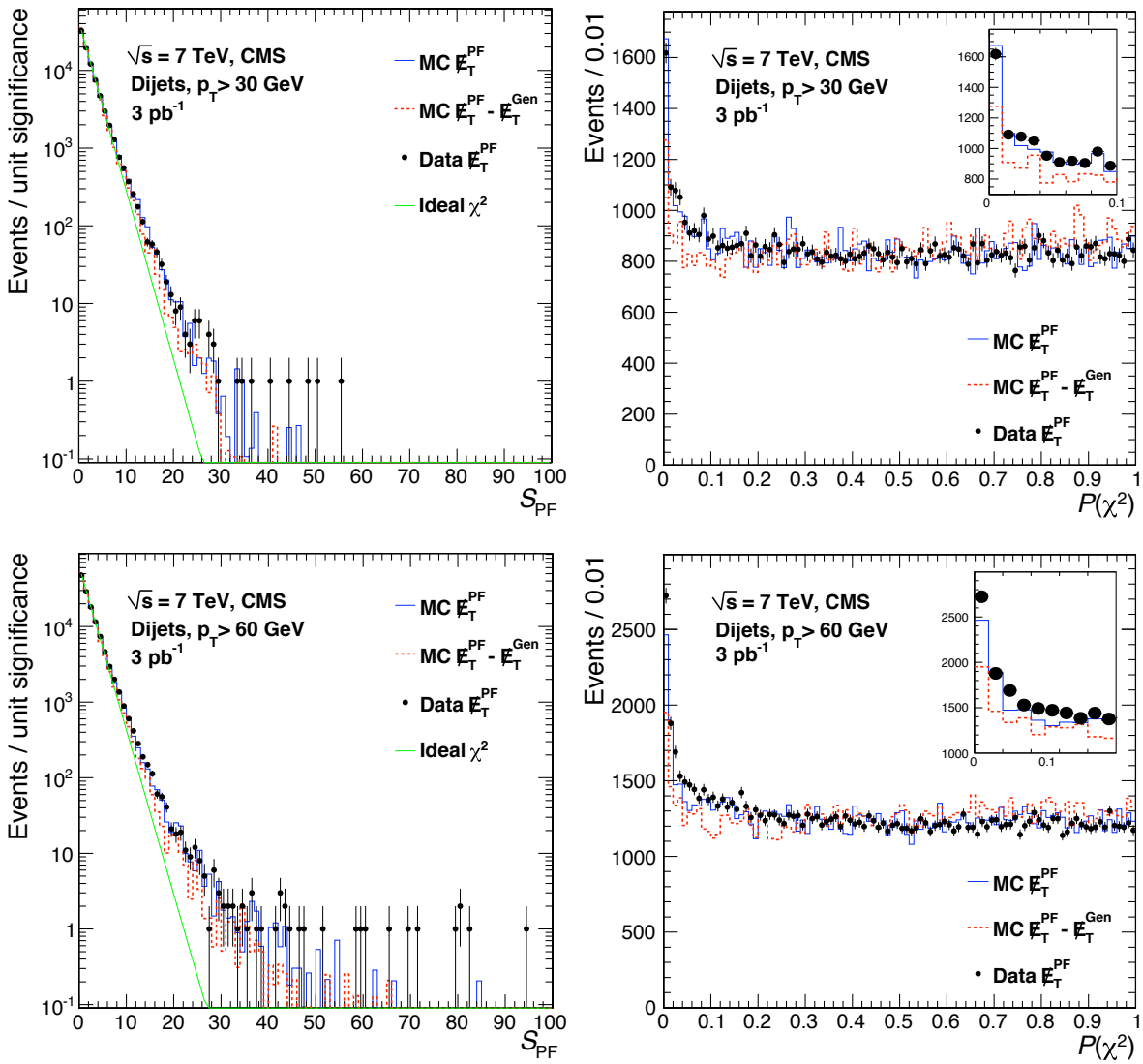

Figure 21: The $\not{E}_T$ significance $\mathcal{S}_{PF}$ distributions (left) and the corresponding probability of χ^2, $\mathcal{P}(\chi^2)$, distributions (right) for dijet event samples in data (points) and simulation (solid histograms) with 30 GeV (top) and 60 GeV (bottom) jet p_T thresholds. The dashed histograms show the simulation distributions with true $\not{E}_T$ contributions, from physics and finite acceptance effects, subtracted event-by-event. The dotted line overlaid on the $\mathcal{S}_{PF}$ distributions shows a reference pure exponential function. Each inset expands the small $\mathcal{P}(\chi^2)$ region.

behaviour closer to the ideal – an example of the central limit theorem. With the additional contributions to the $\not{E}_T$ resolution, the roles of the non-Gaussian response tails and genuine $\not{E}_T$ are diminished. The overall insensitivity can be useful, for example, when extrapolating backgrounds dominated by samples with nominally zero genuine $\not{E}_T$.

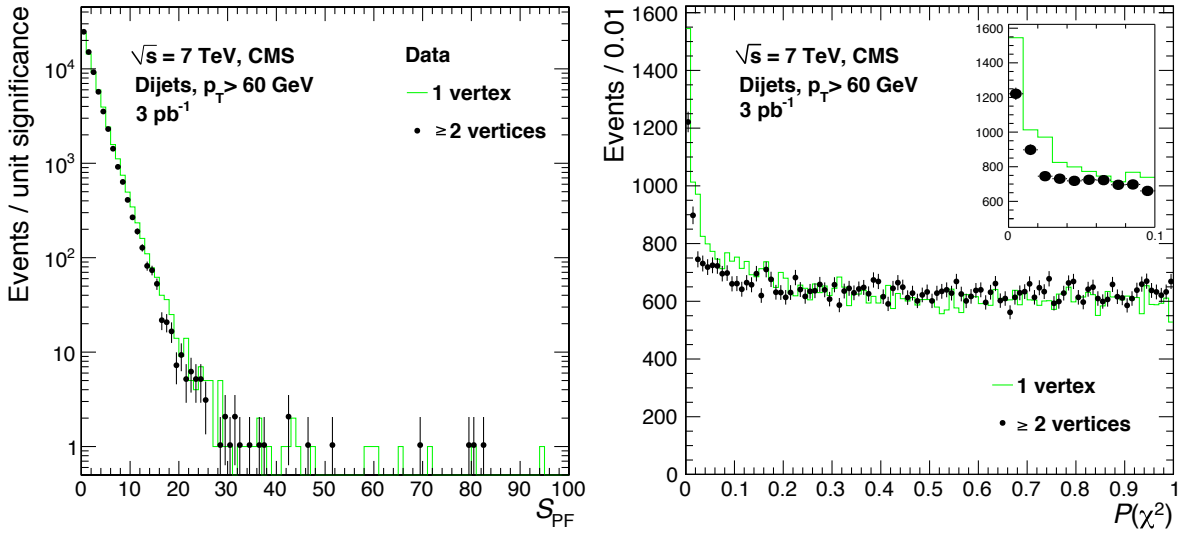

Figure 22: The $\not{E}_T$ significance (left) and $\mathcal{P}(\chi^2)$ (right) distributions for events with a single interaction vertex (histogram) and multiple interaction vertices (points) in the 60 GeV threshold dijet sample. The inset expands the small $\mathcal{P}(\chi^2)$ region.

8.3 Application to W → eν events

As a case study, we examine the potential gain of introducing the significance variable into the selection criteria for W → eν analyses. The set of criteria employed is that of the recent measurement by the CMS collaboration of the W cross section [25], for which backgrounds were controlled using a stringent, 80% efficient, electron isolation criterion. Signal and background yields in that analysis were determined by a fit to the reconstructed $\not{E}_T$ distribution, though because of the large backgrounds at small values of $\not{E}_T$, the signal level is largely determined from the $\not{E}_T > 20$ GeV region.

One analysis option would be to relax the electron isolation from an 80% to a 95% efficient criterion and introduce $\not{E}_T$ significance to help control backgrounds. Figure 23 compares the efficiency for signal versus background in simulation for increasing minimum thresholds on: $\not{E}_T$, with both the 80% and 95% electron isolation criteria applied; $\mathcal{S}_{PF}$, again with both isolation criteria; or $\not{E}_T/\sqrt{\sum E_{T_i}}$ with the 95% isolation criteria. All efficiencies are measured relative to the signal or background yield obtained with the looser 95% electron isolation criterion applied. (As a result, the tighter 80% criterion has an asymptotic value of approximately 84%.) Application of the tighter criterion changes the relative signal and background distributions for $\not{E}_T$ and $\not{E}_T$ significance compared to the looser criterion. When a minimum $\not{E}_T$ threshold is applied, the tighter isolation criterion provides a better signal to background ratio at low background levels than the looser criterion. Application of a minimum $\mathcal{S}_{PF}$ threshold with the looser criterion, however, outperforms all the other combinations for background rejection at a given signal efficiency.

We note that in the calculation of the significance, the isolated signal electron candidate enters as an electron, and in particular with the resolution associated with an electron. This approach

was found to outperform the option where each event was treated as electron-free (as is the case for the dominant background).

Figure 23 also shows that the $\mathcal{S}_{PF}$ distributions for $W \to e\nu$ in data and simulation agree well. As expected, the backgrounds without genuine $\not{E}_T$ are compressed towards low values of $\mathcal{S}_{PF}$ while signal events having real $\not{E}_T$ extend to high values of $\mathcal{S}_{PF}$.

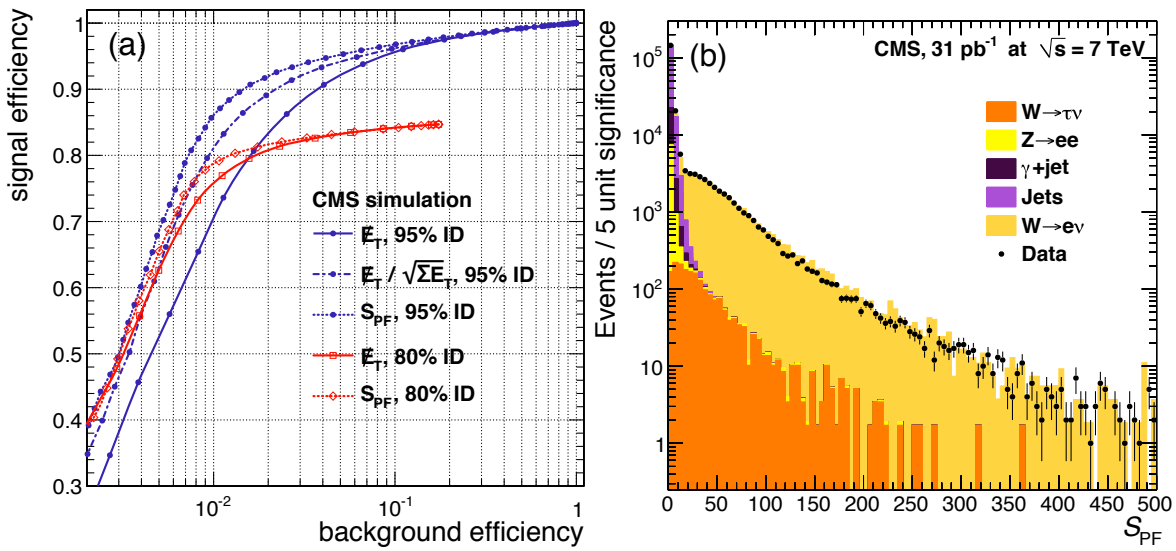

Figure 23: (left) Efficiency curves for $W \to e\nu$ signal versus backgrounds varying the minimum value of $\not{E}_T$ (solid lines), of $\mathcal{S}_{PF}$ (dotted lines), and of $\not{E}_T / \sqrt{\sum E_{T_i}}$ (dot-dash line), with the 95% efficient (blue) or 80% efficient (red) electron isolation criterion applied. (right) Distributions for $\mathcal{S}_{PF}$ in candidate $W \to e\nu$ events from data (points) and simulation (stacked histograms). The simulation components, from top to bottom, are signal (mustard) and backgrounds from jets (purple), $\gamma+$ jets (black), $Z \to e^+e^-$ (yellow), and $W^\pm \to \tau^\pm\nu_\tau$ (orange). The simulation is scaled by a fit to the data with floating normalizations for the signal and the total background.

Figures 24 and 25 contrast the behaviour of signal and total background efficiencies for minimum $\not{E}_T$ or $\mathcal{S}_{PF}$ thresholds for different numbers of interaction vertices (pile-up) in simulation. The jets and $\gamma+$ jets backgrounds, which have no genuine $\not{E}_T$, dominate. The background contribution at higher $\not{E}_T$ grows as pile-up increases, while the $\mathcal{S}_{PF}$ levels remain quite stable. As a result, a background subtraction based on extrapolation of $\not{E}_T$ will be sensitive to the modeling of pile-up, while one based on extrapolation of $\mathcal{S}_{PF}$ would not. As one can see from the signal versus background efficiency curves shown in Fig. 25, differentiation of signal from background degrades for both $\not{E}_T$ and $\mathcal{S}_{PF}$ as pile-up increases. Regardless of the amount of pile-up, however, $\mathcal{S}_{PF}$ always provides a superior signal to background ratio compared to $\not{E}_T$.

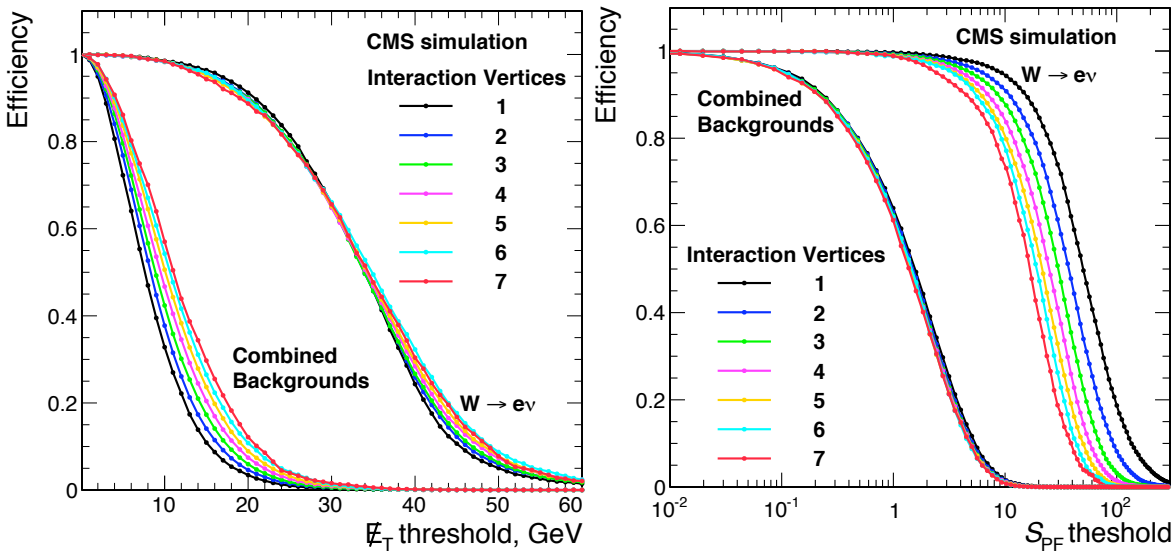

Figure 24: Efficiency versus minimum threshold curves for W → eν signal and for total background for different numbers of interaction vertices with a minimum applied $\not{E}_T$ threshold (left) and a minimum applied $\mathcal{S}_{PF}$ threshold (right).

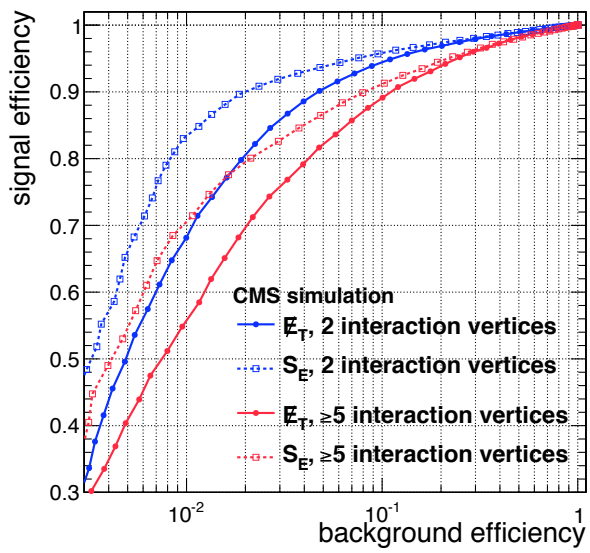

Figure 25: Efficiency curves for W → eν signal versus backgrounds varying the minimum value of $\not{E}_T$ (solid lines) and of $\mathcal{S}_{PF}$ (dotted lines) for events with two interaction vertices (blue) or at least five interaction vertices (red).

9 Conclusions

In conclusion, we studied $\vec{\not{E}}_{\mathrm{T}}$ as measured by the CMS detector with pp collisions at $\sqrt{s} = 7$ TeV during the 2010 run of the LHC. We have determined the $\vec{\not{E}}_{\mathrm{T}}$ scale, resolution, tails, and the degradation of the $\vec{\not{E}}_{\mathrm{T}}$ performance due to pile-up. We find that we are able to remove most sources of anomalous energies that produce artificial, large $\not{E}_{\mathrm{T}}$. The measured $\not{E}_{\mathrm{T}}$ scale agrees with the expectations of the detector simulation, but the resolution is degraded by 10% in data. CMS has three different algorithms for calculating $\not{E}_{\mathrm{T}}$. Algorithms using tracker information have an improved resolution, and the use of a global particle-flow event reconstruction gives the best resolution. We find that pile-up interactions contribute to the degradation of the $\not{E}_{\mathrm{T}}$ resolution but have little effect on the scale of a component of $\not{E}_{\mathrm{T}}$. We also find that we can model its effects with a simple parameterization.

One of the most important uses of $\not{E}_{\mathrm{T}}$ is to distinguish between genuine $\not{E}_{\mathrm{T}}$ produced by weakly interacting particles and artificial $\not{E}_{\mathrm{T}}$ from detector resolutions. An algorithm, called $\not{E}_{\mathrm{T}}$ significance, for separating genuine $\not{E}_{\mathrm{T}}$ from artificial $\not{E}_{\mathrm{T}}$, is shown to perform better than traditional variables such as $\not{E}_{\mathrm{T}}$ alone or $\not{E}_{\mathrm{T}}$ divided by the square root of the $\sum E_{\mathrm{T}}$.

Because of the demonstrated good measurement of $\vec{\not{E}}_{\mathrm{T}}$, the CMS detector is ready to be used for a variety of precision physics measurements, such as studies of the W boson, the top quark, and searches for new neutral, weakly interacting particles.

Acknowledgements

We wish to congratulate our colleagues in the CERN accelerator departments for the excellent performance of the LHC machine. We thank the technical and administrative staff at CERN and other CMS institutes. This work was supported by the Austrian Federal Ministry of Science and Research; the Belgium Fonds de la Recherche Scientifique, and Fonds voor Wetenschappelijk Onderzoek; the Brazilian Funding Agencies (CNPq, CAPES, FAPERJ, and FAPESP); the Bulgarian Ministry of Education and Science; CERN; the Chinese Academy of Sciences, Ministry of Science and Technology, and National Natural Science Foundation of China; the Colombian Funding Agency (COLCIENCIAS); the Croatian Ministry of Science, Education and Sport; the Research Promotion Foundation, Cyprus; the Estonian Academy of Sciences and NICPB; the Academy of Finland, Finnish Ministry of Education, and Helsinki Institute of Physics; the Institut National de Physique Nucléaire et de Physique des Particules / CNRS, and Commissariat à l'Énergie Atomique et aux Énergies Alternatives / CEA, France; the Bundesministerium für Bildung und Forschung, Deutsche Forschungsgemeinschaft, and Helmholtz-Gemeinschaft Deutscher Forschungszentren, Germany; the General Secretariat for Research and Technology, Greece; the National Scientific Research Foundation, and National Office for Research and Technology, Hungary; the Department of Atomic Energy, and Department of Science and Technology, India; the Institute for Studies in Theoretical Physics and Mathematics, Iran; the Science Foundation, Ireland; the Istituto Nazionale di Fisica Nucleare, Italy; the Korean Ministry of Education, Science and Technology and the World Class University program of NRF, Korea; the Lithuanian Academy of Sciences; the Mexican Funding Agencies (CINVESTAV, CONACYT, SEP, and UASLP-FAI); the Pakistan Atomic Energy Commission; the State Commission for Scientific Research, Poland; the Fundação para a Ciência e a Tecnologia, Portugal; JINR (Armenia, Belarus, Georgia, Ukraine, Uzbekistan); the Ministry of Science and Technologies of the Russian Federation, and Russian Ministry of Atomic Energy; the Ministry of Science and Technological Development of Serbia; the Ministerio de Ciencia e Innovación, and Programa Consolider-Ingenio 2010, Spain; the Swiss Funding Agencies (ETH Board, ETH Zurich, PSI,

SNF, UniZH, Canton Zurich, and SER); the National Science Council, Taipei; the Scientific and Technical Research Council of Turkey, and Turkish Atomic Energy Authority; the Science and Technology Facilities Council, UK; the US Department of Energy, and the US National Science Foundation.

Individuals have received support from the Marie-Curie programme and the European Research Council (European Union); the Leventis Foundation; the A. P. Sloan Foundation; the Alexander von Humboldt Foundation; the Associazione per lo Sviluppo Scientifico e Tecnologico del Piemonte (Italy); the Belgian Federal Science Policy Office; the Fonds pour la Formation à la Recherche dans l'Industrie et dans l'Agriculture (FRIA-Belgium); and the Agentschap voor Innovatie door Wetenschap en Technologie (IWT-Belgium).

References

[1] CMS Collaboration, "The CMS experiment at the CERN LHC", *JINST* **3** (2008) S08004. doi:10.1088/1748-0221/3/08/S08004.

[2] CMS Collaboration, "Jet Performance in pp Collisions at $\sqrt{s}$=7 TeV", *CMS Physics Analysis Summary* **CMS-PAS-JME-10-003** (2010).

[3] M. Cacciari, G. Salam, and G. Soyez, "The anti-k_t jet clustering algorithm", *JHEP* **08** (2008) 063, arXiv:arXiv:0802.1189. doi:10.1088/1126-6708/2008/04/063.

[4] CMS Collaboration, "Particle–Flow Event Reconstruction in CMS and Performance for Jets, Taus, and $\not{E}_{\mathrm{T}}$", *CMS Physics Analysis Summary* **CMS-PAS-PFT-09-001** (2009).

[5] CMS Collaboration, "Photon reconstruction and identification at $\sqrt{s}$ = 7 TeV", *CMS Physics Analysis Summary* **CMS-PAS-EGM-10-005** (2010).

[6] CMS Collaboration, "Missing Transverse Energy Performance in Minimum-Bias and Jet Events from Proton-Proton Collisions at $\sqrt{s}$ =7 TeV", *CMS Physics Analysis Summary* **CMS-PAS-JME-10-004** (2010).

[7] CMS Collaboration, "Algorithms for b Jet Identification in CMS", *CMS Physics Analysis Summary* **CMS-PAS-BTV-09-001** (2009).

[8] CMS Collaboration, "Commissioning of b-jet identification with pp collisions at $\sqrt{s}$ = 7 TeV", *CMS Physics Analysis Summary* **CMS-PAS-BTV-10-001** (2010).

[9] T. Sjöstrand, S. Mrenna, and P. Skands, "PYTHIA 6.4 Physics and Manual; v6.420, tune D6T", *JHEP* **05** (2006) 026, arXiv:hep-ph/0603175. doi:10.1088/1126-6708/2006/05/026.

[10] J. Alwall *et al.*, "MadGraph/MadEvent v4: The New Web Generation", *JHEP* **09** (2007) 028, arXiv:0706.2334. doi:10.1088/1126-6708/2007/09/028.

[11] Geant4 Collaboration, "Geant4: A simulation toolkit", *Nucl. Instrum. and Methods A* **506** (2003) 250. doi:10.1016/S0168-9002(03)01368-8.

[12] CMS Collaboration, "Performance of Jet Algorithms in CMS", *CMS Physics Analysis Summary* **CMS-PAS-JME-07-003** (2007).

[13] CMS Collaboration, "Performance of Track-Corrected Missing E_{T} in CMS", *CMS Physics Analysis Summary* **CMS-PAS-JME-09-010** (2009).

[14] CMS Collaboration, "Jet Energy Resolution in CMS at $\sqrt{s} = 7$ TeV", *CMS Physics Analysis Summary* **CMS-PAS-JME-10-014** (2010).

[15] CMS Collaboration, "Identification and Filtering of Uncharacteristic Noise in the CMS Hadron Calorimeter", *JINST* **5** (2009). doi:10.1088/1748-0221/5/03/T03014.

[16] CMS Collaboration, "HCAL performance from first collisions data", (2011). CMS Detector Performance Summary, to be released.

[17] CMS Collaboration, "Isolated Photon Reconstruction and Identification at $\sqrt{s} = 7$ TeV", *CMS Physics Analysis Summary* **CMS-PAS-EGM-10-006** (2010).

[18] CMS Collaboration, "Search for supersymmetry in pp collisions at 7 TeV in events with jets and missing transverse energy", *Physics Letters B* **698** (2011) 196. doi:DOI: 10.1016/j.physletb.2011.03.021.

[19] CMS Collaboration, "Performance of muon identification in pp collisions at $\sqrt{s}$ = 7 TeV", *CMS Physics Analysis Summary* **CMS-PAS-MUO-10-002** (2010).

[20] CMS Collaboration, "Jet Energy Calibration and Transverse Momentum Resolution in CMS", (2010). JME-10-011, to be published.

[21] C. Balazs and C. Yuan, "Soft gluon effects on lepton pairs at hadron colliders", *Phys. Rev.* **D56** (1997) 5558, arXiv:hep-ph/9704258. doi:10.1103/PhysRevD.56.5558.

[22] T. Sjöstrand, S. Mrenna, and P. Z. Skands, "A Brief Introduction to PYTHIA 8.1", *Comput. Phys. Commun.* **178** (2008) 852, arXiv:0710.3820. doi:10.1016/j.cpc.2008.01.036.

[23] R. Gavin et al., "FEWZ 2.0: A code for hadronic Z production at next-to- next-to-leading order", (2010). arXiv:1011.3540.

[24] CDF Collaboration, "Search for Anomalous Production of Events with Two Photons and Additional Energetic Objects at CDF", *Phys. Rev. D* **82** (2010) 052005, arXiv:0910.5170. doi:10.1103/PhysRevD.82.052005.

[25] CMS Collaboration, "Measurements of Inclusive W and Z Cross Sections in pp Collisions at $\sqrt{s} = 7$ TeV", *JHEP* **01** (2011) 80. doi:10.1007/JHEP01(2011)080.

A Appendix: Optimization of $\not{E}_T$ Corrections

In this section, we describe the optimization of the parameters used in the type-I and type-II corrections to $\vec{\not{E}}_T$.

For type-I $\vec{\not{E}}_T$, the p_T threshold used to select the jets that receive the correction was optimized by examining its effect on the $\vec{\not{E}}_T$ resolution and scale, and led to our choice of 10 GeV for PF $\not{E}_T$. We have optimized the p_T threshold to obtain the best $\not{E}_T$ scale and the best $\not{E}_T$ resolution at the same time, under the constraint that very low-p_T jets should not be included in the calculation because their energy corrections have large uncertainties and can degrade the $\not{E}_T$ performances. The use of low p_T jets also makes the measurement more sensitive to the pile-up.

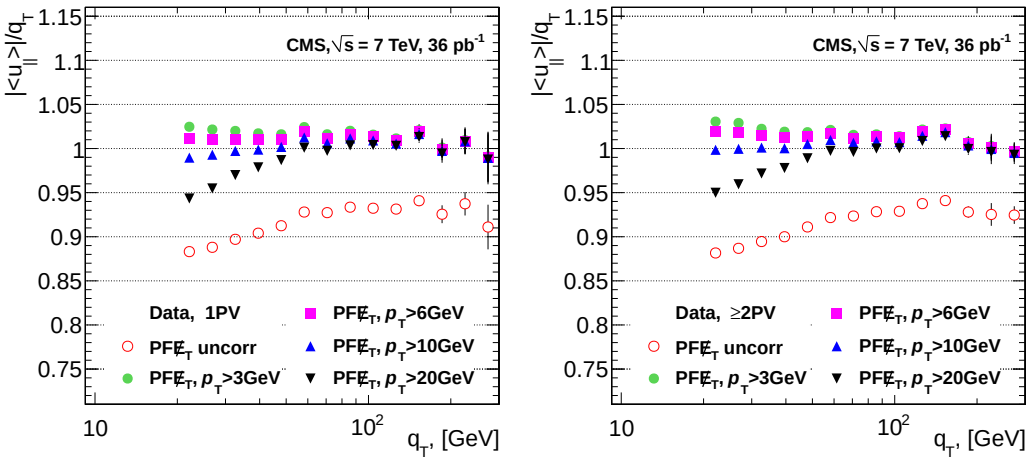

Figure 26: Response for PF $\not{E}_T$ versus γ q_T for various jet corrections thresholds for γ candidate events with 1 primary vertex (left) and more than 1 vertex (right).

Figure 26 shows the PF $\not{E}_T$ response versus q_T for γ candidate events for various jet thresholds for events with and without pile-up. As can be seen from these distributions, the type-I corrections substantially improve the $\not{E}_T$ scale, the dependence on the threshold is small for thresholds $\leq$ 10 GeV, and is independent of the number of additional pile-up interactions.

Figure 27 shows the ratio of the PF $\not{E}_T$ resolution with type-I corrections to the PF $\not{E}_T$ resolution without any type-I corrections for the parallel and perpendicular components of PF $\not{E}_T$ versus q_T for γ candidate events for various jet thresholds and for events with and without pile-up. The optimal resolution for 1 vertex events is obtained for the chosen 10 GeV threshold, and for this threshold, the degradation with pile-up is not large.

The same study has been performed in $Z \to \mu^+\mu^-$ candidate events. The 10 GeV threshold is also the best threshold to combine the improvement of the $\not{E}_T$ scale and $\not{E}_T$ resolution in these events.

Type-II corrections were not used for analyses done using the 2010 data. However, studies were done to optimize the parameters for future use. The type-II correction is obtained using a $Z \to ee$ data sample. Z events constitute an ideal sample for determining the type-II correction, as Z's are generally produced with low q_T and the recoil is often dominated by unclustered energy. We take the vector sum of momenta defined for all calorimeter towers or PF particles not corrected by the type-I correction as a single object denoted $\vec{U}$. The measured value of $\vec{U}$ is defined as:

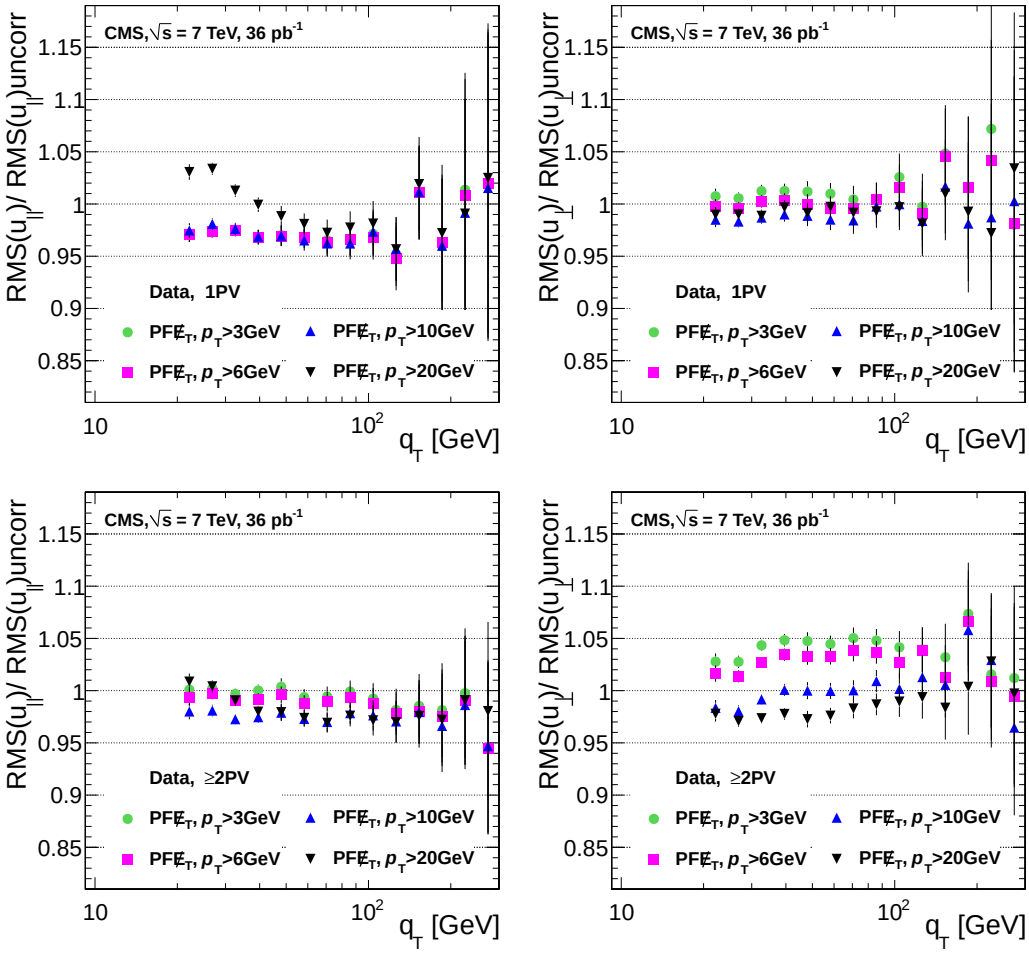

Figure 27: Ratio of PF $\not{E}_T$ resolution with type-I corrections to the the PF $\not{E}_T$ resolution without any type-I corrections for parallel (left) and perpendicular (right) components of PF $\not{E}_T$ versus γ q_T for various jet corrections thresholds for γ candidate events with 1 primary vertex (top) and more than 1 vertex (bottom) after correction for scale, using scale corrections similar to those shown in Fig. 10.

$$\vec{U}_{\mathrm{T,meas}} = -\vec{\not{E}}_{\mathrm{T\,uncorr}} - \sum \vec{p}_{\mathrm{T,jet,uncorr}} - \sum \vec{p}_{\mathrm{T,ele,meas}}, \tag{10}$$

where $\vec{\not{E}}_{\mathrm{T\,uncorr}}$ is the uncorrected $\not{E}_T$, $\vec{p}_{\mathrm{T,jets,uncorr}}$ is the momentum of uncorrected jets, and $\vec{p}_{\mathrm{T,ele,meas}}$ is the momentum of the measured electrons. The sum is over all jets with the corrected $p_T > 20$ GeV for Calo $\not{E}_T$ and $p_T > 10$ GeV for PF $\not{E}_T$.

The type-II correction for the unclustered energy $\vec{U}_{\mathrm{meas}}$ is obtained by selecting events without any reconstructed jets using the correlation between $\vec{U}_{\mathrm{meas}}$ and the q_T of the Z measured from the electrons.

As the direction of the $\vec{U}_{\mathrm{meas}}$ may differ from the direction of q_T due to noise, underlying event, etc., the parallel component of $\vec{U}_{\mathrm{meas}}$ projected on the direction of q_T, $\vec{U}_{\mathrm{meas},||}$, is used for the derivation of the correction. The response of the unclustered energy is then defined as $R(U_{\mathrm{T,meas}}) = U_{\mathrm{T,meas},||}/q_T$. The obtained correction factor, U_{scale}, is parametrized as $2.3 + 1.9\,\exp(-0.2 \cdot U_{\mathrm{T,meas}})$ for Calo $\not{E}_T$. For PF $\not{E}_T$ the obtained correction leads to a U_{scale} of 1.4.

These values obtained from data correspond well to the MC expectation.

One of the ways to validate the type-II corrected $\not{E}_T$ is to look at $\vec{\not{E}}_T$ decomposed into two components in dijet events. The decomposition is based on the dijet bisector axis, which divides the azimuthal opening angle between the leading two jets in two as illustrated in Fig. 28. Positive $\not{E}_{T||}$ points towards the smaller opening angle of the leading two jets, and positive $\not{E}_{T\perp}$ points towards the more central jet (smaller $|\eta|$). The distribution of $\not{E}_{T\perp}$ is symmetric for all

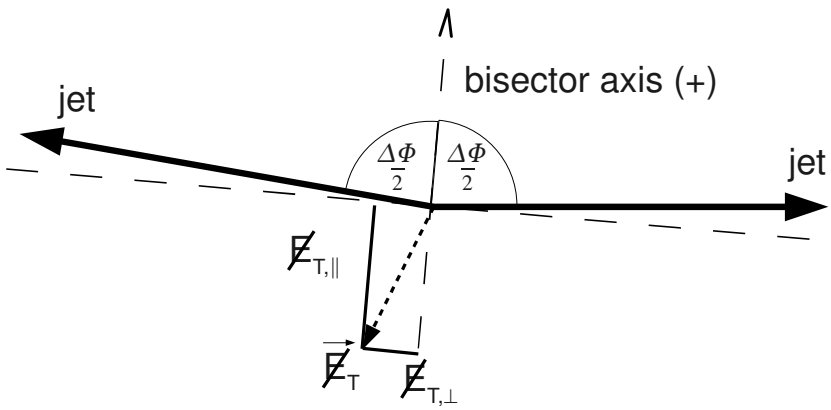

Figure 28: Kinematic definitions for dijet events.

correction levels, while by definition there is a slight asymmetry in $\not{E}_{T||}$. This is due to the fact that the bisector axis always points towards the opening angle of the leading two jets, while the $\not{E}_T$ tends to point in the opposite direction. The type-I correction introduces a more significant asymmetry in the $\not{E}_{T||}$ distribution, because it produces artificial $\not{E}_T$ in the direction opposite to the dijet opening angle. The type-II correction, however, calibrates the rest of the calorimeter energies, and makes the $\not{E}_{T||}$ distribution nearly symmetric again. This trend may be seen in Fig. 29 which shows the mean values of $\not{E}_{T||}$ as a function of $p_T^{avg} = (p_T^{jet1} + p_T^{jet2})/2$ for uncorrected, type-I corrected, and type-II corrected Calo- and PF $\not{E}_T$ in events containing at least two jets with $p_T > 40$ GeV and $|\eta| < 3$.

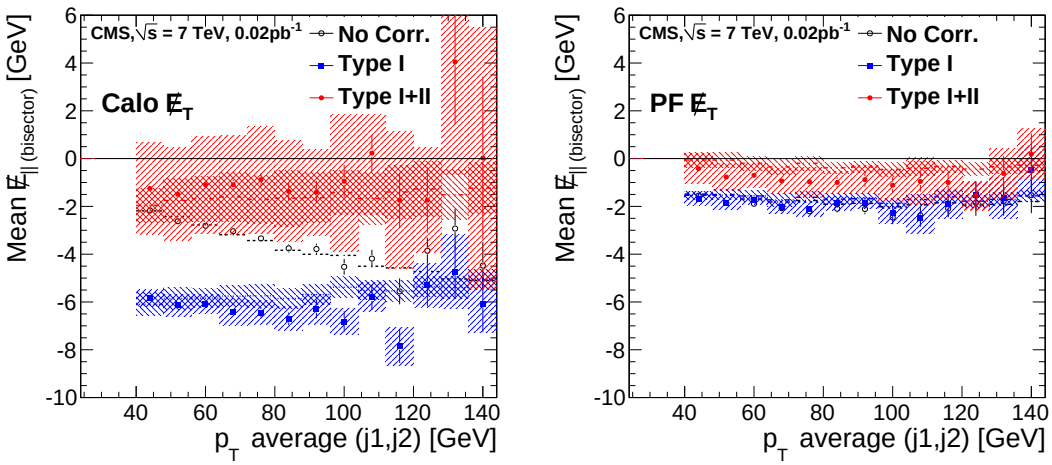

Figure 29: Mean values of $\not{E}_{T||}$ as a function of average p_T of the leading two jets (p_T^{avg}) in dijet events compared with Monte Carlo simulation (dashed lines) for uncorrected, type-I corrected, and type-II corrected (left) Calo $\not{E}_T$ and (right) PF $\not{E}_T$. The blue band on the distribution with type-I corrections represents the uncertainty due to uncertainties on the jet energy scale. The red band on the distribution with type-II corrections represents uncertainties due to uncertainties on the jet energy scale and statistical uncertainties due to the size of the $Z \to e^+e^-$ sample from which the correction for unclustered energies was derived.

B The CMS Collaboration

Yerevan Physics Institute, Yerevan, Armenia
S. Chatrchyan, V. Khachatryan, A.M. Sirunyan, A. Tumasyan

Institut für Hochenergiephysik der OeAW, Wien, Austria
W. Adam, T. Bergauer, M. Dragicevic, J. Erö, C. Fabjan, M. Friedl, R. Frühwirth, V.M. Ghete, J. Hammer[1], S. Hänsel, M. Hoch, N. Hörmann, J. Hrubec, M. Jeitler, W. Kiesenhofer, M. Krammer, D. Liko, I. Mikulec, M. Pernicka, H. Rohringer, R. Schöfbeck, J. Strauss, A. Taurok, F. Teischinger, P. Wagner, W. Waltenberger, G. Walzel, E. Widl, C.-E. Wulz

National Centre for Particle and High Energy Physics, Minsk, Belarus
V. Mossolov, N. Shumeiko, J. Suarez Gonzalez

Universiteit Antwerpen, Antwerpen, Belgium
L. Benucci, E.A. De Wolf, X. Janssen, J. Maes, T. Maes, L. Mucibello, S. Ochesanu, B. Roland, R. Rougny, M. Selvaggi, H. Van Haevermaet, P. Van Mechelen, N. Van Remortel

Vrije Universiteit Brussel, Brussel, Belgium
F. Blekman, S. Blyweert, J. D'Hondt, O. Devroede, R. Gonzalez Suarez, A. Kalogeropoulos, M. Maes, W. Van Doninck, P. Van Mulders, G.P. Van Onsem, I. Villella

Université Libre de Bruxelles, Bruxelles, Belgium
O. Charaf, B. Clerbaux, G. De Lentdecker, V. Dero, A.P.R. Gay, G.H. Hammad, T. Hreus, P.E. Marage, L. Thomas, C. Vander Velde, P. Vanlaer

Ghent University, Ghent, Belgium
V. Adler, A. Cimmino, S. Costantini, M. Grunewald, B. Klein, J. Lellouch, A. Marinov, J. Mccartin, D. Ryckbosch, F. Thyssen, M. Tytgat, L. Vanelderen, P. Verwilligen, S. Walsh, N. Zaganidis

Université Catholique de Louvain, Louvain-la-Neuve, Belgium
S. Basegmez, G. Bruno, J. Caudron, L. Ceard, E. Cortina Gil, J. De Favereau De Jeneret, C. Delaere[1], D. Favart, A. Giammanco, G. Grégoire, J. Hollar, V. Lemaitre, J. Liao, O. Militaru, S. Ovyn, D. Pagano, A. Pin, K. Piotrzkowski, N. Schul

Université de Mons, Mons, Belgium
N. Beliy, T. Caebergs, E. Daubie

Centro Brasileiro de Pesquisas Fisicas, Rio de Janeiro, Brazil
G.A. Alves, D. De Jesus Damiao, M.E. Pol, M.H.G. Souza

Universidade do Estado do Rio de Janeiro, Rio de Janeiro, Brazil
W. Carvalho, E.M. Da Costa, C. De Oliveira Martins, S. Fonseca De Souza, L. Mundim, H. Nogima, V. Oguri, W.L. Prado Da Silva, A. Santoro, S.M. Silva Do Amaral, A. Sznajder

Instituto de Fisica Teorica, Universidade Estadual Paulista, Sao Paulo, Brazil
C.A. Bernardes[2], F.A. Dias, T.R. Fernandez Perez Tomei, E. M. Gregores[2], C. Lagana, F. Marinho, P.G. Mercadante[2], S.F. Novaes, Sandra S. Padula

Institute for Nuclear Research and Nuclear Energy, Sofia, Bulgaria
N. Darmenov[1], L. Dimitrov, V. Genchev[1], P. Iaydjiev[1], S. Piperov, M. Rodozov, S. Stoykova, G. Sultanov, V. Tcholakov, R. Trayanov, I. Vankov

University of Sofia, Sofia, Bulgaria
A. Dimitrov, R. Hadjiiska, A. Karadzhinova, V. Kozhuharov, L. Litov, M. Mateev, B. Pavlov, P. Petkov

Institute of High Energy Physics, Beijing, China
J.G. Bian, G.M. Chen, H.S. Chen, C.H. Jiang, D. Liang, S. Liang, X. Meng, J. Tao, J. Wang, J. Wang, X. Wang, Z. Wang, H. Xiao, M. Xu, J. Zang, Z. Zhang

State Key Lab. of Nucl. Phys. and Tech., Peking University, Beijing, China
Y. Ban, S. Guo, Y. Guo, W. Li, Y. Mao, S.J. Qian, H. Teng, L. Zhang, B. Zhu, W. Zou

Universidad de Los Andes, Bogota, Colombia
A. Cabrera, B. Gomez Moreno, A.A. Ocampo Rios, A.F. Osorio Oliveros, J.C. Sanabria

Technical University of Split, Split, Croatia
N. Godinovic, D. Lelas, K. Lelas, R. Plestina[3], D. Polic, I. Puljak

University of Split, Split, Croatia
Z. Antunovic, M. Dzelalija

Institute Rudjer Boskovic, Zagreb, Croatia
V. Brigljevic, S. Duric, K. Kadija, S. Morovic

University of Cyprus, Nicosia, Cyprus
A. Attikis, M. Galanti, J. Mousa, C. Nicolaou, F. Ptochos, P.A. Razis

Charles University, Prague, Czech Republic
M. Finger, M. Finger Jr.

Academy of Scientific Research and Technology of the Arab Republic of Egypt, Egyptian Network of High Energy Physics, Cairo, Egypt
S. Khalil[4], M.A. Mahmoud[5], A. Radi[6]

National Institute of Chemical Physics and Biophysics, Tallinn, Estonia
A. Hektor, M. Kadastik, M. Müntel, M. Raidal, L. Rebane

Department of Physics, University of Helsinki, Helsinki, Finland
V. Azzolini, P. Eerola, G. Fedi

Helsinki Institute of Physics, Helsinki, Finland
S. Czellar, J. Härkönen, A. Heikkinen, V. Karimäki, R. Kinnunen, M.J. Kortelainen, T. Lampén, K. Lassila-Perini, S. Lehti, T. Lindén, P. Luukka, T. Mäenpää, E. Tuominen, J. Tuominiemi, E. Tuovinen, D. Ungaro, L. Wendland

Lappeenranta University of Technology, Lappeenranta, Finland
K. Banzuzi, A. Korpela, T. Tuuva

Laboratoire d'Annecy-le-Vieux de Physique des Particules, IN2P3-CNRS, Annecy-le-Vieux, France
D. Sillou

DSM/IRFU, CEA/Saclay, Gif-sur-Yvette, France
M. Besancon, S. Choudhury, M. Dejardin, D. Denegri, B. Fabbro, J.L. Faure, F. Ferri, S. Ganjour, F.X. Gentit, A. Givernaud, P. Gras, G. Hamel de Monchenault, P. Jarry, E. Locci, J. Malcles, M. Marionneau, L. Millischer, J. Rander, A. Rosowsky, I. Shreyber, M. Titov, P. Verrecchia

Laboratoire Leprince-Ringuet, Ecole Polytechnique, IN2P3-CNRS, Palaiseau, France
S. Baffioni, F. Beaudette, L. Benhabib, L. Bianchini, M. Bluj[7], C. Broutin, P. Busson, C. Charlot, T. Dahms, L. Dobrzynski, S. Elgammal, R. Granier de Cassagnac, M. Haguenauer, P. Miné, C. Mironov, C. Ochando, P. Paganini, D. Sabes, R. Salerno, Y. Sirois, C. Thiebaux, B. Wyslouch[8], A. Zabi

Institut Pluridisciplinaire Hubert Curien, Université de Strasbourg, Université de Haute Alsace Mulhouse, CNRS/IN2P3, Strasbourg, France
J.-L. Agram[9], J. Andrea, D. Bloch, D. Bodin, J.-M. Brom, M. Cardaci, E.C. Chabert, C. Collard, E. Conte[9], F. Drouhin[9], C. Ferro, J.-C. Fontaine[9], D. Gelé, U. Goerlach, S. Greder, P. Juillot, M. Karim[9], A.-C. Le Bihan, Y. Mikami, P. Van Hove

Centre de Calcul de l'Institut National de Physique Nucleaire et de Physique des Particules (IN2P3), Villeurbanne, France
F. Fassi, D. Mercier

Université de Lyon, Université Claude Bernard Lyon 1, CNRS-IN2P3, Institut de Physique Nucléaire de Lyon, Villeurbanne, France
C. Baty, S. Beauceron, N. Beaupere, M. Bedjidian, O. Bondu, G. Boudoul, D. Boumediene, H. Brun, J. Chasserat, R. Chierici, D. Contardo, P. Depasse, H. El Mamouni, J. Fay, S. Gascon, B. Ille, T. Kurca, T. Le Grand, M. Lethuillier, L. Mirabito, S. Perries, V. Sordini, S. Tosi, Y. Tschudi, P. Verdier

Institute of High Energy Physics and Informatization, Tbilisi State University, Tbilisi, Georgia
D. Lomidze

RWTH Aachen University, I. Physikalisches Institut, Aachen, Germany
G. Anagnostou, M. Edelhoff, L. Feld, N. Heracleous, O. Hindrichs, R. Jussen, K. Klein, J. Merz, N. Mohr, A. Ostapchuk, A. Perieanu, F. Raupach, J. Sammet, S. Schael, D. Sprenger, H. Weber, M. Weber, B. Wittmer

RWTH Aachen University, III. Physikalisches Institut A, Aachen, Germany
M. Ata, W. Bender, E. Dietz-Laursonn, M. Erdmann, J. Frangenheim, T. Hebbeker, A. Hinzmann, K. Hoepfner, T. Klimkovich, D. Klingebiel, P. Kreuzer, D. Lanske[†], C. Magass, M. Merschmeyer, A. Meyer, P. Papacz, H. Pieta, H. Reithler, S.A. Schmitz, L. Sonnenschein, J. Steggemann, D. Teyssier

RWTH Aachen University, III. Physikalisches Institut B, Aachen, Germany
M. Bontenackels, M. Davids, M. Duda, G. Flügge, H. Geenen, M. Giffels, W. Haj Ahmad, D. Heydhausen, T. Kress, Y. Kuessel, A. Linn, A. Nowack, L. Perchalla, O. Pooth, J. Rennefeld, P. Sauerland, A. Stahl, M. Thomas, D. Tornier, M.H. Zoeller

Deutsches Elektronen-Synchrotron, Hamburg, Germany
M. Aldaya Martin, W. Behrenhoff, U. Behrens, M. Bergholz[10], A. Bethani, K. Borras, A. Cakir, A. Campbell, E. Castro, D. Dammann, G. Eckerlin, D. Eckstein, A. Flossdorf, G. Flucke, A. Geiser, J. Hauk, H. Jung[1], M. Kasemann, I. Katkov[11], P. Katsas, C. Kleinwort, H. Kluge, A. Knutsson, M. Krämer, D. Krücker, E. Kuznetsova, W. Lange, W. Lohmann[10], R. Mankel, M. Marienfeld, I.-A. Melzer-Pellmann, A.B. Meyer, J. Mnich, A. Mussgiller, J. Olzem, D. Pitzl, A. Raspereza, A. Raval, M. Rosin, R. Schmidt[10], T. Schoerner-Sadenius, N. Sen, A. Spiridonov, M. Stein, J. Tomaszewska, R. Walsh, C. Wissing

University of Hamburg, Hamburg, Germany
C. Autermann, V. Blobel, S. Bobrovskyi, J. Draeger, H. Enderle, U. Gebbert, K. Kaschube,

G. Kaussen, R. Klanner, J. Lange, B. Mura, S. Naumann-Emme, F. Nowak, N. Pietsch, C. Sander, H. Schettler, P. Schleper, M. Schröder, T. Schum, J. Schwandt, H. Stadie, G. Steinbrück, J. Thomsen

Institut für Experimentelle Kernphysik, Karlsruhe, Germany
C. Barth, J. Bauer, V. Buege, T. Chwalek, W. De Boer, A. Dierlamm, G. Dirkes, M. Feindt, J. Gruschke, C. Hackstein, F. Hartmann, M. Heinrich, H. Held, K.H. Hoffmann, S. Honc, J.R. Komaragiri, T. Kuhr, D. Martschei, S. Mueller, Th. Müller, M. Niegel, O. Oberst, A. Oehler, J. Ott, T. Peiffer, G. Quast, K. Rabbertz, F. Ratnikov, N. Ratnikova, M. Renz, C. Saout, A. Scheurer, P. Schieferdecker, F.-P. Schilling, M. Schmanau, G. Schott, H.J. Simonis, F.M. Stober, D. Troendle, J. Wagner-Kuhr, T. Weiler, M. Zeise, V. Zhukov[11], E.B. Ziebarth

Institute of Nuclear Physics "Demokritos", Aghia Paraskevi, Greece
G. Daskalakis, T. Geralis, S. Kesisoglou, A. Kyriakis, D. Loukas, I. Manolakos, A. Markou, C. Markou, C. Mavrommatis, E. Ntomari, E. Petrakou

University of Athens, Athens, Greece
L. Gouskos, T.J. Mertzimekis, A. Panagiotou, E. Stiliaris

University of Ioánnina, Ioánnina, Greece
I. Evangelou, C. Foudas, P. Kokkas, N. Manthos, I. Papadopoulos, V. Patras, F.A. Triantis

KFKI Research Institute for Particle and Nuclear Physics, Budapest, Hungary
A. Aranyi, G. Bencze, L. Boldizsar, C. Hajdu[1], P. Hidas, D. Horvath[12], A. Kapusi, K. Krajczar[13], F. Sikler[1], G.I. Veres[13], G. Vesztergombi[13]

Institute of Nuclear Research ATOMKI, Debrecen, Hungary
N. Beni, J. Molnar, J. Palinkas, Z. Szillasi, V. Veszpremi

University of Debrecen, Debrecen, Hungary
P. Raics, Z.L. Trocsanyi, B. Ujvari

Panjab University, Chandigarh, India
S. Bansal, S.B. Beri, V. Bhatnagar, N. Dhingra, R. Gupta, M. Jindal, M. Kaur, J.M. Kohli, M.Z. Mehta, N. Nishu, L.K. Saini, A. Sharma, A.P. Singh, J. Singh, S.P. Singh

University of Delhi, Delhi, India
S. Ahuja, S. Bhattacharya, B.C. Choudhary, B. Gomber, P. Gupta, S. Jain, S. Jain, R. Khurana, A. Kumar, K. Ranjan, R.K. Shivpuri

Bhabha Atomic Research Centre, Mumbai, India
R.K. Choudhury, D. Dutta, S. Kailas, V. Kumar, P. Mehta, A.K. Mohanty[1], L.M. Pant, P. Shukla

Tata Institute of Fundamental Research - EHEP, Mumbai, India
T. Aziz, M. Guchait[14], A. Gurtu, M. Maity[15], D. Majumder, G. Majumder, K. Mazumdar, G.B. Mohanty, A. Saha, K. Sudhakar, N. Wickramage

Tata Institute of Fundamental Research - HECR, Mumbai, India
S. Banerjee, S. Dugad, N.K. Mondal

Institute for Research and Fundamental Sciences (IPM), Tehran, Iran
H. Arfaei, H. Bakhshiansohi[16], S.M. Etesami, A. Fahim[16], M. Hashemi, A. Jafari[16], M. Khakzad, A. Mohammadi[17], M. Mohammadi Najafabadi, S. Paktinat Mehdiabadi, B. Safarzadeh, M. Zeinali[18]

INFN Sezione di Bari [a], Università di Bari [b], Politecnico di Bari [c], Bari, Italy
M. Abbrescia[a,b], L. Barbone[a,b], C. Calabria[a,b], A. Colaleo[a], D. Creanza[a,c], N. De Filippis[a,c,1], M. De Palma[a,b], L. Fiore[a], G. Iaselli[a,c], L. Lusito[a,b], G. Maggi[a,c], M. Maggi[a], N. Manna[a,b], B. Marangelli[a,b], S. My[a,c], S. Nuzzo[a,b], N. Pacifico[a,b], G.A. Pierro[a], A. Pompili[a,b], G. Pugliese[a,c], F. Romano[a,c], G. Roselli[a,b], G. Selvaggi[a,b], L. Silvestris[a], R. Trentadue[a], S. Tupputi[a,b], G. Zito[a]

INFN Sezione di Bologna [a], Università di Bologna [b], Bologna, Italy
G. Abbiendi[a], A.C. Benvenuti[a], D. Bonacorsi[a], S. Braibant-Giacomelli[a,b], L. Brigliadori[a], P. Capiluppi[a,b], A. Castro[a,b], F.R. Cavallo[a], M. Cuffiani[a,b], G.M. Dallavalle[a], F. Fabbri[a], A. Fanfani[a,b], D. Fasanella[a], P. Giacomelli[a], M. Giunta[a], C. Grandi[a], S. Marcellini[a], G. Masetti[b], M. Meneghelli[a,b], A. Montanari[a], F.L. Navarria[a,b], F. Odorici[a], A. Perrotta[a], F. Primavera[a], A.M. Rossi[a,b], T. Rovelli[a,b], G. Siroli[a,b], R. Travaglini[a,b]

INFN Sezione di Catania [a], Università di Catania [b], Catania, Italy
S. Albergo[a,b], G. Cappello[a,b], M. Chiorboli[a,b,1], S. Costa[a,b], A. Tricomi[a,b], C. Tuve[a]

INFN Sezione di Firenze [a], Università di Firenze [b], Firenze, Italy
G. Barbagli[a], V. Ciulli[a,b], C. Civinini[a], R. D'Alessandro[a,b], E. Focardi[a,b], S. Frosali[a,b], E. Gallo[a], S. Gonzi[a,b], P. Lenzi[a,b], M. Meschini[a], S. Paoletti[a], G. Sguazzoni[a], A. Tropiano[a,1]

INFN Laboratori Nazionali di Frascati, Frascati, Italy
L. Benussi, S. Bianco, S. Colafranceschi[19], F. Fabbri, D. Piccolo

INFN Sezione di Genova, Genova, Italy
P. Fabbricatore, R. Musenich

INFN Sezione di Milano-Bicocca [a], Università di Milano-Bicocca [b], Milano, Italy
A. Benaglia[a,b], F. De Guio[a,b,1], L. Di Matteo[a,b], S. Gennai[1], A. Ghezzi[a,b], S. Malvezzi[a], A. Martelli[a,b], A. Massironi[a,b], D. Menasce[a], L. Moroni[a], M. Paganoni[a,b], D. Pedrini[a], S. Ragazzi[a,b], N. Redaelli[a], S. Sala[a], T. Tabarelli de Fatis[a,b]

INFN Sezione di Napoli [a], Università di Napoli "Federico II" [b], Napoli, Italy
S. Buontempo[a], C.A. Carrillo Montoya[a,1], N. Cavallo[a,20], A. De Cosa[a,b], F. Fabozzi[a,20], A.O.M. Iorio[a,1], L. Lista[a], M. Merola[a,b], P. Paolucci[a]

INFN Sezione di Padova [a], Università di Padova [b], Università di Trento (Trento) [c], Padova, Italy
P. Azzi[a], N. Bacchetta[a], P. Bellan[a,b], D. Bisello[a,b], A. Branca[a], R. Carlin[a,b], P. Checchia[a], M. De Mattia[a,b], T. Dorigo[a], U. Dosselli[a], F. Fanzago[a], F. Gasparini[a,b], U. Gasparini[a,b], A. Gozzelino, S. Lacaprara[a,21], I. Lazzizzera[a,c], M. Margoni[a,b], M. Mazzucato[a], A.T. Meneguzzo[a,b], M. Nespolo[a,1], L. Perrozzi[a,1], N. Pozzobon[a,b], P. Ronchese[a,b], F. Simonetto[a,b], E. Torassa[a], M. Tosi[a,b], S. Vanini[a,b], P. Zotto[a,b], G. Zumerle[a,b]

INFN Sezione di Pavia [a], Università di Pavia [b], Pavia, Italy
P. Baesso[a,b], U. Berzano[a], S.P. Ratti[a,b], C. Riccardi[a,b], P. Torre[a,b], P. Vitulo[a,b], C. Viviani[a,b]

INFN Sezione di Perugia [a], Università di Perugia [b], Perugia, Italy
M. Biasini[a,b], G.M. Bilei[a], B. Caponeri[a,b], L. Fanò[a,b], P. Lariccia[a,b], A. Lucaroni[a,b,1], G. Mantovani[a,b], M. Menichelli[a], A. Nappi[a,b], F. Romeo[a,b], A. Santocchia[a,b], S. Taroni[a,b,1], M. Valdata[a,b]

INFN Sezione di Pisa [a], Università di Pisa [b], Scuola Normale Superiore di Pisa [c], Pisa, Italy
P. Azzurri[a,c], G. Bagliesi[a], J. Bernardini[a,b], T. Boccali[a,1], G. Broccolo[a,c], R. Castaldi[a], R.T. D'Agnolo[a,c], R. Dell'Orso[a], F. Fiori[a,b], L. Foà[a,c], A. Giassi[a], A. Kraan[a], F. Ligabue[a,c],

T. Lomtadze[a], L. Martini[a,22], A. Messineo[a,b], F. Palla[a], G. Segneri[a], A.T. Serban[a], P. Spagnolo[a], R. Tenchini[a], G. Tonelli[a,b,1], A. Venturi[a,1], P.G. Verdini[a]

INFN Sezione di Roma [a], Università di Roma "La Sapienza" [b], Roma, Italy
L. Barone[a,b], F. Cavallari[a], D. Del Re[a,b], E. Di Marco[a,b], M. Diemoz[a], D. Franci[a,b], M. Grassi[a,1], E. Longo[a,b], S. Nourbakhsh[a], G. Organtini[a,b], F. Pandolfi[a,b,1], R. Paramatti[a], S. Rahatlou[a,b], C. Rovelli[1]

INFN Sezione di Torino [a], Università di Torino [b], Università del Piemonte Orientale (Novara) [c], Torino, Italy
N. Amapane[a,b], R. Arcidiacono[a,c], S. Argiro[a,b], M. Arneodo[a,c], C. Biino[a], C. Botta[a,b,1], N. Cartiglia[a], R. Castello[a,b], M. Costa[a,b], N. Demaria[a], A. Graziano[a,b,1], C. Mariotti[a], M. Marone[a,b], S. Maselli[a], E. Migliore[a,b], G. Mila[a,b], V. Monaco[a,b], M. Musich[a,b], M.M. Obertino[a,c], N. Pastrone[a], M. Pelliccioni[a,b], A. Romero[a,b], M. Ruspa[a,c], R. Sacchi[a,b], V. Sola[a,b], A. Solano[a,b], A. Staiano[a], A. Vilela Pereira[a]

INFN Sezione di Trieste [a], Università di Trieste [b], Trieste, Italy
S. Belforte[a], F. Cossutti[a], G. Della Ricca[a,b], B. Gobbo[a], D. Montanino[a,b], A. Penzo[a]

Kangwon National University, Chunchon, Korea
S.G. Heo, S.K. Nam

Kyungpook National University, Daegu, Korea
S. Chang, J. Chung, D.H. Kim, G.N. Kim, J.E. Kim, D.J. Kong, H. Park, S.R. Ro, D. Son, D.C. Son, T. Son

Chonnam National University, Institute for Universe and Elementary Particles, Kwangju, Korea
Zero Kim, J.Y. Kim, S. Song

Korea University, Seoul, Korea
S. Choi, B. Hong, M.S. Jeong, M. Jo, H. Kim, J.H. Kim, T.J. Kim, K.S. Lee, D.H. Moon, S.K. Park, H.B. Rhee, E. Seo, S. Shin, K.S. Sim

University of Seoul, Seoul, Korea
M. Choi, S. Kang, H. Kim, C. Park, I.C. Park, S. Park, G. Ryu

Sungkyunkwan University, Suwon, Korea
Y. Choi, Y.K. Choi, J. Goh, M.S. Kim, E. Kwon, J. Lee, S. Lee, H. Seo, I. Yu

Vilnius University, Vilnius, Lithuania
M.J. Bilinskas, I. Grigelionis, M. Janulis, D. Martisiute, P. Petrov, T. Sabonis

Centro de Investigacion y de Estudios Avanzados del IPN, Mexico City, Mexico
H. Castilla-Valdez, E. De La Cruz-Burelo, I. Heredia-de La Cruz, R. Lopez-Fernandez, R. Magaña Villalba, A. Sánchez-Hernández, L.M. Villasenor-Cendejas

Universidad Iberoamericana, Mexico City, Mexico
S. Carrillo Moreno, F. Vazquez Valencia

Benemerita Universidad Autonoma de Puebla, Puebla, Mexico
H.A. Salazar Ibarguen

Universidad Autónoma de San Luis Potosí, San Luis Potosí, Mexico
E. Casimiro Linares, A. Morelos Pineda, M.A. Reyes-Santos

University of Auckland, Auckland, New Zealand
D. Krofcheck, J. Tam, C.H. Yiu

University of Canterbury, Christchurch, New Zealand
P.H. Butler, R. Doesburg, H. Silverwood

National Centre for Physics, Quaid-I-Azam University, Islamabad, Pakistan
M. Ahmad, I. Ahmed, M.I. Asghar, H.R. Hoorani, W.A. Khan, T. Khurshid, S. Qazi

Institute of Experimental Physics, Faculty of Physics, University of Warsaw, Warsaw, Poland
G. Brona, M. Cwiok, W. Dominik, K. Doroba, A. Kalinowski, M. Konecki, J. Krolikowski

Soltan Institute for Nuclear Studies, Warsaw, Poland
T. Frueboes, R. Gokieli, M. Górski, M. Kazana, K. Nawrocki, K. Romanowska-Rybinska, M. Szleper, G. Wrochna, P. Zalewski

Laboratório de Instrumentação e Física Experimental de Partículas, Lisboa, Portugal
N. Almeida, P. Bargassa, A. David, P. Faccioli, P.G. Ferreira Parracho, M. Gallinaro, P. Musella, A. Nayak, P.Q. Ribeiro, J. Seixas, J. Varela

Joint Institute for Nuclear Research, Dubna, Russia
I. Belotelov, P. Bunin, I. Golutvin, A. Kamenev, V. Karjavin, V. Konoplyanikov, G. Kozlov, A. Lanev, P. Moisenz, V. Palichik, V. Perelygin, S. Shmatov, V. Smirnov, A. Volodko, A. Zarubin

Petersburg Nuclear Physics Institute, Gatchina (St Petersburg), Russia
V. Golovtsov, Y. Ivanov, V. Kim, P. Levchenko, V. Murzin, V. Oreshkin, I. Smirnov, V. Sulimov, L. Uvarov, S. Vavilov, A. Vorobyev, An. Vorobyev

Institute for Nuclear Research, Moscow, Russia
Yu. Andreev, A. Dermenev, S. Gninenko, N. Golubev, M. Kirsanov, N. Krasnikov, V. Matveev, A. Pashenkov, A. Toropin, S. Troitsky

Institute for Theoretical and Experimental Physics, Moscow, Russia
V. Epshteyn, V. Gavrilov, V. Kaftanov[†], M. Kossov[1], A. Krokhotin, N. Lychkovskaya, V. Popov, G. Safronov, S. Semenov, V. Stolin, E. Vlasov, A. Zhokin

Moscow State University, Moscow, Russia
E. Boos, M. Dubinin[23], L. Dudko, A. Ershov, A. Gribushin, O. Kodolova, I. Lokhtin, A. Markina, S. Obraztsov, M. Perfilov, S. Petrushanko, L. Sarycheva, V. Savrin, A. Snigirev

P.N. Lebedev Physical Institute, Moscow, Russia
V. Andreev, M. Azarkin, I. Dremin, M. Kirakosyan, A. Leonidov, S.V. Rusakov, A. Vinogradov

State Research Center of Russian Federation, Institute for High Energy Physics, Protvino, Russia
I. Azhgirey, S. Bitioukov, V. Grishin[1], V. Kachanov, D. Konstantinov, A. Korablev, V. Krychkine, V. Petrov, R. Ryutin, S. Slabospitsky, A. Sobol, L. Tourtchanovitch, S. Troshin, N. Tyurin, A. Uzunian, A. Volkov

University of Belgrade, Faculty of Physics and Vinca Institute of Nuclear Sciences, Belgrade, Serbia
P. Adzic[24], M. Djordjevic, D. Krpic[24], J. Milosevic

Centro de Investigaciones Energéticas Medioambientales y Tecnológicas (CIEMAT), Madrid, Spain
M. Aguilar-Benitez, J. Alcaraz Maestre, P. Arce, C. Battilana, E. Calvo, M. Cepeda, M. Cerrada,

M. Chamizo Llatas, N. Colino, B. De La Cruz, A. Delgado Peris, C. Diez Pardos, D. Domínguez Vázquez, C. Fernandez Bedoya, J.P. Fernández Ramos, A. Ferrando, J. Flix, M.C. Fouz, P. Garcia-Abia, O. Gonzalez Lopez, S. Goy Lopez, J.M. Hernandez, M.I. Josa, G. Merino, J. Puerta Pelayo, I. Redondo, L. Romero, J. Santaolalla, M.S. Soares, C. Willmott

Universidad Autónoma de Madrid, Madrid, Spain
C. Albajar, G. Codispoti, J.F. de Trocóniz

Universidad de Oviedo, Oviedo, Spain
J. Cuevas, J. Fernandez Menendez, S. Folgueras, I. Gonzalez Caballero, L. Lloret Iglesias, J.M. Vizan Garcia

Instituto de Física de Cantabria (IFCA), CSIC-Universidad de Cantabria, Santander, Spain
J.A. Brochero Cifuentes, I.J. Cabrillo, A. Calderon, S.H. Chuang, J. Duarte Campderros, M. Felcini[25], M. Fernandez, G. Gomez, J. Gonzalez Sanchez, C. Jorda, P. Lobelle Pardo, A. Lopez Virto, J. Marco, R. Marco, C. Martinez Rivero, F. Matorras, F.J. Munoz Sanchez, J. Piedra Gomez[26], T. Rodrigo, A.Y. Rodríguez-Marrero, A. Ruiz-Jimeno, L. Scodellaro, M. Sobron Sanudo, I. Vila, R. Vilar Cortabitarte

CERN, European Organization for Nuclear Research, Geneva, Switzerland
D. Abbaneo, E. Auffray, G. Auzinger, P. Baillon, A.H. Ball, D. Barney, A.J. Bell[27], D. Benedetti, C. Bernet[3], W. Bialas, P. Bloch, A. Bocci, S. Bolognesi, M. Bona, H. Breuker, K. Bunkowski, T. Camporesi, G. Cerminara, T. Christiansen, J.A. Coarasa Perez, B. Curé, D. D'Enterria, A. De Roeck, S. Di Guida, N. Dupont-Sagorin, A. Elliott-Peisert, B. Frisch, W. Funk, A. Gaddi, G. Georgiou, H. Gerwig, D. Gigi, K. Gill, D. Giordano, F. Glege, R. Gomez-Reino Garrido, M. Gouzevitch, P. Govoni, S. Gowdy, L. Guiducci, M. Hansen, C. Hartl, J. Harvey, J. Hegeman, B. Hegner, H.F. Hoffmann, A. Honma, V. Innocente, P. Janot, K. Kaadze, E. Karavakis, P. Lecoq, C. Lourenço, T. Mäki, M. Malberti, L. Malgeri, M. Mannelli, L. Masetti, A. Maurisset, F. Meijers, S. Mersi, E. Meschi, R. Moser, M.U. Mozer, M. Mulders, E. Nesvold[1], M. Nguyen, T. Orimoto, L. Orsini, E. Perez, A. Petrilli, A. Pfeiffer, M. Pierini, M. Pimiä, D. Piparo, G. Polese, A. Racz, J. Rodrigues Antunes, G. Rolandi[28], T. Rommerskirchen, M. Rovere, H. Sakulin, C. Schäfer, C. Schwick, I. Segoni, A. Sharma, P. Siegrist, M. Simon, P. Sphicas[29], M. Spiropulu[23], M. Stoye, M. Tadel, P. Tropea, A. Tsirou, P. Vichoudis, M. Voutilainen, W.D. Zeuner

Paul Scherrer Institut, Villigen, Switzerland
W. Bertl, K. Deiters, W. Erdmann, K. Gabathuler, R. Horisberger, Q. Ingram, H.C. Kaestli, S. König, D. Kotlinski, U. Langenegger, F. Meier, D. Renker, T. Rohe, J. Sibille[30], A. Starodumov[31]

Institute for Particle Physics, ETH Zurich, Zurich, Switzerland
P. Bortignon, L. Caminada[32], N. Chanon, Z. Chen, S. Cittolin, G. Dissertori, M. Dittmar, J. Eugster, K. Freudenreich, C. Grab, A. Hervé, W. Hintz, P. Lecomte, W. Lustermann, C. Marchica[32], P. Martinez Ruiz del Arbol, P. Meridiani, P. Milenovic[33], F. Moortgat, C. Nägeli[32], P. Nef, F. Nessi-Tedaldi, L. Pape, F. Pauss, T. Punz, A. Rizzi, F.J. Ronga, M. Rossini, L. Sala, A.K. Sanchez, M.-C. Sawley, B. Stieger, L. Tauscher[†], A. Thea, K. Theofilatos, D. Treille, C. Urscheler, R. Wallny, M. Weber, L. Wehrli, J. Weng

Universität Zürich, Zurich, Switzerland
E. Aguilo, C. Amsler, V. Chiochia, S. De Visscher, C. Favaro, M. Ivova Rikova, B. Millan Mejias, P. Otiougova, C. Regenfus, P. Robmann, A. Schmidt, H. Snoek

National Central University, Chung-Li, Taiwan

Y.H. Chang, K.H. Chen, S. Dutta, C.M. Kuo, S.W. Li, W. Lin, Z.K. Liu, Y.J. Lu, D. Mekterovic, R. Volpe, J.H. Wu, S.S. Yu

National Taiwan University (NTU), Taipei, Taiwan
P. Bartalini, P. Chang, Y.H. Chang, Y.W. Chang, Y. Chao, K.F. Chen, W.-S. Hou, Y. Hsiung, K.Y. Kao, Y.J. Lei, R.-S. Lu, J.G. Shiu, Y.M. Tzeng, M. Wang

Cukurova University, Adana, Turkey
A. Adiguzel, M.N. Bakirci[34], S. Cerci[35], C. Dozen, I. Dumanoglu, E. Eskut, S. Girgis, G. Gokbulut, I. Hos, E.E. Kangal, A. Kayis Topaksu, G. Onengut, K. Ozdemir, S. Ozturk, A. Polatoz, K. Sogut[36], D. Sunar Cerci[35], B. Tali[35], H. Topakli[34], D. Uzun, L.N. Vergili, M. Vergili, S. Yilmaz

Middle East Technical University, Physics Department, Ankara, Turkey
I.V. Akin, T. Aliev, S. Bilmis, M. Deniz, H. Gamsizkan, A.M. Guler, K. Ocalan, A. Ozpineci, M. Serin, R. Sever, U.E. Surat, E. Yildirim, M. Zeyrek

Bogazici University, Istanbul, Turkey
M. Deliomeroglu, D. Demir[37], E. Gülmez, B. Isildak, M. Kaya[38], O. Kaya[38], S. Ozkorucuklu[39], N. Sonmez[40]

National Scientific Center, Kharkov Institute of Physics and Technology, Kharkov, Ukraine
L. Levchuk

University of Bristol, Bristol, United Kingdom
F. Bostock, J.J. Brooke, T.L. Cheng, E. Clement, D. Cussans, R. Frazier, J. Goldstein, M. Grimes, M. Hansen, D. Hartley, G.P. Heath, H.F. Heath, L. Kreczko, S. Metson, D.M. Newbold[41], K. Nirunpong, A. Poll, S. Senkin, V.J. Smith, S. Ward

Rutherford Appleton Laboratory, Didcot, United Kingdom
L. Basso[42], K.W. Bell, A. Belyaev[42], C. Brew, R.M. Brown, B. Camanzi, D.J.A. Cockerill, J.A. Coughlan, K. Harder, S. Harper, J. Jackson, B.W. Kennedy, E. Olaiya, D. Petyt, B.C. Radburn-Smith, C.H. Shepherd-Themistocleous, I.R. Tomalin, W.J. Womersley, S.D. Worm

Imperial College, London, United Kingdom
R. Bainbridge, G. Ball, J. Ballin, R. Beuselinck, O. Buchmuller, D. Colling, N. Cripps, M. Cutajar, G. Davies, M. Della Negra, W. Ferguson, J. Fulcher, D. Futyan, A. Gilbert, A. Guneratne Bryer, G. Hall, Z. Hatherell, J. Hays, G. Iles, M. Jarvis, G. Karapostoli, L. Lyons, B.C. MacEvoy, A.-M. Magnan, J. Marrouche, B. Mathias, R. Nandi, J. Nash, A. Nikitenko[31], A. Papageorgiou, M. Pesaresi, K. Petridis, M. Pioppi[43], D.M. Raymond, S. Rogerson, N. Rompotis, A. Rose, M.J. Ryan, C. Seez, P. Sharp, A. Sparrow, A. Tapper, S. Tourneur, M. Vazquez Acosta, T. Virdee, S. Wakefield, N. Wardle, D. Wardrope, T. Whyntie

Brunel University, Uxbridge, United Kingdom
M. Barrett, M. Chadwick, J.E. Cole, P.R. Hobson, A. Khan, P. Kyberd, D. Leslie, W. Martin, I.D. Reid, L. Teodorescu

Baylor University, Waco, USA
K. Hatakeyama, H. Liu

Boston University, Boston, USA
T. Bose, E. Carrera Jarrin, C. Fantasia, A. Heister, J. St. John, P. Lawson, D. Lazic, J. Rohlf, D. Sperka, L. Sulak

Brown University, Providence, USA
A. Avetisyan, S. Bhattacharya, J.P. Chou, D. Cutts, A. Ferapontov, U. Heintz, S. Jabeen, G. Kukartsev, G. Landsberg, M. Luk, M. Narain, D. Nguyen, M. Segala, T. Sinthuprasith, T. Speer, K.V. Tsang

University of California, Davis, Davis, USA
R. Breedon, M. Calderon De La Barca Sanchez, S. Chauhan, M. Chertok, J. Conway, P.T. Cox, J. Dolen, R. Erbacher, E. Friis, W. Ko, A. Kopecky, R. Lander, H. Liu, S. Maruyama, T. Miceli, M. Nikolic, D. Pellett, J. Robles, S. Salur, T. Schwarz, M. Searle, J. Smith, M. Squires, M. Tripathi, R. Vasquez Sierra, C. Veelken

University of California, Los Angeles, Los Angeles, USA
V. Andreev, K. Arisaka, D. Cline, R. Cousins, A. Deisher, J. Duris, S. Erhan, C. Farrell, J. Hauser, M. Ignatenko, C. Jarvis, C. Plager, G. Rakness, P. Schlein[†], J. Tucker, V. Valuev

University of California, Riverside, Riverside, USA
J. Babb, A. Chandra, R. Clare, J. Ellison, J.W. Gary, F. Giordano, G. Hanson, G.Y. Jeng, S.C. Kao, F. Liu, H. Liu, O.R. Long, A. Luthra, H. Nguyen, B.C. Shen[†], R. Stringer, J. Sturdy, S. Sumowidagdo, R. Wilken, S. Wimpenny

University of California, San Diego, La Jolla, USA
W. Andrews, J.G. Branson, G.B. Cerati, D. Evans, F. Golf, A. Holzner, R. Kelley, M. Lebourgeois, J. Letts, B. Mangano, S. Padhi, C. Palmer, G. Petrucciani, H. Pi, M. Pieri, R. Ranieri, M. Sani, V. Sharma, S. Simon, E. Sudano, Y. Tu, A. Vartak, S. Wasserbaech[44], F. Würthwein, A. Yagil, J. Yoo

University of California, Santa Barbara, Santa Barbara, USA
D. Barge, R. Bellan, C. Campagnari, M. D'Alfonso, T. Danielson, K. Flowers, P. Geffert, J. Incandela, C. Justus, P. Kalavase, S.A. Koay, D. Kovalskyi, V. Krutelyov, S. Lowette, N. Mccoll, V. Pavlunin, F. Rebassoo, J. Ribnik, J. Richman, R. Rossin, D. Stuart, W. To, J.R. Vlimant

California Institute of Technology, Pasadena, USA
A. Apresyan, A. Bornheim, J. Bunn, Y. Chen, M. Gataullin, Y. Ma, A. Mott, H.B. Newman, C. Rogan, K. Shin, V. Timciuc, P. Traczyk, J. Veverka, R. Wilkinson, Y. Yang, R.Y. Zhu

Carnegie Mellon University, Pittsburgh, USA
B. Akgun, R. Carroll, T. Ferguson, Y. Iiyama, D.W. Jang, S.Y. Jun, Y.F. Liu, M. Paulini, J. Russ, H. Vogel, I. Vorobiev

University of Colorado at Boulder, Boulder, USA
J.P. Cumalat, M.E. Dinardo, B.R. Drell, C.J. Edelmaier, W.T. Ford, A. Gaz, B. Heyburn, E. Luiggi Lopez, U. Nauenberg, J.G. Smith, K. Stenson, K.A. Ulmer, S.R. Wagner, S.L. Zang

Cornell University, Ithaca, USA
L. Agostino, J. Alexander, D. Cassel, A. Chatterjee, S. Das, N. Eggert, L.K. Gibbons, B. Heltsley, W. Hopkins, A. Khukhunaishvili, B. Kreis, G. Nicolas Kaufman, J.R. Patterson, D. Puigh, A. Ryd, E. Salvati, X. Shi, W. Sun, W.D. Teo, J. Thom, J. Thompson, J. Vaughan, Y. Weng, L. Winstrom, P. Wittich

Fairfield University, Fairfield, USA
A. Biselli, G. Cirino, D. Winn

Fermi National Accelerator Laboratory, Batavia, USA
S. Abdullin, M. Albrow, J. Anderson, G. Apollinari, M. Atac, J.A. Bakken, S. Banerjee, L.A.T. Bauerdick, A. Beretvas, J. Berryhill, P.C. Bhat, I. Bloch, F. Borcherding, K. Burkett,

J.N. Butler, V. Chetluru, H.W.K. Cheung, F. Chlebana, S. Cihangir, W. Cooper, D.P. Eartly, V.D. Elvira, S. Esen, I. Fisk, J. Freeman, Y. Gao, E. Gottschalk, D. Green, K. Gunthoti, O. Gutsche, J. Hanlon, R.M. Harris, J. Hirschauer, B. Hooberman, H. Jensen, M. Johnson, U. Joshi, R. Khatiwada, B. Klima, K. Kousouris, S. Kunori, S. Kwan, C. Leonidopoulos, P. Limon, D. Lincoln, R. Lipton, J. Lykken, K. Maeshima, J.M. Marraffino, D. Mason, P. McBride, T. Miao, K. Mishra, S. Mrenna, Y. Musienko[45], C. Newman-Holmes, V. O'Dell, R. Pordes, O. Prokofyev, N. Saoulidou, E. Sexton-Kennedy, S. Sharma, W.J. Spalding, L. Spiegel, P. Tan, L. Taylor, S. Tkaczyk, L. Uplegger, E.W. Vaandering, R. Vidal, J. Whitmore, W. Wu, F. Yang, F. Yumiceva, J.C. Yun

University of Florida, Gainesville, USA
D. Acosta, P. Avery, D. Bourilkov, M. Chen, M. De Gruttola, G.P. Di Giovanni, D. Dobur, A. Drozdetskiy, R.D. Field, M. Fisher, Y. Fu, I.K. Furic, J. Gartner, B. Kim, J. Konigsberg, A. Korytov, A. Kropivnitskaya, T. Kypreos, K. Matchev, G. Mitselmakher, L. Muniz, C. Prescott, R. Remington, M. Schmitt, B. Scurlock, P. Sellers, N. Skhirtladze, M. Snowball, D. Wang, J. Yelton, M. Zakaria

Florida International University, Miami, USA
C. Ceron, V. Gaultney, L. Kramer, L.M. Lebolo, S. Linn, P. Markowitz, G. Martinez, D. Mesa, J.L. Rodriguez

Florida State University, Tallahassee, USA
T. Adams, A. Askew, J. Bochenek, J. Chen, B. Diamond, S.V. Gleyzer, J. Haas, S. Hagopian, V. Hagopian, M. Jenkins, K.F. Johnson, H. Prosper, L. Quertenmont, S. Sekmen, V. Veeraraghavan

Florida Institute of Technology, Melbourne, USA
M.M. Baarmand, B. Dorney, S. Guragain, M. Hohlmann, H. Kalakhety, R. Ralich, I. Vodopiyanov

University of Illinois at Chicago (UIC), Chicago, USA
M.R. Adams, I.M. Anghel, L. Apanasevich, Y. Bai, V.E. Bazterra, R.R. Betts, J. Callner, R. Cavanaugh, C. Dragoiu, L. Gauthier, C.E. Gerber, S. Hamdan, D.J. Hofman, S. Khalatyan, G.J. Kunde[46], F. Lacroix, M. Malek, C. O'Brien, C. Silvestre, A. Smoron, D. Strom, N. Varelas

The University of Iowa, Iowa City, USA
U. Akgun, E.A. Albayrak, B. Bilki, W. Clarida, F. Duru, C.K. Lae, E. McCliment, J.-P. Merlo, H. Mermerkaya[47], A. Mestvirishvili, A. Moeller, J. Nachtman, C.R. Newsom, E. Norbeck, J. Olson, Y. Onel, F. Ozok, S. Sen, J. Wetzel, T. Yetkin, K. Yi

Johns Hopkins University, Baltimore, USA
B.A. Barnett, B. Blumenfeld, A. Bonato, C. Eskew, D. Fehling, G. Giurgiu, A.V. Gritsan, Z.J. Guo, G. Hu, P. Maksimovic, S. Rappoccio, M. Swartz, N.V. Tran, A. Whitbeck

The University of Kansas, Lawrence, USA
P. Baringer, A. Bean, G. Benelli, O. Grachov, R.P. Kenny Iii, M. Murray, D. Noonan, S. Sanders, J.S. Wood, V. Zhukova

Kansas State University, Manhattan, USA
A.F. Barfuss, T. Bolton, I. Chakaberia, A. Ivanov, S. Khalil, M. Makouski, Y. Maravin, S. Shrestha, I. Svintradze, Z. Wan

Lawrence Livermore National Laboratory, Livermore, USA
J. Gronberg, D. Lange, D. Wright

University of Maryland, College Park, USA
A. Baden, M. Boutemeur, S.C. Eno, D. Ferencek, J.A. Gomez, N.J. Hadley, R.G. Kellogg, M. Kirn, Y. Lu, A.C. Mignerey, K. Rossato, P. Rumerio, F. Santanastasio, A. Skuja, J. Temple, M.B. Tonjes, S.C. Tonwar, E. Twedt

Massachusetts Institute of Technology, Cambridge, USA
B. Alver, G. Bauer, J. Bendavid, W. Busza, E. Butz, I.A. Cali, M. Chan, V. Dutta, P. Everaerts, G. Gomez Ceballos, M. Goncharov, K.A. Hahn, P. Harris, Y. Kim, M. Klute, Y.-J. Lee, W. Li, C. Loizides, P.D. Luckey, T. Ma, S. Nahn, C. Paus, D. Ralph, C. Roland, G. Roland, M. Rudolph, G.S.F. Stephans, F. Stöckli, K. Sumorok, K. Sung, E.A. Wenger, R. Wolf, S. Xie, M. Yang, Y. Yilmaz, A.S. Yoon, M. Zanetti

University of Minnesota, Minneapolis, USA
S.I. Cooper, P. Cushman, B. Dahmes, A. De Benedetti, P.R. Dudero, G. Franzoni, J. Haupt, K. Klapoetke, Y. Kubota, J. Mans, V. Rekovic, R. Rusack, M. Sasseville, A. Singovsky

University of Mississippi, University, USA
L.M. Cremaldi, R. Godang, R. Kroeger, L. Perera, R. Rahmat, D.A. Sanders, D. Summers

University of Nebraska-Lincoln, Lincoln, USA
K. Bloom, S. Bose, J. Butt, D.R. Claes, A. Dominguez, M. Eads, J. Keller, T. Kelly, I. Kravchenko, J. Lazo-Flores, H. Malbouisson, S. Malik, G.R. Snow

State University of New York at Buffalo, Buffalo, USA
U. Baur, A. Godshalk, I. Iashvili, S. Jain, A. Kharchilava, A. Kumar, S.P. Shipkowski, K. Smith

Northeastern University, Boston, USA
G. Alverson, E. Barberis, D. Baumgartel, O. Boeriu, M. Chasco, S. Reucroft, J. Swain, D. Trocino, D. Wood, J. Zhang

Northwestern University, Evanston, USA
A. Anastassov, A. Kubik, N. Odell, R.A. Ofierzynski, B. Pollack, A. Pozdnyakov, M. Schmitt, S. Stoynev, M. Velasco, S. Won

University of Notre Dame, Notre Dame, USA
L. Antonelli, D. Berry, M. Hildreth, C. Jessop, D.J. Karmgard, J. Kolb, T. Kolberg, K. Lannon, W. Luo, S. Lynch, N. Marinelli, D.M. Morse, T. Pearson, R. Ruchti, J. Slaunwhite, N. Valls, M. Wayne, J. Ziegler

The Ohio State University, Columbus, USA
B. Bylsma, L.S. Durkin, J. Gu, C. Hill, P. Killewald, K. Kotov, T.Y. Ling, M. Rodenburg, G. Williams

Princeton University, Princeton, USA
N. Adam, E. Berry, P. Elmer, D. Gerbaudo, V. Halyo, P. Hebda, A. Hunt, J. Jones, E. Laird, D. Lopes Pegna, D. Marlow, T. Medvedeva, M. Mooney, J. Olsen, P. Piroué, X. Quan, H. Saka, D. Stickland, C. Tully, J.S. Werner, A. Zuranski

University of Puerto Rico, Mayaguez, USA
J.G. Acosta, X.T. Huang, A. Lopez, H. Mendez, S. Oliveros, J.E. Ramirez Vargas, A. Zatserklyaniy

Purdue University, West Lafayette, USA
E. Alagoz, V.E. Barnes, G. Bolla, L. Borrello, D. Bortoletto, A. Everett, A.F. Garfinkel, L. Gutay, Z. Hu, M. Jones, O. Koybasi, M. Kress, A.T. Laasanen, N. Leonardo, C. Liu, V. Maroussov,

P. Merkel, D.H. Miller, N. Neumeister, I. Shipsey, D. Silvers, A. Svyatkovskiy, H.D. Yoo, J. Zablocki, Y. Zheng

Purdue University Calumet, Hammond, USA
P. Jindal, N. Parashar

Rice University, Houston, USA
C. Boulahouache, V. Cuplov, K.M. Ecklund, F.J.M. Geurts, B.P. Padley, R. Redjimi, J. Roberts, J. Zabel

University of Rochester, Rochester, USA
B. Betchart, A. Bodek, Y.S. Chung, R. Covarelli, P. de Barbaro, R. Demina, Y. Eshaq, H. Flacher, A. Garcia-Bellido, P. Goldenzweig, Y. Gotra, J. Han, A. Harel, D.C. Miner, D. Orbaker, G. Petrillo, D. Vishnevskiy, M. Zielinski

The Rockefeller University, New York, USA
A. Bhatti, R. Ciesielski, L. Demortier, K. Goulianos, G. Lungu, S. Malik, C. Mesropian, M. Yan

Rutgers, the State University of New Jersey, Piscataway, USA
O. Atramentov, A. Barker, D. Duggan, Y. Gershtein, R. Gray, E. Halkiadakis, D. Hidas, D. Hits, A. Lath, S. Panwalkar, R. Patel, A. Richards, K. Rose, S. Schnetzer, S. Somalwar, R. Stone, S. Thomas

University of Tennessee, Knoxville, USA
G. Cerizza, M. Hollingsworth, S. Spanier, Z.C. Yang, A. York

Texas A&M University, College Station, USA
R. Eusebi, J. Gilmore, A. Gurrola, T. Kamon, V. Khotilovich, R. Montalvo, I. Osipenkov, Y. Pakhotin, J. Pivarski, A. Safonov, S. Sengupta, A. Tatarinov, D. Toback, M. Weinberger

Texas Tech University, Lubbock, USA
N. Akchurin, C. Bardak, J. Damgov, C. Jeong, K. Kovitanggoon, S.W. Lee, P. Mane, Y. Roh, A. Sill, I. Volobouev, R. Wigmans, E. Yazgan

Vanderbilt University, Nashville, USA
E. Appelt, E. Brownson, D. Engh, C. Florez, W. Gabella, M. Issah, W. Johns, P. Kurt, C. Maguire, A. Melo, P. Sheldon, B. Snook, S. Tuo, J. Velkovska

University of Virginia, Charlottesville, USA
M.W. Arenton, M. Balazs, S. Boutle, B. Cox, B. Francis, R. Hirosky, A. Ledovskoy, C. Lin, C. Neu, R. Yohay

Wayne State University, Detroit, USA
S. Gollapinni, R. Harr, P.E. Karchin, P. Lamichhane, M. Mattson, C. Milstène, A. Sakharov

University of Wisconsin, Madison, USA
M. Anderson, M. Bachtis, J.N. Bellinger, D. Carlsmith, S. Dasu, J. Efron, K. Flood, L. Gray, K.S. Grogg, M. Grothe, R. Hall-Wilton, M. Herndon, P. Klabbers, J. Klukas, A. Lanaro, C. Lazaridis, J. Leonard, R. Loveless, A. Mohapatra, F. Palmonari, D. Reeder, I. Ross, A. Savin, W.H. Smith, J. Swanson, M. Weinberg

†: Deceased
1: Also at CERN, European Organization for Nuclear Research, Geneva, Switzerland
2: Also at Universidade Federal do ABC, Santo Andre, Brazil
3: Also at Laboratoire Leprince-Ringuet, Ecole Polytechnique, IN2P3-CNRS, Palaiseau, France
4: Also at British University, Cairo, Egypt

5: Also at Fayoum University, El-Fayoum, Egypt
6: Also at Ain Shams University, Cairo, Egypt
7: Also at Soltan Institute for Nuclear Studies, Warsaw, Poland
8: Also at Massachusetts Institute of Technology, Cambridge, USA
9: Also at Université de Haute-Alsace, Mulhouse, France
10: Also at Brandenburg University of Technology, Cottbus, Germany
11: Also at Moscow State University, Moscow, Russia
12: Also at Institute of Nuclear Research ATOMKI, Debrecen, Hungary
13: Also at Eötvös Loránd University, Budapest, Hungary
14: Also at Tata Institute of Fundamental Research - HECR, Mumbai, India
15: Also at University of Visva-Bharati, Santiniketan, India
16: Also at Sharif University of Technology, Tehran, Iran
17: Also at Shiraz University, Shiraz, Iran
18: Also at Isfahan University of Technology, Isfahan, Iran
19: Also at Facoltà Ingegneria Università di Roma "La Sapienza", Roma, Italy
20: Also at Università della Basilicata, Potenza, Italy
21: Also at Laboratori Nazionali di Legnaro dell' INFN, Legnaro, Italy
22: Also at Università degli studi di Siena, Siena, Italy
23: Also at California Institute of Technology, Pasadena, USA
24: Also at Faculty of Physics of University of Belgrade, Belgrade, Serbia
25: Also at University of California, Los Angeles, Los Angeles, USA
26: Also at University of Florida, Gainesville, USA
27: Also at Université de Genève, Geneva, Switzerland
28: Also at Scuola Normale e Sezione dell' INFN, Pisa, Italy
29: Also at University of Athens, Athens, Greece
30: Also at The University of Kansas, Lawrence, USA
31: Also at Institute for Theoretical and Experimental Physics, Moscow, Russia
32: Also at Paul Scherrer Institut, Villigen, Switzerland
33: Also at University of Belgrade, Faculty of Physics and Vinca Institute of Nuclear Sciences, Belgrade, Serbia
34: Also at Gaziosmanpasa University, Tokat, Turkey
35: Also at Adiyaman University, Adiyaman, Turkey
36: Also at Mersin University, Mersin, Turkey
37: Also at Izmir Institute of Technology, Izmir, Turkey
38: Also at Kafkas University, Kars, Turkey
39: Also at Suleyman Demirel University, Isparta, Turkey
40: Also at Ege University, Izmir, Turkey
41: Also at Rutherford Appleton Laboratory, Didcot, United Kingdom
42: Also at School of Physics and Astronomy, University of Southampton, Southampton, United Kingdom
43: Also at INFN Sezione di Perugia; Università di Perugia, Perugia, Italy
44: Also at Utah Valley University, Orem, USA
45: Also at Institute for Nuclear Research, Moscow, Russia
46: Also at Los Alamos National Laboratory, Los Alamos, USA
47: Also at Erzincan University, Erzincan, Turkey